Synthesis and applications of carbon nanomaterials for energy generation and storage

Marco Notarianni[1,2], Jinzhang Liu[3], Kristy Vernon[1], Nunzio Motta[1]

[1]*Institute of Future Environments and School of Chemistry, Physics, and Mechanical Engineering, Queensland University of Technology, Brisbane QLD 4001, Australia*

[2]*Plasma-Therm LLC, 10050 16th St North, St. Petersburg, FL 33716 USA*

[3]*School of Materials Science and Engineering, Beihang University, Beijing, 100191, China*

Abstract

The world is facing an energy crisis due to exponential population growth and limited availability of fossil fuels. Carbon, one of the most abundant materials found on earth, and its allotrope forms such as fullerenes, carbon nanotubes and graphene have been proposed over the last 20 years for energy generation and storage because of their extraordinary properties and ease to produce. Different approaches to synthesise and incorporate carbon nanomaterials in organic photovoltaics and supercapacitors have been reviewed and discussed in this work, highlighting their benefits compared to other materials commonly used in these devices. The use of carbon nanotubes, fullerenes and graphene in organic photovoltaics and supercapacitors is described in detail, explaining how their remarkable properties can enhance the efficiency of solar cells and the energy storage in supercapacitors. .

Both fullerene, carbon nanotubes and graphene have been included in solar cells, obtaining interesting results, although a number of problems are still to be overcome in order to achieve high efficiency and stability. However, the flexibility and the low cost of these materials provide the opportunity for many applications like wearable and disposable electronics or mobile charging.

The application of carbon nanotubes and graphene to supercapacitors is also discussed and reviewed in this work, including graphene synthetized by electrochemical method used as electrode in flexible solid-state supercapacitors. Carbon nanotubes in combination with graphene can create a more porous film with extraordinary capacitive performance, paving the way to many practical applications from mobile phones to electric cars.

In conclusion we show that carbon nanomaterials, developed by inexpensive synthesis and process methods such as printing and roll-to-roll techniques, are ideal for the development of flexible devices for energy generation and storage, the key to the portable electronic of the future.

Keywords

Energy; Carbon; Nanomaterials; Fullerenes; Carbon nanotubes; Graphene; Plasmonic structures; Gold nanoparticles; Organic solar cells; Supercapacitors; Current collector; Thin films.

Contents

1 The energy future: challenges and opportunities

The demand for energy in the 21st century is increasing due to the increase in the world's population and technological advances [1]. The worldwide population is using today about 17 TW (17 trillions of watt) of power with around 4 TW being consumed in the US alone[2] . Energy experts are predicting that we will need an additional 30 TW by 2050 due to the global population growth and economic development worldwide [3].

Solving this energy demand using more efficient or clean alternative energy sources is not just going to save the planet from harmful effects caused by the pollution but could reduce disparity and create a more peaceful world [4]. Energy is just one of the many problems that the world is facing but it is probably the most important to be addressed with urgency in order to also solve other off-shoot problems. Richard E. Smalley, Nobel Laureate in Chemistry in 1996 for the discovery of the fullerene, presented in one of his last talks a list named: "Top Ten Problems of Humanity for the Next 50 Years" [5]. The list in order of priority is:

1. Energy
2. Water
3. Food
4. Environment
5. Poverty
6. Terrorism and war
7. Disease
8. Education
9. Democracy
10. Population

The energy problem is on the top of the list because, according to Smalley, it directly influences the other problems and thus should be prioritized accordingly by governments worldwide. The first immediate solution to this problem would be to work on energy efficiency programs because it has been demonstrated that developed countries could already save 25% of energy [6].

The majority, about 87% of energy produced in 2013, was composed of fossil fuels such as oil, gas and coal which represented the best choice of energy production at competitive costs in the 20th and 21st century (Figure 1) [7]. Unfortunately, It has been

proven that fossil fuels have catastrophic consequences for human health [8] and global warming [9] and their reserves are progressively decreasing [10].

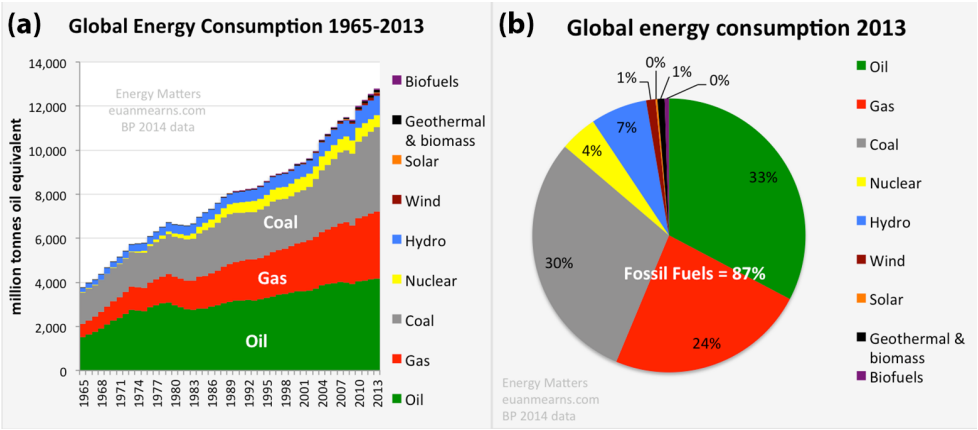

Figure 1: (a) Global energy consumption growth from 1965 to 2013. (b) The share of different energy sources for the global energy consumption in 2013 (from [7]).

Despite the fact that our technological advances are able to reduce the amount of kilograms of carbon emitted to the atmosphere as CO_2 per year per watt of power (Figure 2 (a)), CO_2 emissions will continue to increase due to the increase in energy consumption worldwide (Figure 2 (b)) [11]. For example, to stabilize the concentration of CO_2 at 350 ppm (purple line in Figure 2 (b)), ideally, we will need to reduce the carbon emissions worldwide to zero by 2050 [12].

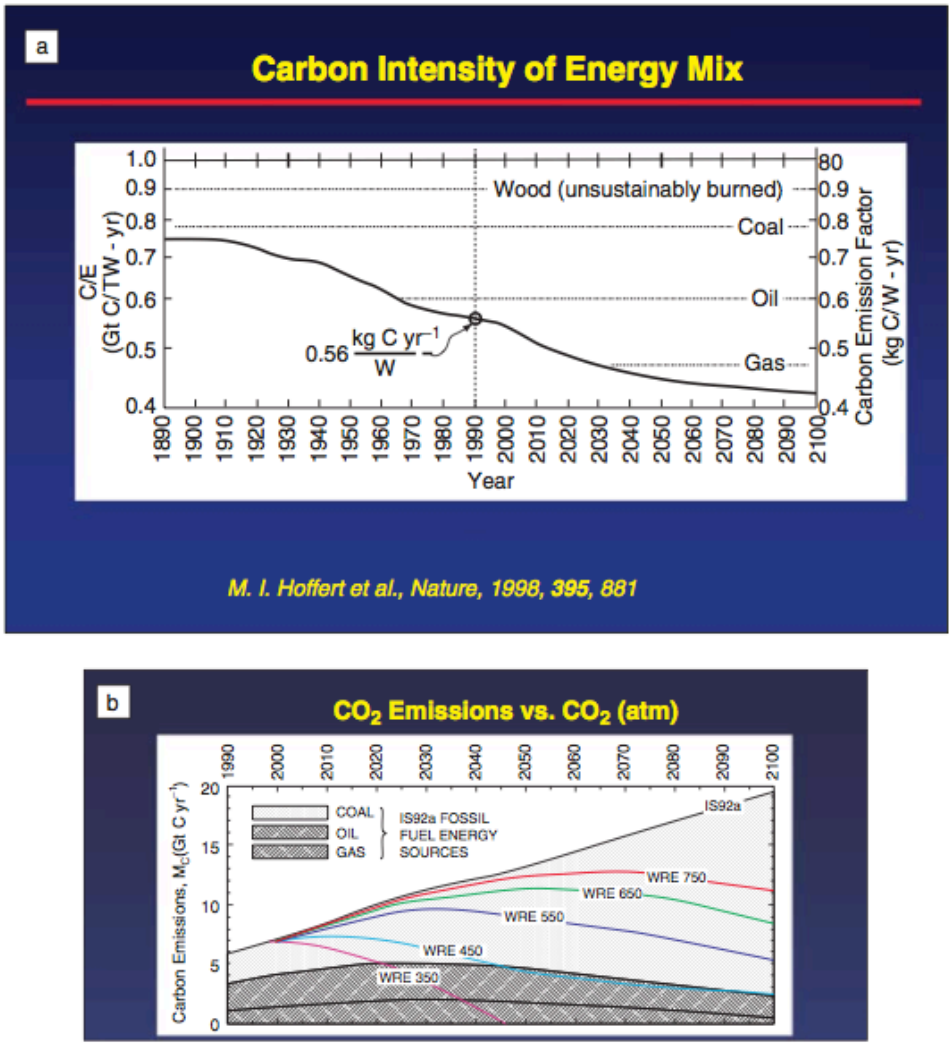

Figure 2: (a) Carbon intensity of the energy mix from 1890 through 2100 (projected), i.e., kilograms of carbon emitted to the atmosphere as CO_2 per year per watt of power produced from combined sources of fuel. The average in 1990 is shown as an open circle on the carbon intensity curve. (b) CO_2 emissions versus CO_2 in the atmosphere, projected through 2100 (from [12]).

It has been estimated that in order to generate about 1/3 of the prospective energy needed by 2050, we should build around 10,000 nuclear plants over the next 36 years [12]! Apart from the costs of building all of these nuclear plants, nuclear energy has risks and hazards associated with it. Nuclear plants are in fact very expensive to build, maintain and protect from terroristic attacks. Not to mention, the disposal of nuclear waste which has still not been resolved leaving problems for future generations to deal with [13].

Renewable energies represent the easiest way to produce clean and safe energy but they represented only 10% of the resources used in 2013 (Figure 1). Unfortunately, the cost of producing energy from renewable sources is still high. But prices are decreasing, allowing these technologies to be considered in the near future when the prices of fossil fuels will increase due to their shortage. Among all of the renewable energy resources available, including hydroelectricity, geothermal energy, wind energy, biomass and others, solar energy probably represents the best renewable resource. In fact, the biggest nuclear reactor that we can even imagine is the sun which has given energy to the earth for over 4 billion years and provides more energy in one hour than all of the energy consumed on our planet in an entire year. We receive on Earth about 170,000 TW of electromagnetic radiation. Therefore, covering 0.16% of the land on earth with 10% efficient solar conversion systems would provide over 20 TW of power [3]. However, apart from the costs of this technology at the moment ($0.20-0.50 kW/hr), building solar farms in remote areas is not without its own problems. In fact, the advantage of the oil in the last century and still today is the possibility to transport this form of energy across oceans without the need to build expensive infrastructures. For example, the price per gallon of gas includes less than 10% of the transportation cost to the gas station [12]. On the other hand, the cost of building solar farms is very high considering the realization of infrastructures to transport the electricity from remote desert areas to the urban centres in addition to the 25% of energy that is lost in the transportation [3]. Receiving incentives from the government to install photovoltaic systems on private property could be a viable solution to benefit immediately from the energy produced without the construction of any infrastructure and without any transportation losses. However, this could definitively create a sort of energy independence that not favored by major energy corporations. The energy business is the biggest one in the world considering companies like Exxon Mobil, which was listed second in the US in 2014 publicly traded companies having the greatest market capitalization and Saudi Aramco (an oil state owned company) that was estimated from $781 billion to $7 trillion [14].

The other major problems of solar energy are that it is diffuse (170 W/m^2) and intermittent. This is why concentration and storage become two critical issues to solve in order to make this energy source cost competitive with fossil fuels. The challenge over the next few years will not just be to produce electricity in a safe and clean way but also to store the energy produced with technologies more efficient and more environmentally

friendly than chemical batteries [13]. Creating small-scale energy storage technologies with a combination of smart grid technologies could help to provide energy to each single house when immediately needed and with a high efficiency.

Nanotechnology could help to solve solar energy's obstacles and meet the energy expectations without compromising the environment and the population's health by creating new devices that are able to generate, store and transport electricity in a clean more efficient way and with smaller space requirements. Specifically, the use of nanostructured allotrope forms of carbon and derivatives such as fullerenes, carbon nanotubes (CNTs) and graphene have been widely investigated over the past 10 years for energy generation and storage. In particular, the possibility to include these nanostructured materials using lightweight flexible substrates, printable inks, low temperature and ambient pressure fabrication tools allows for dramatic reductions in the production costs [15].

Organic solar cell devices and electrochemical capacitors, also called supercapacitors, based on carbon nanostructures allow in the near future the fabrication of devices that could be more efficient and cheaper to produce than conventional silicon solar cells and chemical batteries [16-17]. The potential to produce these devices "in house" with simple tools like printers, scissors and glue makes these technologies widely available, including in developing countries.

2 Carbon nanomaterials: properties and Synthesis

Carbon, one of the most abundant materials found on earth, can be found in nature in its elemental form as graphite, diamond and coal. Its production is about 9 Gt/year for technological applications with a record production compared to other elements [18]. Nanostructured allotrope forms of carbon have been intensively investigated in the past two decades because of their unique hybridization properties and sensitivity to perturbation during synthesis allowing for fine manipulation of the properties of the material. In particular, carbon can be found in several different hybridization states; each one with unique properties (Figure 3). In fact, chemical, mechanical, thermal and electrical properties of the different allotrope forms are directly correlated to their structure and hybridization state opening up the possibility to use the same material for a wide range of applications [19].

Herein, the synthesis and application of fullerenes, carbon nanotubes (CNTs) and graphene will be discussed for energy generation and storage.

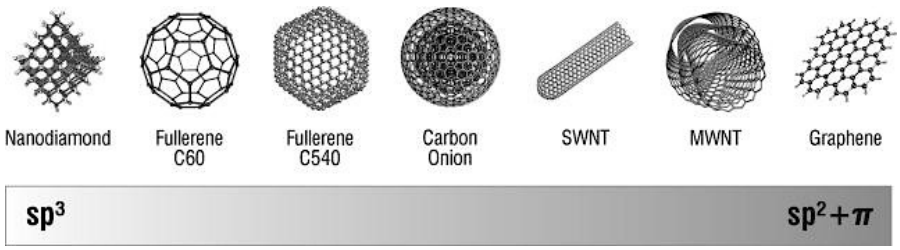

Figure 3: Hybridization states of carbon-based nanomaterials [19].

2.1 Fullerenes

Fullerenes are allotrope forms of carbon, also called buckyballs because of their spherical structure. Fullerenes were predicted and studied theoretically before their experimental discovery by Japanese [20] and Russian [21] researchers in the 1970s, but it was only in the mid -1980s that H. Kroto, R. Smalley and R. Curl were able to detect the first fullerene molecule obtained by laser vaporization of carbon from a graphite target using mass spectroscopy [22]. The name fullerene (C_{60}) was dedicated to the architect Buckminster Fuller who was famous for designing and building geodesic

domes [23]. The C_{60} is composed of hexagonal and pentagonal faces to form a spherical structure similar to a soccer ball with a diameter of ~10 Å. This icosahedral symmetry was demonstrated experimentally only in the 1990s by nuclear magnetic resonance [24]. The C_{60} was the first 0D form of allotrope carbon discovered but it is not the only one. In fact, large quantities of C_{70}, C_{76}, C_{78}, C_{84} and even large clusters, such as C_{240}, $C_{330,}$ have also been synthetized and studied [25]. In particular, the C_{70} can be seen as a C_{60} molecule with a belt of five hexagons around the equatorial plane and exhibits a more oval shape (Figure 4) [26].

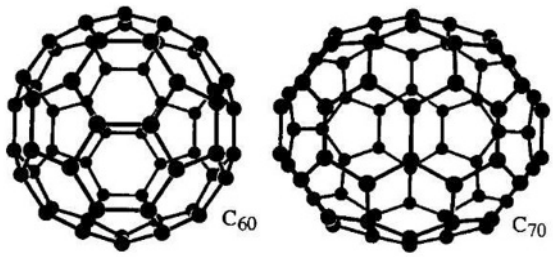

Figure 4: Structure of most significant fullerenes, the C_{60} and the C_{70}. All fullerenes exhibit hexagonal and pentagonal rings of carbon atoms (from [26]).

The main properties of C_{60} are [25]:

- Young's modulus ~ 14 GPa
- Electrical resistivity ~ 1014 Ω m
- Thermal conductivity ~ 0.4 W/mK
- Bandgap 1.7 eV

The other fullerene species show similar properties to C_{60}. Depending on the application, different fullerenes are chosen because of the slight difference in the properties.

Historically, the first technique to synthesize fullerenes is based on using laser ablation of graphite targets in a He gas, but does not produce large quantities of the materials and so is mostly used for research studies. The common method to produce large quantities (several grams per day) of fullerenes was first developed by Kratschmer et al. [27] and consisted of an AC arc-discharge between high purity graphite rods in 100-200 Torr of helium (He) or Argon (Ar). The temperature required for fullerene

formation is about 2000 °C. At this temperature, the electrodes evaporate carbon forming soot that contains fullerenes which then condenses on the cool walls of a reactor made of stainless steel or Pyrex [28]. Usually, the quantity of fullerenes found in the soot is about 15% (~13% C_{60} and ~2% C_{70}). Several setups with different architectures have been proposed but the one proposed by Bezmelnitsyn et al. [29] is one of the most popular because of the large quantity of material produced. It uses 24 carbon strip auto-loaded anodes that are consumed one by one during the process while the cathode consists of a rotating carbon wheel, which passes a scraper to remove the carbon powder accumulated (Figure 5). This method leads to a fullerene production of about 100-200 g per day.

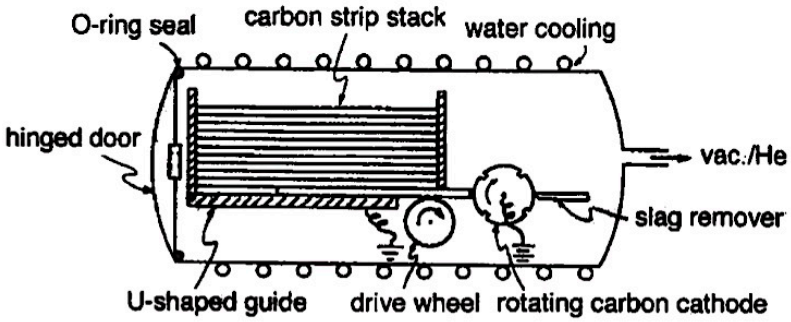

Figure 5: Schematic depiction of an auto-loading version of an arc-discharge apparatus used for fullerene production (from [29]).

Another method based on the combustion of benzene in an oxygen deficient environment has been proposed for the formation of C_{60} and C_{70} [30-31]. Benzene diluted with Ar is injected along the central axis of a combustion chamber and oxygen at 12-40 Torr being fed through a large diameter porous plate. The flame chamber is usually composed of a burner and a fuel injection system mounted in the bottom of the chamber. The chamber has viewing ports to see the process and insert the plate where the final material is deposited (Figure 6) [31].

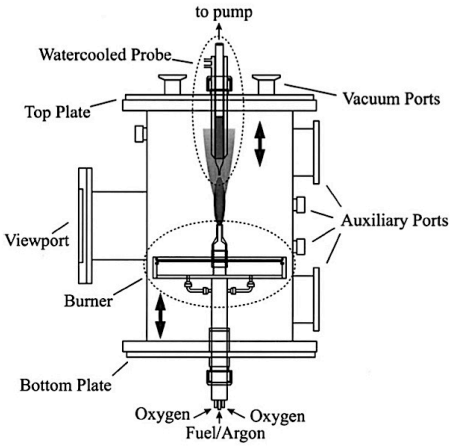

Figure 6: Diffusion flame chamber for fullerenes production [31].

Chemical methods have also been proposed to synthetize fullerenes but the yield production is so low to consider these methods only for research purposes. For example, C_{60} can be produced by the pyrolysis hydrogenation of naphthalene, corannulene or others but it requires high energies. Dehydrohalogenation of precursors can also be a valid chemical method to form C_{60} from a chloroaromatic, for example (Figure 7) [32].

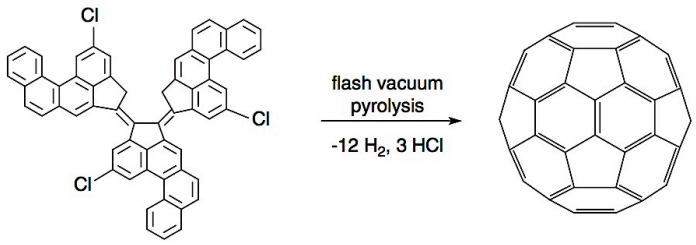

Figure 7: Formation of C_{60} through dehydrogenation/dehydrochlorination (from [32]).

Fullerenes can also be modified, by putting dopants in the cage. Fullerenes with atoms enclosed in the cage are called “endohedral fullerenes”. The endohedral fullerenes are divided in two categories: the endohedral metallofullerenes where metal atoms (typically transitional metal atoms) are inserted into the cage during the synthesis of the cage itself [33]; the endohedral non-metal doped fullerenes with noble gas such as helium, neon, argon and xenon inserted into the cage [34].

Another fullerene species is the exohedral fullerenes or fullerene derivatives, which are molecules created by bonding a fullerene with other chemical groups. A typical example of a fullerene derivative is the [6,6]-phenyl-C61-butyric acid methyl

ester ($PC_{61}BM$), which is largely used in organic solar cells. Hummelen et al. [35] were the first group to synthesize $PC_{61}BM$ by reacting diazoalcane with a C_{60} to reach the [5,6] fulleroid ester and subsequent isomerization to the [6,6]methanofullerene by refluxing it with o-dichlorobenzene solution or with trifluoroacetic acid (Figure 8) [36].

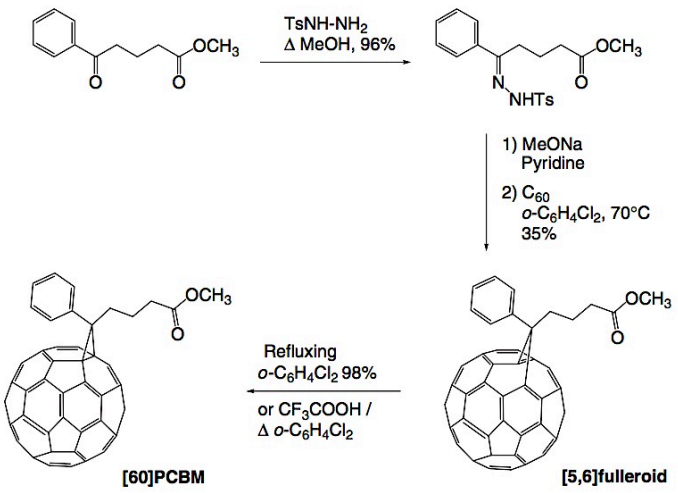

Figure 8: Synthesis of $PC_{61}BM$ by reaction between C_{60} and diazoalacane with subsequently refluxing with o-dichlorobenzene solution or with trifluoroacetic acid (from [26]).

2.2 Carbon nanotubes

Carbon nanotubes (CNTs), discovered by Ijima in 1991 [37], are another allotrope form of carbon with a cylindrical structure. The unique structures of CNTs result in many extraordinary properties. Since the discovery of CNTs, scientists have made great progress in the experimental and theoretical study of their mechanical, electrical and thermal properties. CNTs exhibit remarkable properties including:

- Tensile strength at least 37 GPa and strain to failure at least 6% [38-39]
- Young's modulus ~ 0.62 to 1.25 TPa [40]
- Electrical resistivity ~ 1 μΩ cm [41]
- Thermal conductivity ~ 3000 W/mK [42]

In addition to their extraordinary properties, the density of the CNTs is around 1.33-1.4 g/cm^3 [40], which is half of the density of aluminium (2.7 g/cm^3) making them very attractive for lightweight applications.

CNTs are categorized as single-wall carbon nanotubes (SWNTs) and multi-wall carbon nanotubes (MWNTs). SWNTs are single graphene sheets rolled up to form a tube, while the MWNTs consist of multiple rolled layers (concentric tubes) of graphene (Figure 9) [43].

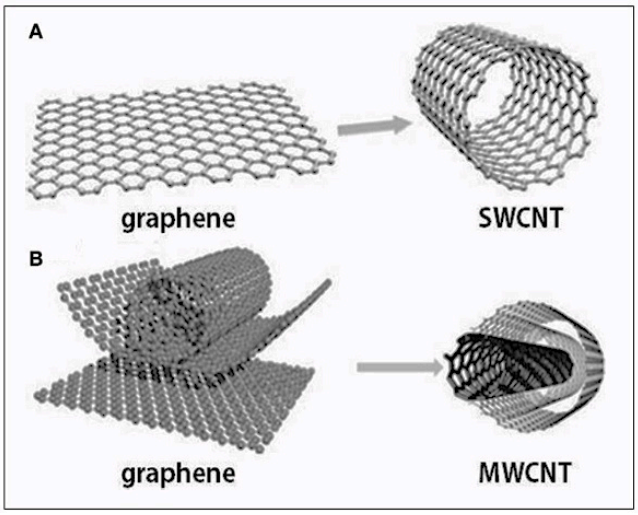

Figure 9: Graphene and carbon nanotubes as (A) single wall carbon nanotube (SWCNT) and (B) multi-wall carbon nanotube (MWCNT) structures (from [44]).

The way that the graphene is wrapped is identified by a chiral vector, whose components along the base vectors are defined by indices (n, m). If m = 0 the SWNTs are called zig-zag; if n = m, they are armchair or otherwise chiral if n ≠ m (see Figure 10) [45].

The chiral vector (C_h) identified by the index (n, m) is very important because it strongly affects the electronic properties of the SWNTs. For a given (n, m) nanotube, if n = m the nanotube is metallic; if (n-m) is a multiple of 3, the nanotube is semiconducting with a very small band gap, otherwise the nanotube is semiconducting [45]. It was also observed that the energy gap scales inversely with the tube diameter [45].

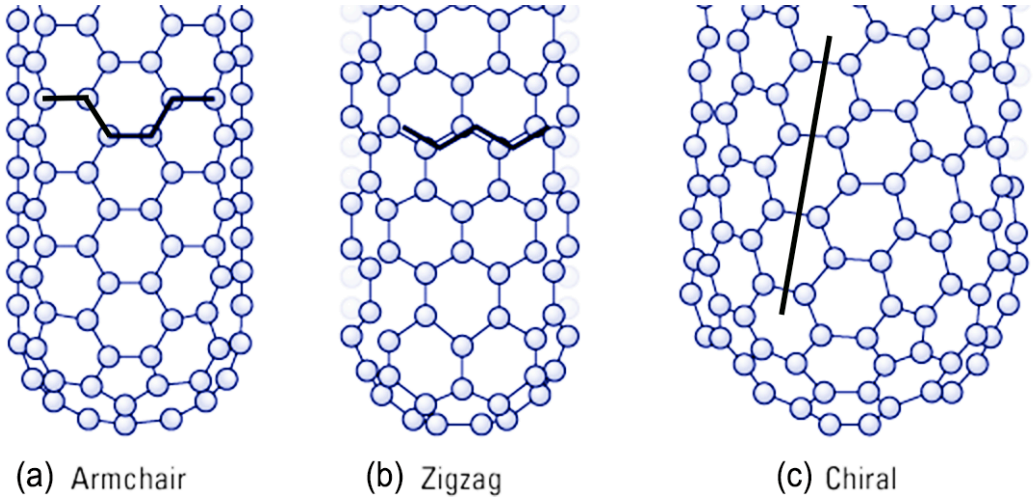

Figure 10: Schematic models for SWCNTs with the nanotube axis normal to the chiral vector, which, in turn, is along: (a) the direction $\vartheta = 30°$ in an armchair (n, n) nanotube, (b) the direction $\vartheta = 0°$ in a zig-zag (n, 0) nanotube, and (c) a general ϑ direction, in a chiral (n, m) nanotube.

An important feature of the CNTs is that they have a high aspect ratio ($A= 10^{10}$), with A=l/d, where l is the length of the CNTs that varies from 20 nm to 2 mm and d is the diameter of the tubes (typically 0.3 - 2 nm) [46].

There are three main methods to synthesize CNTs, each of which have advantages and disadvantages in terms of quality and length of the nanotubes produced [47] (Figure 11):

- Arc Discharge: higher batch yields (~ 1g/day) compared to CVD.
- Laser Vaporization: higher batch yields (~ 1-10g/day) compared to CVD.
- Chemical Vapor Deposition (CVD): high quality, most common method with low batch yields (~ 30mg/day).

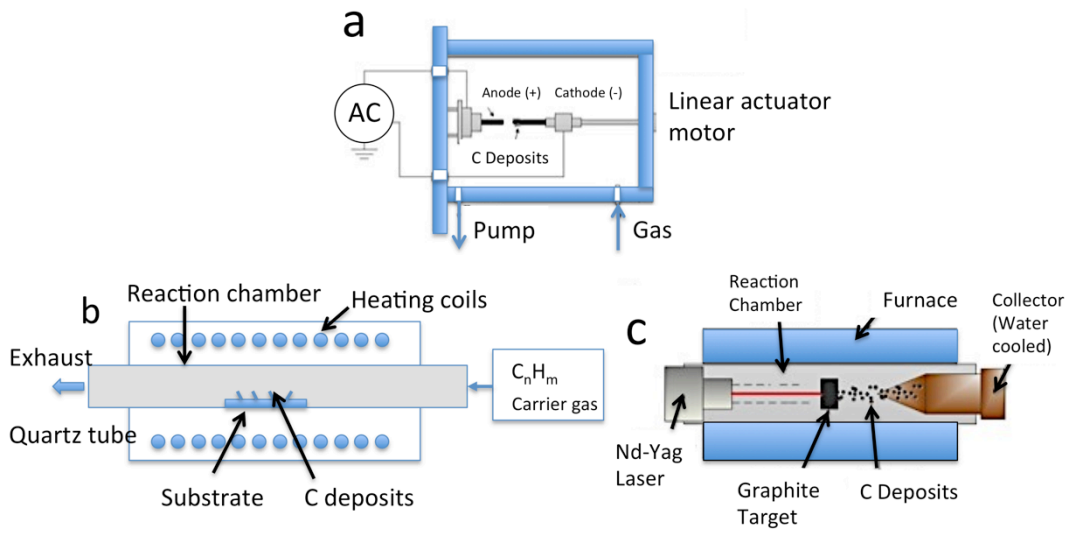

Figure 11: Schematic representation of methods used for carbon nanotube synthesis (a) Arc discharge; (b) Chemical vapor deposition; (c) Laser ablation

In the arc discharge method, the carbon is evaporated by helium plasma ignited by high currents passed through an opposing carbon anode and cathode; this method requires the use of a metal catalyst such as cobalt [48]. The nanotubes are typically bound together by strong van der Waals interactions and form tight bundles.

The second method, the laser ablation method uses continuous wave [49] or pulsed [50] lasers to ablate a carbon target containing 1 % of nickel and cobalt in a 1200 °C tube furnace. A laser beam evaporates a graphite sample containing 1% nickel and cobalt catalyst particles [51]; in the resulting vapor, the metal aggregates into carbon saturated catalyst nano-particles, which sprout the growth of CNTs [48]. These catalyst particles are necessary to produce SWNTs rather than MWNTs [52]. The relative amount of SWNTs, MWNTs, and impurities produced by these methods is dependent on the exact reactor conditions. Impurities include fullerenes, metal catalyst particles encapsulated by graphitic polyhedrons, and amorphous carbon. The majority of impurities can be removed by purification processes based on nitric acid [53]. In both, the arc discharge and laser ablation methods, bundles of MWNTs and SWNTs held together by Van der Waals forces are generated by the condensation of carbon atoms generated from the evaporation of solid carbon sources.

The third method, chemical vapor deposition (CVD), involves flowing a hydrocarbon gas over a catalyst in a tube furnace. The catalyst is typically transition metal nanoparticles on a support such as alumina. Materials grown on the catalyst are

collected after cooling the furnace to room temperature. Key process parameters are the hydrocarbon and catalyst types as well as the operating temperature [54]. Production of MWNTs typically involves ethylene or acetylene feedstock with an iron, nickel or cobalt catalyst and operating temperatures of 550-750 °C while SWNTs are produced by using methane or ethane feedstock, similar catalysts, and operating temperatures of 850-1000 °C [55]. Other CVD derivatives methods are used to produce CNTs in order to reduce temperature growth and increase the batch yields. These methods are: plasma enhanced CVD where a gas such as C_2H_2, CH_4, C_2H_4, C_2H_6, CO is supplied to the chamber and a discharge at high frequency is applied at the chamber [56]; laser-assisted thermal CVD where a continuous wave CO_2 laser with medium power,, which is perpendicularly directed on a substrate, pyrolyses sensitized mixtures of $Fe(CO)_5$ vapor and acetylene in a flow reactor [57]; HiPco (high-pressure catalytic decomposition of carbon monoxide) where carbon monoxide and catalyst particles generated from the decomposition of $Fe(CO)_5$ are flown in a high pressure reactor (up to 10 atm) at temperatures range from 800 - 1200°C [58]. With the HiPco method large yields (>10g/day) and narrow tubes can be produced [59].

2.3 Graphene

Despite their excellent electrical, mechanical and thermal properties, CNTs are not the only carbon nanomaterial that could play a major role in replacing conventional materials for energy generation and storage devices. In particular, the discovery of the electronic properties of graphene, another allotrope form of carbon, by Geim, Novoselov and co-workers [60] opened up the potential of this interesting material being employed in real world applications. In fact, graphene shows similar or even better mechanical, thermal and electronic properties than CNTs. Moreover, from an engineering point of view, the production and the usage of graphene could be easier when compared to the CNTs. Fewer manufacturing parameters, such as chirality and nature of the tubes (SWNTs vs. MWNTs), need to be considered and a larger availability of synthesis processes make it very attractive to the material science field.

Graphene represents the building block of other important allotropes because it can be stacked to form 3D - graphite, rolled to form 1D - nanotubes and wrapped to form

0D – fullerenes (Figure 12)[61] . It consists of a single atomic layer of carbon atoms bonded together in a honeycomb lattice formed by two sub-lattices, A and B, evolving from two carbon atoms. The graphene layer has a thickness of 0.34 nm and a carbon-carbon distance of 0.142 nm [62].

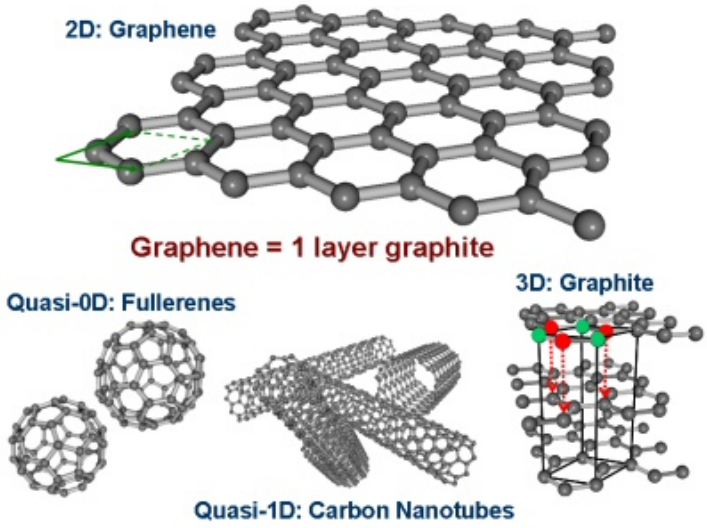

Figure 12: Honeycomb lattice of graphene. Graphene layers can be stacked into graphite or rolled up into carbon nanotubes. The formation of fullerenes requires the incorporation of five-membered rings (adapted from [61]).

The graphene characteristics measured experimentally are very close to the theoretically predicted limits: high intrinsic mobility at room temperature (250,000 $cm^2 V^{-1} s^{-1}$) [63-64], high Young's modulus (~ 1 TPa) with an intrinsic strength of 130 GPa [65-66], high thermal conductivity (over 3000 $Wm^{-1}K^{-1}$) [67] and an excellent optical transmittance (~ 97.7 %) [68]; high theoretical specific surface area (2630 $m^2 g^{-1}$) [69] non-permeability to gases [70]; capability to carry high densities of current (a million times higher than copper) [71]; anomalous Quantum Hall Effect (QHE) that appears larger than in other materials [72-73]; zero bandgap semiconducting properties with one type of electrons and one type of holes [74] that can also be tuned for different electronic applications [75-76].

Most of these extraordinary properties, in particular the electrical and electronic ones, have to be attributed to the unique band structures that this material has and that

were first calculated in 1947 by P.R. Wallace [77]. The valence band, formed by bonding π states and the conduction band, formed by the anti-bonding π* states are orthogonal and they touch only at six points (Dirac points indicated as K and K'). The graphene electron dispersion is linear but also very sensitive to external perturbations which can interact with the π-electron of the system (Figure 13) [78].

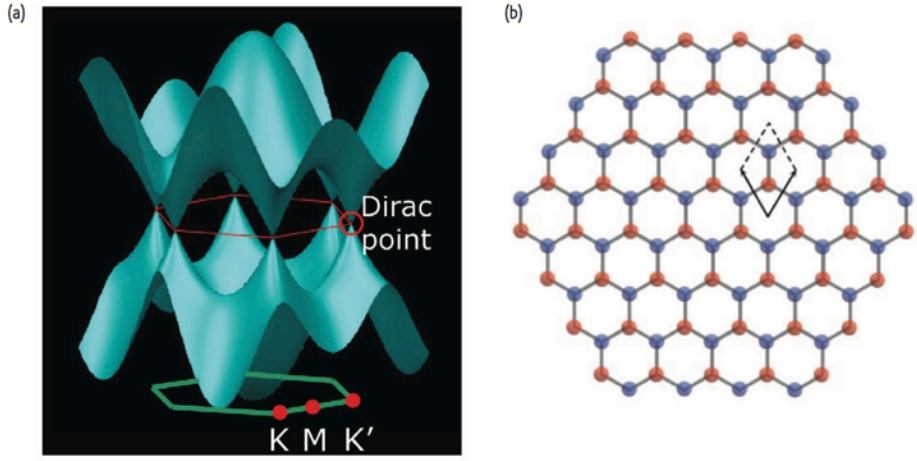

Figure 13: (a) Representation of the electronic bandstructure and Brillouin zone of graphene; (b) The two graphene sub-lattices (red and blue) and unit cell (from [78]).

It should be mentioned that graphene is not the only 2D material today that can offer great performance for a wide range of applications [79]. Boron nitride and molybdenum disulphide are in fact examples of other 2D materials that can offer the possibility to tune material and device characteristics for a specific application and can even be used in combination with graphene [80-81].

As mentioned previously, the synthesis processes available today to produce graphene can potentially achieve a better quality material with higher batch yields than CNTs, resulting in a lot of interest from the industries to make this technology available on the market. The processes available to synthesize graphene are more than ten but only five can be reasonably considered in terms of quality and scalability of the material (Figure 14) [82]:

- Mechanical exfoliation
- Chemical exfoliation
- Chemical exfoliation via graphene oxide
- CVD
- Synthesis on SiC

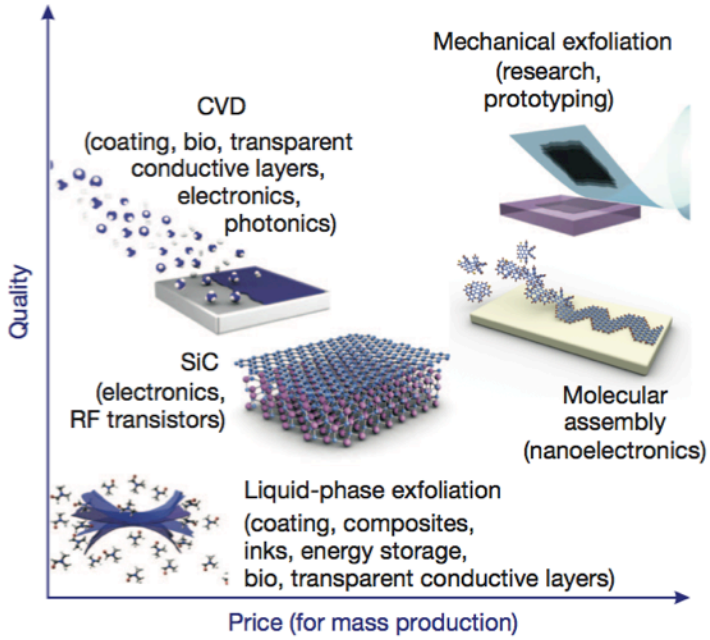

Figure 14: Several methods of mass-production of graphene, which allow a wide choice in terms of size, quality and price for any particular application (from [82]).

Each of these methods has its advantages and disadvantages in terms of quality, yield production and applications as summarized in **Error! Reference source not found.**. In particular, the mechanical exfoliation can probably produce the best samples in terms of charge carrier mobility but it is probably the worst in terms of scalability. CVD methods instead can produce pristine graphene sheets but only in limited quantities. Large quantities of graphene sheets are recently being obtained with CVD methods using catalytic metal substrates [83-84] but associated problems such as complexity of the process, harsh conditions (high temperature and high vacuum), high costs and difficulties in transferring to different substrates have still to be resolved. Also, graphene flakes have irregular shapes, that require a substrate to control the orientation for high-tech applications [78].

Other methods based on the chemical exfoliation of graphite and thermal or chemical reduction of graphene oxide can instead produce graphene on an industrial scale but unfortunately with structural defects that can affect the electronic and electrical properties [85-86].

Table 1: Properties of grapheme obtained by different methods (from [82]).

Method	Crystallite size (μm)	Sample size (mm)	Charge carrier mobility (at ambient temperature) ($cm^2V^{-1}s^{-1}$)	Applications
Mechanical exfoliation	>1,000	>1	$>2\times10^5$ and $>10^6$ (at low temperatures)	Research
Chemical exfoliation	≤0.1	Infinite as a layer of overlapping flakes	100 (for a layer of overlapping flakes)	Coatings, paint/ink, composites, transparent conductive layers, energy storage, bioapplications
Chemical exfoliation via grapheme oxide	~100	Infinite as a layer of overlapping flakes	1 (for a layer of overlapping flakes)	Coatings, paint/ink, composites, transparent conductive layers, energy storage, bioapplications
CVD	1,000	~1,000	10,000	Photonics, nanoelectronics, transparent conductive layers, sensors, bioapplications
SiC	50	100	10,000	High-efficiency transistors and other electronic devices

These are the main problems that are slowing down the production of high quality graphene on a large scale but a possible application timeline has already appeared indicating when possible electronic device prototypes could be expected in the future (Figure 15) [82].

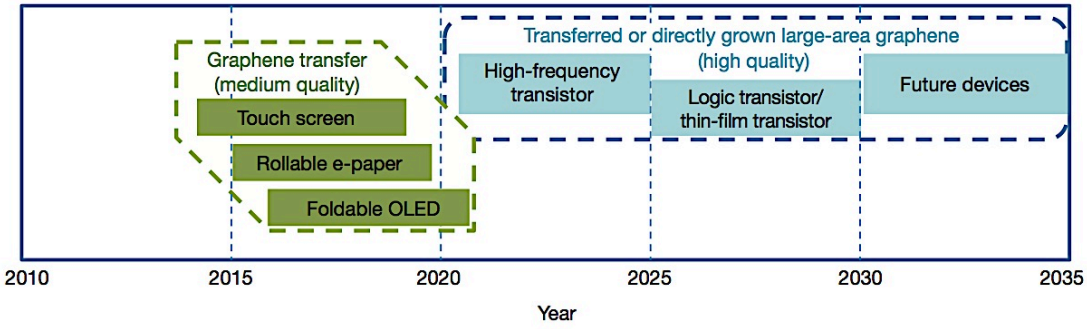

Figure15: Graphene-based display and electronic devices. Display applications are shown in green; electronic applications are shown in blue. Possible application timeline, based on projections of products requiring advanced materials such as graphene. (from [82]).

Mechanical exfoliation

The mechanical exfoliation method was historically the first one adopted by Geim, Novoselov and co-workers to isolate single layers of graphene [87]. In this method, the bulk graphite can be exfoliated into individual graphene sheets by using scotch tape and then transferring the sheet by pressing it onto a substrate such as Si, SiO_2 or Ni [88]. Typically, the bulk graphite chosen is Highly Ordered Pyrolytic Graphite

(HOPG) in order to guarantee a product of high quality graphene crystallites. The main advantages of this method are the ability to complete this process at room temperature and with inexpensive equipment. But, in terms of scalability, it is probably the worst and so it can only be considered for research purposes.

Chemical Exfoliation

It is well known that the van de Waal forces that bond together the graphene sheets to form graphite are particularly weak and can be broken by an external mechanical force. A typical example of this can be seen everyday with the usage of pencils or solid lubricants based on graphite.

Graphene can also be exfoliated from graphite by chemical methods, the process of which is very similar to the dispersion of polymers in particular solvents. This method can be explained by enthalpy and charge transfer between the graphene layers and the solvent molecules [89-90]. In particular, it was discovered that effective solvent medias are the ones with surface energies similar to graphene (~ 40-50 mJ m^{-2}) [89]:

$$\frac{\Delta H_{mix}}{V_{mix}} \approx \frac{2}{T_{NS}}\left(\sqrt{E_{S,S}} - \sqrt{E_{S,G}}\right)^2 \phi_G \qquad (1)$$

where ΔH_{mix} is the enthalpy of the mixing, V_{mix} is the volume of the mixture, T_{NS} is the thickness of a graphene nanosheet, $E_{S,S}$ and $E_{S,G}$ are the surface energies of the solvent and graphene and ϕ_G is the volume fraction of graphene dispersed in the solution. From formula (1), it is clear that the enthalpy of the mixing is minimal when the two surface energies are close or equivalent meaning that the exfoliation will take place with a mild sonication [89, 91]. Furthermore, some solvents are more suitable because they match the graphene surface energy such as N,N-dimethylformamide (DMF), benzyl benzoate, g-butyrolactone (GBL), 1-methyl-2-pyrrolidinone (NMP), N-vinyl- 2-pyrrolidone (NVP) and N,N-dimethylacetamide (DMA) while ethanol, acetone and water are considered poor solvents for exfoliation [92-93].

Other solvents, such as ionic liquids [94] and chlorosulphonic acid [95], have also been proposed for exfoliating graphite but the exfoliation mechanism has been explained differently. In fact, it has been demonstrated, in these cases, that there is a charge transfer between the solvent and the graphite layers allowing the exfoliation. Therefore, the graphene sheets could be positively or negatively charged with varying donor and acceptor numbers depending on the solvents.

Surfactants and polymers can also contribute to graphite exfoliation if mixed with particular solvents such as water. Specifically, they can change the wettability and prevent the aggregation because of electrostatic repulsion [96].

The main problem with the liquid-phase exfoliation method is that it can produce graphene for films that are not completely transparent (from 80% to 90%) with high sheet resistance (from 8 kΩ to 5 kΩ) [89, 91]. The increased sheet resistance is due to damage caused by the sonication during exfoliation.

For these reasons, electrochemical exfoliation methods are recently being employed to produce better quality graphene with a faster process [97-98]. In the electrochemical exfoliation method, the graphite or HOPG is usually connected to an electrode (anode), the counter electrode (cathode) is usually a platinum (Pt) wire and the setup is usually placed in an acidic solution (Figure 16). The complete exfoliation takes place in 15-30 min with voltages varying from 4V to 10V. The final graphene flakes produced are usually employed to make a thin film transparent electrode with a sheet resistance of 210 Ω/sq at 96% transparency [97] or to make thin film supercapacitors with capacitance values of over 1 mF/cm^2 [98].

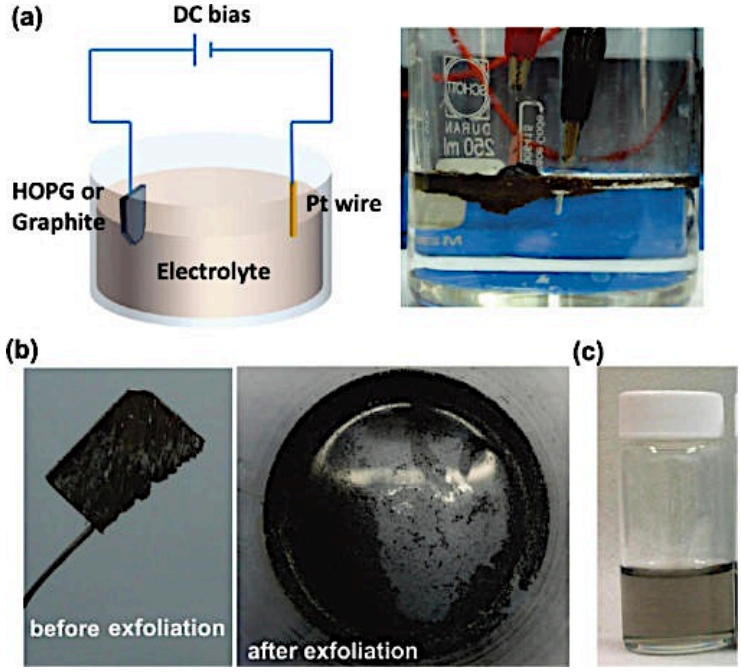

Figure 16: (a) Schematic illustration and photo for electrochemical exfoliation of graphite. (b) Photos of the graphite flakes before and after electrochemical exfoliation. (c) Photo of the dispersed graphene sheets in a DMF solution (from [97]).

Chemical or Thermal Reduction of Graphene Oxide

Graphene oxide (GO) is a semiconducting material stemming from the graphene research and can be considered a precursor of the graphene synthesis by chemical or thermal reduction [85-86, 99-100]. It recently attracted a lot of interest because of the potential to start with this material in order to have higher yield production and functionalization of the graphene sheets.

The main difference between GO and graphene is that it consists of epoxy (C–O–C) trigonally bonded in sp^2 partially sp^3 configurations, hydroxyl group (C=O) in sp^3 configuration displaced above or below the graphene plane and of some carboxylic groups (–COOH) at the edges of the graphene plane (Figure 17) [101-103].

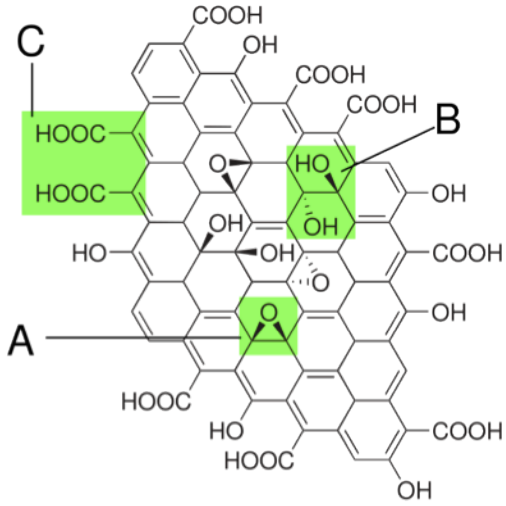

Figure 17: Chemical structure of the graphene oxide with functional groups. A: Epoxy bridges, B: Hydroxyl groups, C: Pairwise carboxyl groups (image from en.wikipedia.org/wiki/Graphite_oxide – structure from [103]).

GO exhibits excellent mechanical, optical, thermal and electronic properties that are similar to graphene because of its specific 2D structure and the presence of various oxygenated functional groups. From an electronic point of view, the GO, as synthesized, is typically insulating and has a high sheet resistance around $10^{12}\Omega/\text{square}$ [104]. This intrinsic insulating nature is strongly related to the amount C–O–C and C=O groups of this material. However, chemical and thermal treatments can help to reduce the GO in order to remove the oxygen groups with a resulting increase in the conductivity and a

tuning of the intrinsic properties from insulating to semiconducting [105]. Because of the presence of a large number of oxygen containing functional groups and structural defects, GO presents enhanced chemical activity compared with pristine graphene.

The GO can be produced chemically from graphite oxide. The graphite oxide is a compound of carbon, oxygen, and hydrogen in variable ratios, obtained by treating graphite with strong oxidizers. The first one to synthetize the graphite oxide was Benjamin C. Brodie in 1859 [106], by treating graphite with a mixture of potassium chlorate ($KClO_3$) and fuming nitric acid (HNO_3). But, in 1957, Hummers and Offeman found a safer, quicker, and more efficient way, which is largely used today in the scientific community, based on a mixture of sulfuric acid (H_2SO_4), sodium nitrate ($NaNO_3$), and potassium permanganate ($KMnO_4$) [107]. Recently, Hummers modified methods are proposed in order to have a higher fraction of well-oxidized hydrophilic carbon material with a more regular structure where the basal plane of the graphite is less disrupted [108].

The attractive property of the GO is that it can be reduced thermally and chemically to produce graphene, usually called reduced GO (rGO) [109-110]. The name rGO is given in order to differentiate it from the pristine graphene. In fact, residual functional groups and defects break the conjugate structure decreasing the carrier mobility and concentration. Current research in rGO is not only focused on removing the functional groups but also on recovering the network of the graphene lattice [111]. In fact, the rGO results in a much lower conductivity when compared to pristine graphene because of large areas of defects as demonstrated by TEM images (Figure8) [112].

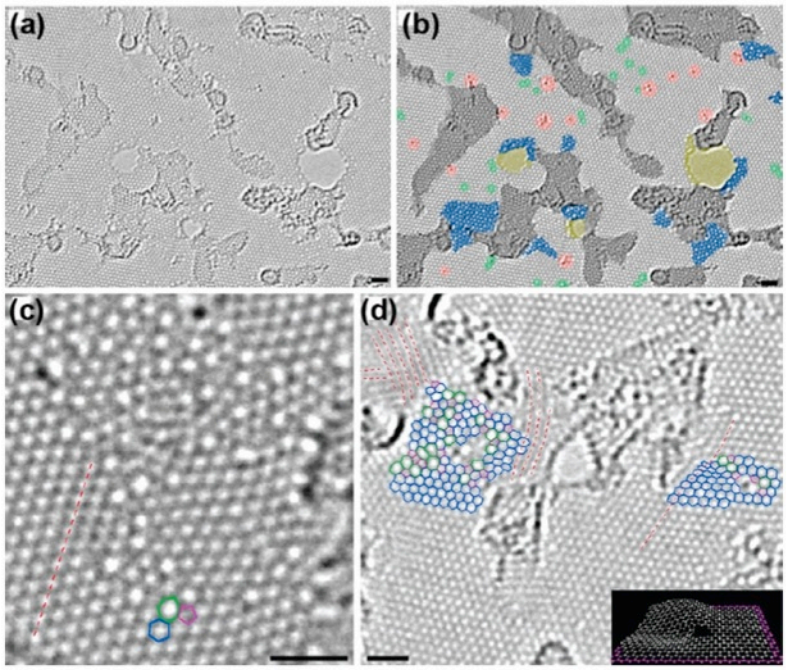

Figure 18: Atomic resolution, aberration-corrected TEM image of a single layer H-plasma-reduced-GO membrane. (a) Original image and (b) with color added to highlight the different features; (c) atomic resolution TEM image of a non-periodic defect configuration; (d) partial assignment of the configurations in defective areas, the inset shows a structural model showing clearly the strong local deformations associated with defects. All the scale bars are 1 nm (from [112]).

The GO and rGO can be easily distinguished just by optical observation [110]. The rGO usually has an increased charge carrier concentration and mobility that will improve the reflection of light if deposited onto a metallic substrate when compared to a GO film deposited on the same substrate. Instead, when immersed in a solvent such as DMF, the vial containing GO usually has a brown colour while the one with rGO appears black. The microscopic aspect of GO flakes reveals a certain wrinkling of thin and aggregated flakes stacked to each other. Their lateral sizes range from 100 nm to several μm [113](Figure 19).

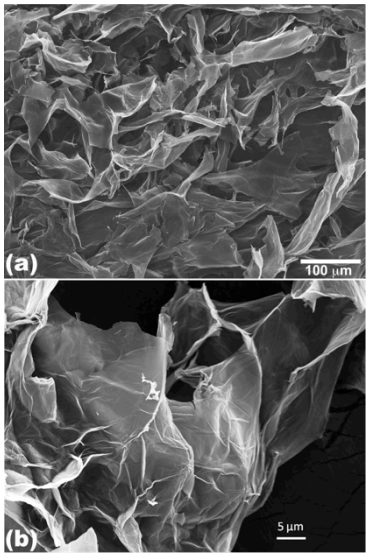

Figure 19: (a) Low magnification and (b) high magnification SEM images of graphite oxide flakes (from [113]).

Before reduction, the C/O ratio is typically 4:1-2:1 [114-115] and can be reduced to 12:1 [116] or even to 246:1 [100] as recently obtained. The C/O ratio is usually obtained by X-ray photo-electron spectroscopy (XPS) because of the possibility to easily identify all the species and their percentage values in the material (Figure 20) [117-118].

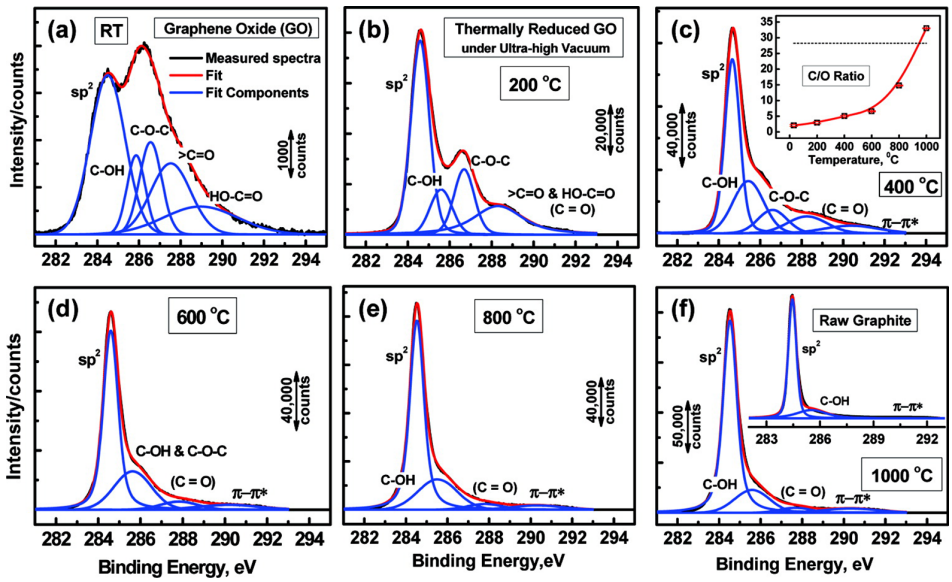

Figure 20: High resolution C1s XPS spectra: deconvoluted peaks with increasing reduction temperature (Tr). (a) Room temperature; (b) 200 °C; (c) 400 °C. The insert shows the C/O ratio as a function of T. (d) 600 °C; (e) 800 °C; (f) 1000 °C. The insert shows the C1s spectra for starting/precursor graphite (from [117]).

The thermal reduction of GO is usually carried out by annealing films or powders in the presence of inert or reducing gases or in vacuum. The annealing temperature certainly affects the properties of the rGO produced. In particular, it was found that the C/O ratio could increase from more than 7 to 13 if the temperature was increased from 500 °C to 750 °C [119]. The ratio of C/O is also directly connected to the conductivity. In fact, Peng et al.[110] demonstrated that the conductivity increased from 50 S/cm to 550 S/cm for annealing temperatures of 500 °C and 1100 °C respectively, This result has been recently confirmed and explained in details by Chambers et al. [120], and related to the loss of oxygen (Figure 12).

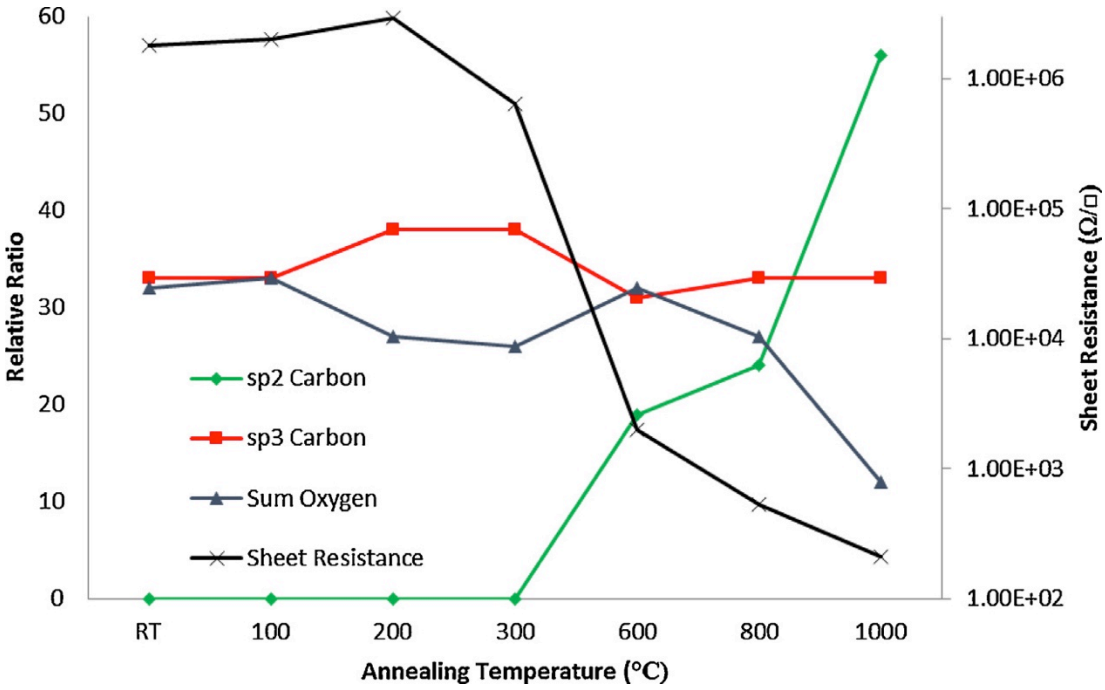

Figure 121: Plot of Sheet resistance against annealing temperature with a comparison to key carbon and oxygen ratios. It should be noted that the sheet resistance has been plotted on a logarithmic scale [120].

Wu et al. [121] used an arc-discharge system, instead of a typical furnace, to exfoliate and reduce the graphite. With this method, they were able to obtain graphene sheets with a conductivity of 2000 S/cm and a C/O ratio of ~ 18 due to the arc-discharge system that reached temperatures of over 2000 °C for a short time.

Not only the temperature but also the annealing atmosphere is very important to determine the quality of the rGO. Becerril et al. [104] demonstrated that at 1000 °C, the quality of the vacuum was critical for the quality of rGO because of the reaction with residual O_2 molecules. For this reason, the usage of reducing gases such as H_2 can help

to decrease the annealing temperatures to 450 °C and still give a high C/O ratio of ~ 15 as demonstrate by Wu and co-workers [122]. Li et al. [123] instead used a mixture of ammonia and argon (2 Torr NH_3/Ar (10% NH_3) at 500 °C to produce good quality of doped rGO.

The drawbacks of thermal reduction are the high energy consumption due to high temperatures and time consumption, considering that the GO has to reach the temperatures slowly in order to prevent an explosion of the material. For these reasons, other heating approaches based on microwave irradiation [124] and photo-irradiation have been considered because of the simplicity of these systems and the reduced exposure time [125].

A cheaper and easy way to reduce the GO is by chemical reduction because it is usually done at room temperature or with low heating [110]. Between the many chemical reagents that could reduce the GO, hydrazine and its derivatives are probably the most used by simple addition to aqueous GO solution [126-129]. The C/O ratio can reach values above 10 and a conductivity of 99.6 S/cm [85, 130]. Other compounds based on metal hybrids such as sodium hydride and sodium borohydride have also been used to specifically remove the C=O species. The main problem that occurred is that sodium borohydride, for example, does not reduce the epoxy and carboxylic groups well [131] and for this reason has to be utilized after treating the GO with concentrated sulphuric acid at 180 °C. With this method, Gao et al. [100] were able to obtain a C/O ratio of 8.6 and a conductivity of about 16.6 S/cm. Unfortunately, these values are still low when compared to the rGO obtained from the hydrazine derivative compounds.

Other reducing agents such as ascorbic acid ($C_6H_8O_6$) and hydroiodic (HI) acid are recently proposed because of their potential to obtain higher quality rGO when compared with the product obtained from hydrazine derivative compounds. Fernandez-Merino et al. [130] were able to obtain a rGO with a C/O ratio of 12.5 and a conductivity of 77 S/cm with the ascorbic acid while Moon et al. [132] obtained a rGO with a C/O ratio of 15 and a conductivity of 300 S/cm by HI acid.

Derivative approaches of the chemical method have also been employed to reduce the GO: photocatalyst reduction where the GO mixed with TiO_2 particles is exposed to an ultraviolet (UV) irradiation [133]; electrochemical reduction with an inert electrode placed in an aqueous buffer solution containing GO where cyclic voltammetry scannings are performed between certain voltage ranges [134]; solvothermal reduction

where the sealed vial containing GO in a solvent can go to high temperatures and high vapor pressures [135].

A lot of effort has been spent by the research community to make the chemical or thermal reduction processes of GO effective but the final product is still lacking in terms of quality when compared to the pristine graphene. It has to be mentioned that mildly-oxidized GO has been recently proposed because it could preserve the conjugated structure with few defects [136].

Chemical Vapour Deposition (CVD)

CVD method is commonly used to produce large area uniform graphene film [78, 137]. Similar to the CVD method to grow CNTs, graphene can be grown from gases containing C on catalytic metal surfaces or by surface segregation of C dissolved in metals such as Fe [138], Ni [139], Co, Pt and Pd [140]. The pioneer who discovered a single layer of graphite on Pt was S. Hagstrom in 1965 [141], but the first to interpret it as a single layer was J. W. May in 1969 [142]. The CVD and surface segregation can also coexist causing the carbon atoms coming from the gas source to diffuse into the metal. The process is very difficult to control above all in polycrystalline metals where the grain boundaries act as nucleation sites for multilayer growth [143]. For this reason, single crystal and atomically smooth metals are usually preferred for growing high quality monolayer graphene. Also, the choice of the metal catalytic substrate is very important to avoid the diffusion of the carbon atoms into the metal. For example, Cu surfaces are probably the best choice to have a pure CVD process with the formation of a monolayer graphene because the diffusion of C atoms in Cu is very low (0.001 at. % at 1000 °C) [84, 144]. The CVD process on Cu foils can be scalable using a roll-to-roll technique allowing for a 30 inch graphene film for a transparent electrode (Figure22(a)) [83]. However, even this method does not guarantee a perfect graphene in terms of quality. In fact, the graphene produced is mostly polycrystalline with aperiodic heptagon-pentagon pairs [145] or overlapped bilayer regions [146] at the grain boundaries (Figure22(b)). It has also been demonstrated that the presence of grain boundaries can reduce the mechanical and electrical properties of the graphene (Figure22 (c), (d)) [145, 147].

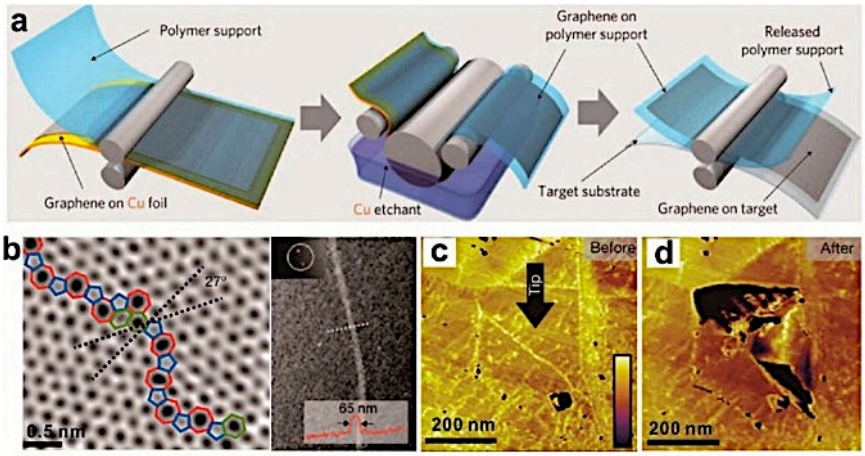

Figure 22: CVD graphene. (a) Schematic of the transfer of graphene produced on Cu using the roll-to-roll method; (b) Two types of graphene boundaries: aperiodic heptagon-pentagon pairs and overlapped bilayer regions; (c) and (d) Tears occurred along the graphene grain boundaries after indentation (from [137]).

To polish the commercial Cu foil, generally covered with protection layers, the electrochemical method is commonly used, followed by a treatment in a CVD system at 2 atm of H_2 for 7 hours to reduce the defects. In this way, ~ 2.3 mm monolayer graphene with mobility of ~ 11,000 $cm^2 V^{-1} s^{-1}$ was synthesized (Figure 23) [148].

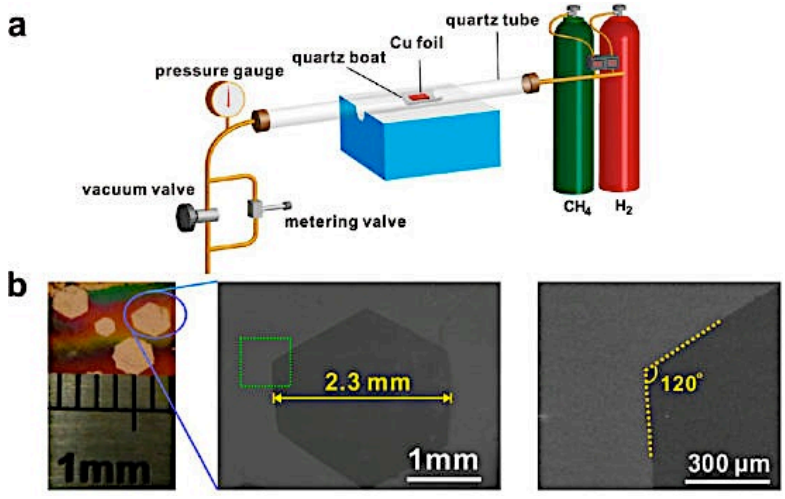

Figure 23: Millimeter-size graphene grains made on polished and annealed Cu foils. (a) Schematic of the controlled pressure CVD system; (b) Typical optical and scanning electron microscope (SEM) images of as-produced millimeter-sized graphene grains on pretreated Cu foils (from [137]).

Enclosure-like Cu structures have also been used by Ruoff's group to grow large single crystal graphene (~0.5 mm-2 mm) [149-150]. Specifically the Cu was electrochemically polished and then rolled into a tube before being placed in the furnace. They demonstrated that, with this method, the Cu inner surface is smoother than the outer one allowing the formation of millimeter-sized graphene (Figure 4).

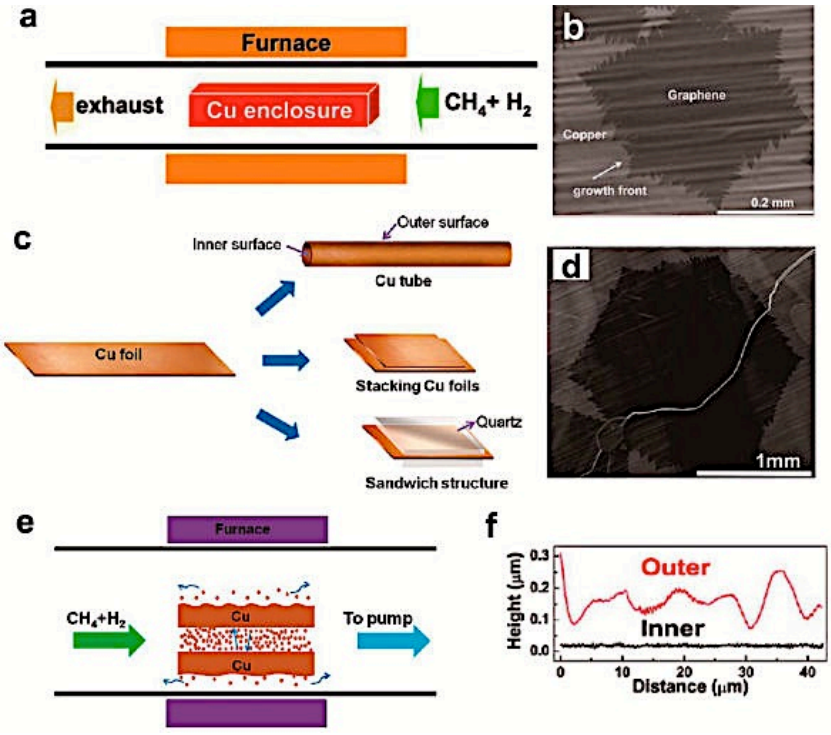

Figure 24: Millimeter-sized graphene grains made on the inside of enclosure-like Cu structures. (a) Schematic of Cu enclosures for graphene growth; (b) One SEM image of graphene grains grown on the inner surface of a Cu enclosure; (c) Schemes of Cu tube, stacked Cu foils, and Cu foil between two quartz slides; (d) Typical SEM image of one graphene grain grown on the inner surface of the tube-like Cu structure; (e) Suppression of loss of Cu by evaporation due to redeposition of Cu in a confined space; (f) Height profiles on the inner surface (the black curve) and the outer surface (the red curve) of a tube-like Cu structure after annealing (from [137]).

Mohsin et al. [151] also showed that the Cu surface morphology is very important for the graphene nucleation. In fact, by melting and resolidifying Cu substrates they were able to obtain a ~ 1 mm monolayer graphene grains because the Cu roughness decreased from 166 nm to 8 nm after treatment (Figure 5).

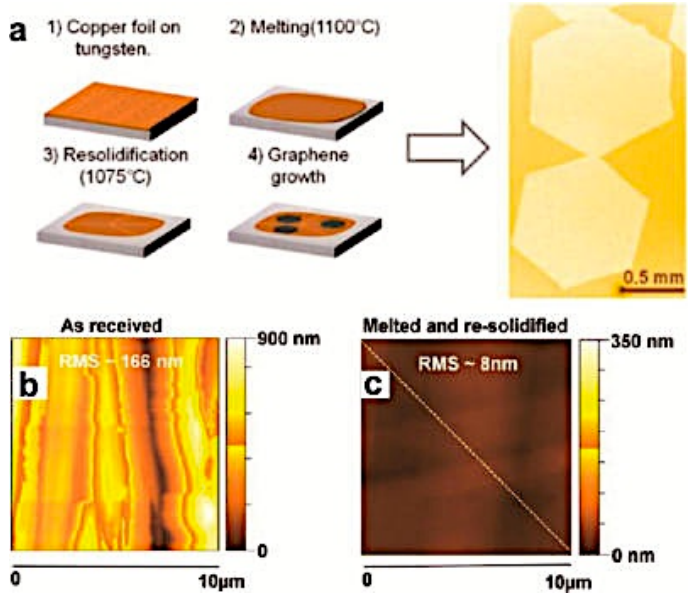

Figure 25: Millimeter-sized graphene grains made on resolidified Cu. (a) Schematic of resolidifying Cu on a tungsten substrates (left) and one optical image of millimeter-sized hexagonal graphene grains grown on resolidified Cu (right). AFM topographical images of various copper surfaces: (b) as-received and (c) resolidified (from [137]).

Another approach, reported by Zhou et al. [152], is to anneal Cu foils in Ar to keep catalytically inactive Cu_2O layer and extending the graphene growth to 48 hrs. With this method, they were able to achieve 5 mm monolayer graphene with a high carrier mobility of 16,000 $cm^2 V^{-1} s^{-1}$. Luo and Ruoff groups then adopted a similar strategy and they were able to produce centimeter scale of single crystal graphene [153-154].

The drawbacks of the CVD process are that it is expensive because a large amount of energy is required, the transfer to dielectric or other substrates is not easy to achieve and controlling the crystallographic orientation is critical for many electronic applications. However, the breakthrough that would make this technology available on a large scale production would be to develop a CVD process at a low temperature (i.e. plasma enhanced-CVD) that could produce large area high quality graphene on any kind of substrate.

Epitaxial Growth on SiC

Graphene growth on silicon carbide (SiC) has also been extensively explored because it can guarantee a wafer-scale growth, and SiC can be an excellent substrate for electronics, avoiding the transfer to another substrate. High quality graphene with a

controlled thickness and a specific crystallographic orientation can in fact be grown on commercially available semiconducting or insulating SiC wafers. For these reasons, this process is very attractive for industrial applications because it can easily be integrated with the conventional silicon technology.

SiC is a semiconducting material that can be found in 250 crystalline forms [155]. A large family of similar crystalline forms can be catalogued in particular structures called polytypes that present different physical properties.

All the polytypes show a similar local chemical environment for both the carbon and silicon species. Specifically, each C (or Si) atom is situated above the centre of a triangle of Si (or C) atoms and underneath a Si (or C) atom belonging to the next layer in a tetrahedral co-ordination with a distance between neighbouring silicon or carbon atom of ~ 3.08 Å, while the distance between the C atom to each of the Si atoms (Si-C bond length) is ~ 1.89 Å. It also exists a second type of building block that is identical but just rotated 180° with respect to the first (Figure 6) [156].

These units are periodically repeated in closed packed layers, whose stacking sequence give rise to the different polytypes.

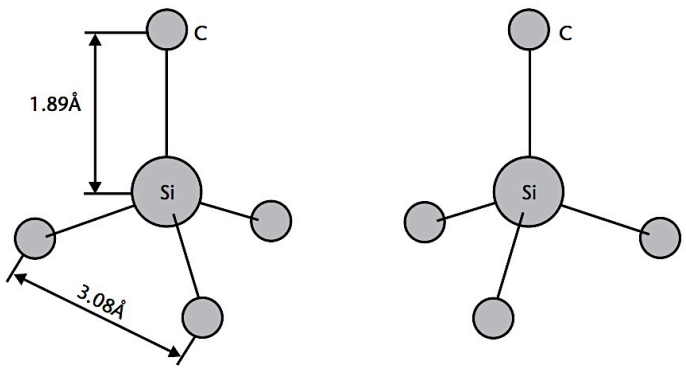

Figure 26: The characteristic tetrahedron building block of all SiC crystals. Four carbon atoms are covalently bonded with a silicon atom in the center or viceversa. Two types exist. One is rotated 180° around the *c-axis* with respect to the other, as shown (from [156]).

The two major polytypes are α-SiC and β-SiC. The α-SiC exhibits a hexagonal crystal structure (similar to Wurtzite) and is usually formed at temperatures above 1700 °C. β-SiC exhibits a cubic crystal structure with a stacking sequence of ABCABC along the (111) directions, which is typical of a zinc blende crystal structure (similar to diamond) and is formed at temperatures below 1700 °C. The α-SiC and the β-SiC can

also be catalogued with the Ramsdell classification scheme where a number indicates the layer and a letter indicates the Bravais lattice type such as Cubic (C), Hexagonal (H) or Rhombohedral (R) [157].

For example the α-SiC can also be called 2H-, 4H- or 6H-SiC depending on the unit cell while β-SiC can also be called 3C-SiC because of the ABC stacking (Figure 27).

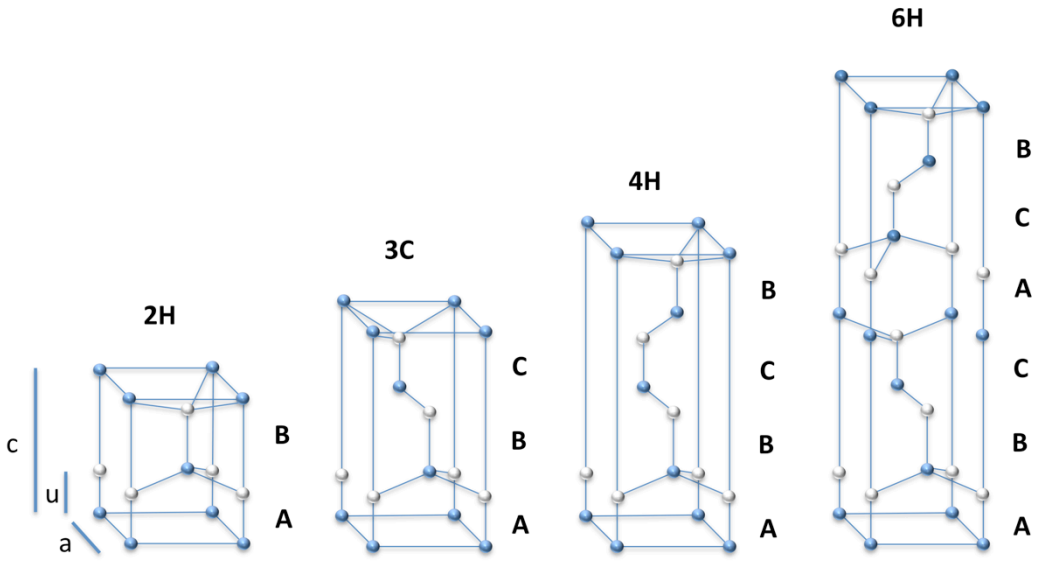

Figure 27: Schematic representation of the stacking sequence of hexagonal SiC bilayers for 2H, 3C, 4H and 6H polytypes (from [158]).

The formation process of graphene on SiC is also called graphitization. It consists of the sublimation of Si atoms from the SiC surface caused by high temperatures with a consequent rearrangement of the carbon atoms on the surface to form a graphene lattice [159-161]. Graphene can be grown on both terminated C- or Si-faces but Si allows for better control over the number of graphene layers and gives a uniform coverage with an azimuthal orientation that is determined by the crystal structure [162].

Hexagonal polytypes of SiC such as 6H and 4H with orientation (0001) are preferred because of the lattice structure that matches graphene lattice. However, 3C polytypes structure have also been used on (111) oriented surfaces in order to maintain a good match with the hexagonal lattice of the graphene [163-164].

The SiC is usually pre-cleaned in ultra-high vacuum (UHV) or in other environments with different techniques in order to increase the graphene quality during

graphitization. The three most common techniques are: heating the sample ex-situ by hydrogen (H_2) etching for 30 min at 950 °C; preparing a silicon rich phase (3×3) in a Si flux and then heating the sample for 30 min at 1000 °C; heating the sample at around 1000 °C under Si flux to remove the native oxide and to avoid silicon depletion of the surface [165].

Graphene growth occurs at temperatures of 1200-1350 °C in UHV [166-167] even if graphitic bonds start to appear at temperatures around 1000 °C [168]. Graphene can also be grown at temperatures of 1400-1600 °C in other environments like in inert gas atmospheres [169-170] or in an excess of Si in the gas phase [171] in order to reduce the sublimation rate with the positive pressure. The growth temperature is a very important parameter because it influences the number of graphene layers grown and it is directly related to the Si diffusion (Figure 28) [172],.

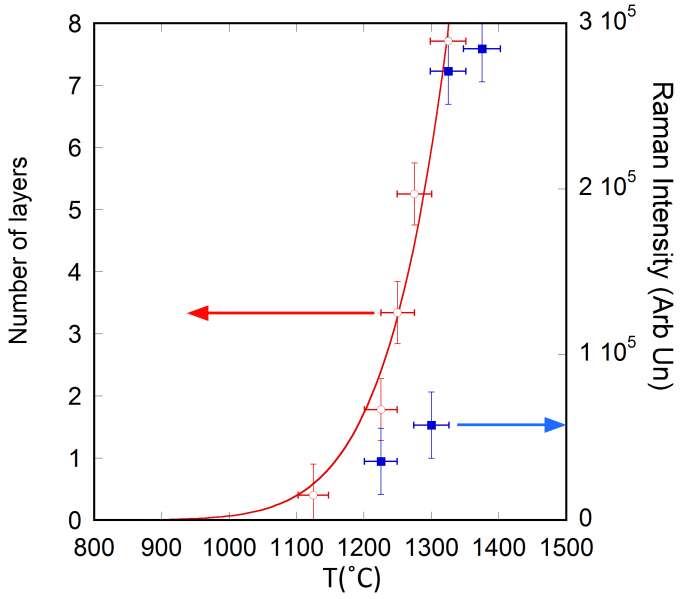

Figure 28: Number of graphene layers grown by annealing 3C-SiC for 10' in UHV as a function of T (from [166]).

The graphene can also be grown on a C face. The advantages are the absence of a buffer layer and the possibility to easily grow multi layer graphene (MLG) in all directions on the SiC surface (Figure 29(a)) [173]. The different graphene layers are not stacked in the same direction and are usually rotated about 23° with respect to each other (Figure 29 (b), (c)). It has been demonstrated that the rotationally stacked graphene has a van Hove singularity, which generates peaks in the density of the states. This property could be useful to tune the electronic properties of graphene.

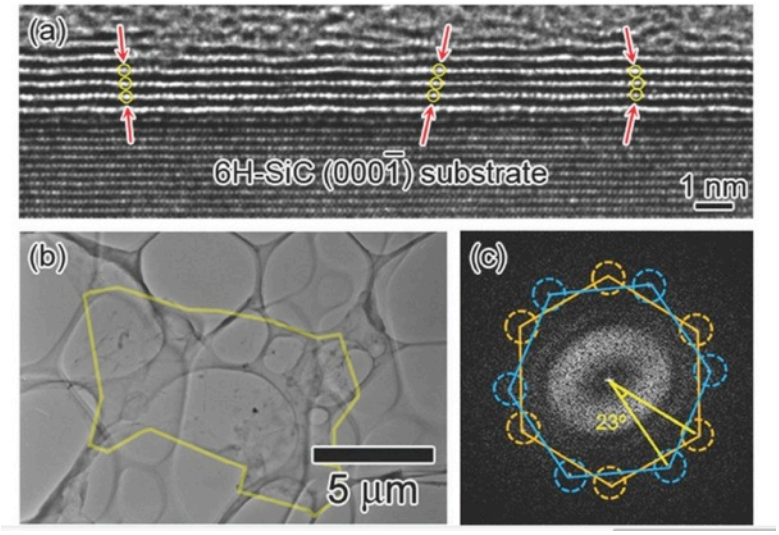

Figure 29: TEM images of MLG on the C-face. (a) The cross-sectional TEM image. (b) The low-magnification TEM image of graphene exfoliated from the SiC substrate. (c) The FFT pattern from the area in (b) (from [173]).

One potential application of the graphene grown on SiC is in high frequency transistors. A pioneering work was completed in 2006 by Berger et al. [174] by fabricating a field-effect transistor (FET). They were able to show the Dirac nature and the high mobility (25,000 $cm^2 V^{-1} s^{-1}$) of graphene grown on SiC. An IBM research group recently reached a 300 GHz cut off frequency of a graphene FET grown on SiC and showed the stable operation of an integrated circuit containing graphene (Figure 30) [175-176].

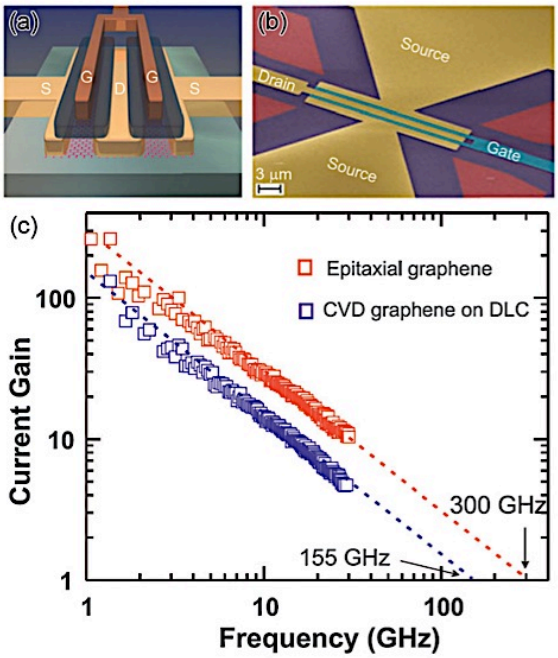

Figure 30: High frequency graphene transistor. (a) and (b) Structure of graphene FET for an analogue radio frequency device. (c) Current gain as a function of frequency, showing a cutoff frequency of 300 GHz for epitaxial graphene on SiC (from [175]).

The two major drawbacks of this graphene synthesis process are the high costs of the SiC wafers and the high temperatures involved that are not suitable for the Si technology [82]. The first drawback is being solved by growing thin layers (100-300 nm) of SiC on top of Si substrates but still further development is required to have a uniform deposition on a large diameter wafer with a low roughness and elimination of the terraces in order to guarantee high quality monolayer graphene. The second drawback could be solved, as in the CVD process, by reducing the growth temperatures with the use of PE-CVD equipment. Industries and research groups worldwide are deeply looking at solving this problem because it could contribute to the launch of graphene into the electronic market.

3 Organic Photovoltaics

Over the past twenty years, organic photovoltaics improved rapidly because of the potential to obtain a manufacturing process that is faster, less expensive and with higher production volumes when compared to the silicon technology [177-180]. Figure 31 shows the best solar cell efficiencies reported by the National Renewable Energy Laboratory (NREL) in the United States in the last 40 years. It is noticeable that the organic solar cell efficiencies increased from 4% to 12 % (record established by Heliatek in 2013 for a tandem organic solar cell) in just a little over ten years [181].

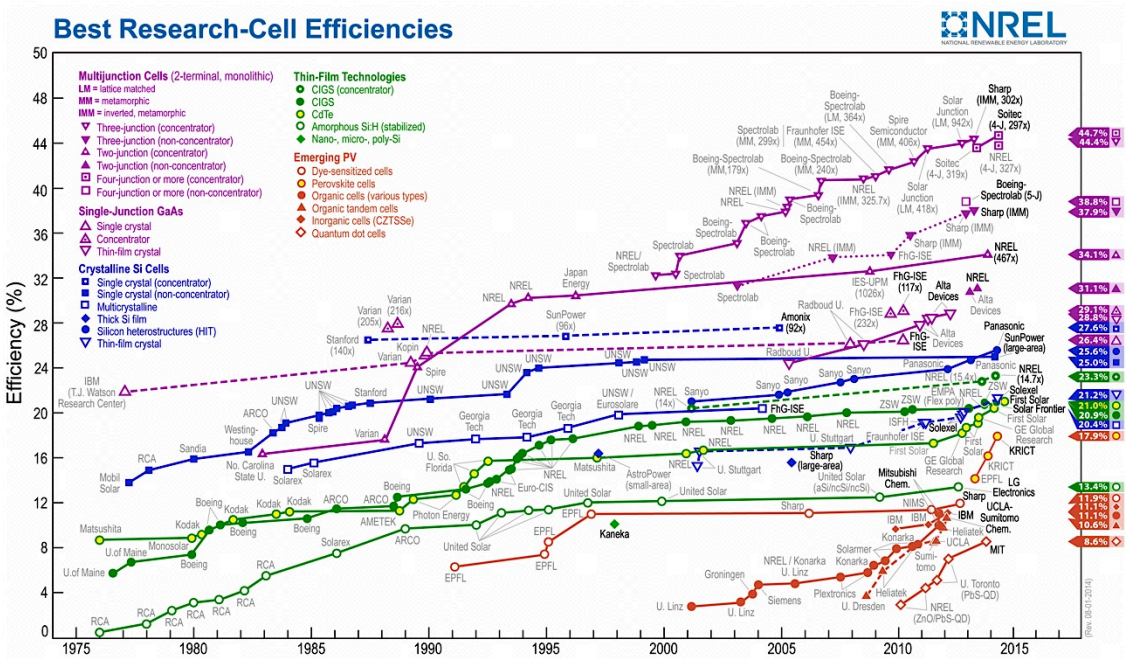

Figure 31: Record solar cell efficiencies worldwide reported by NREL in 2014 (from [182]).

Three problems still have to be solved in order to make this technology competitive with others already present on the market: the power conversion efficiency (PCE) [183], the device lifetime [184] and the large scale production [185].

The common structure of an organic solar cell consists of two electrodes (in which one of the two has to be transparent) and an active layer between them where the generation of free charge carriers will occur. A buffer layer is usually included between each electrode and the active layer in order to prevent the charge recombination, which reduces the efficiency of the device. The active layer can be a double layer [one has a

stronger affinity for electrons (donor) and the other has a stronger affinity for holes (acceptor)] or a bulk heterojunction (mixture of a donor and acceptor material in bulk). The bulk heterojunction (BHJ) provides a larger volume of paths for the transport of free carriers and more efficient charge separation in comparison to the other structures [186-188]. The first kind of BHJ architecture was originally proposed by Sariciftci et al. [189] and is based on an active blend of a conducting polymer (electron donor material) mixed with fullerenes derivatives (electron acceptor material) [190].

The generation of a photocurrent due to light incident upon an organic solar cell device consists of three steps (Figure 32) [191-192]:

1. Photon absorption in the conducting polymer (donor material).
2. Creation of an exciton. An exciton is a bound state of an electron and a hole which are attracted to each other by the electrostatic Coulomb force. Its diffusion length is about 10 nm.
3. Exciton separation at the interface between the donor and the acceptor. Because of the built-in electric field at the interface, the electron is transferred to the acceptor and the hole to the donor (creation of the photocurrent).

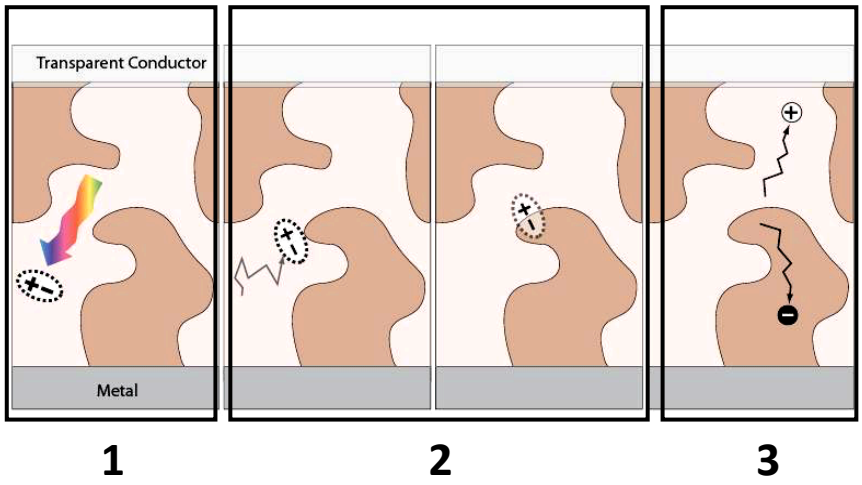

Figure 32: Photocurrent generation steps in an organic solar cell. Step 1: photon absorption in the conducting polymer (donor material). Step 2: creation of an exciton. Step 3: exciton separation at the interface of the heterojunction (interface between the donor and the acceptor).

One problem is the short lifetime of excitons generated by the light. Considering that their recombination distance is between 4 nm and 20 nm [193-194], the active layer morphology is an important parameter for the performance of the device [195-197].

3.1 Fullerene derivatives in organic solar cells

At present, the most studied BHJ solar cells are based on fullerene derivative [6,6]-phenyl-C61-butyric acid methyl ester ($PC_{61}BM$) as the acceptor material and conducting polymer poly(3-hexylthiophene-2,5-diyl) (P3HT) as the donor material [198-200]. Both materials are commercially available and guarantee stable devices. In the regular structure, Indium Tin Oxide (ITO) is typically used as the transparent conducting anode and poly(3,4-ethylenedioxythiophene):poly(styrene sulfonate) (PEDOT:PSS) as the electron blocking layer. The blend of PCBM and P3HT is the active layer, onto which a thin layer of lithium fluoride (LiF), used to block holes, and a layer of aluminium as cathode are coated respectively. (Figure 33 (a)) [201-202]).

The specific choice of these materials is due to the fact that the exciton separation at the interface acceptor/donor and the transport of the charges across the device is strongly affected by the energy band alignment. Figure shows how, in a regular structure, the electrons and holes can easily move from the donor/acceptor interface to the respective electrodes because the energy values of the lowest unoccupied molecular orbital (LUMO) and the highest occupied molecular orbital (HOMO) of each material are very similar [26].

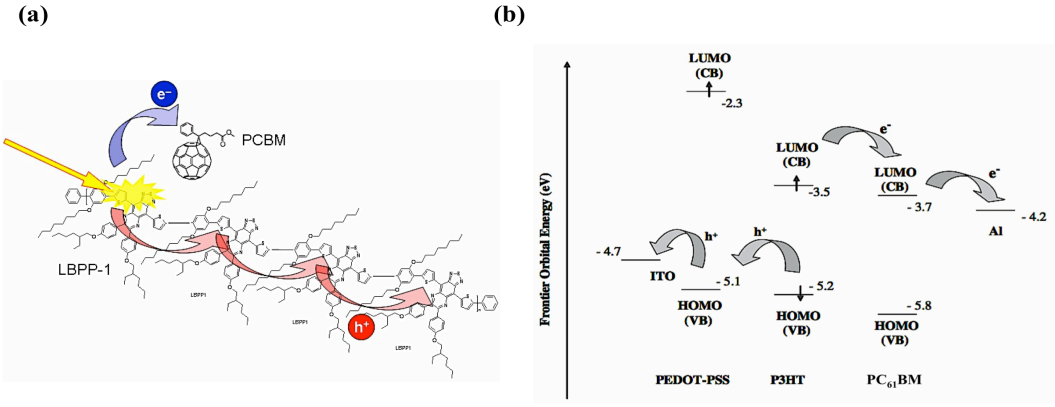

Figure 33: (a) Electron transfer from P3HT to PCBM after generation of the exciton at the interface of the two materials. (b) HOMO and LUMO of the different materials in an organic solar cell structure ITO/PEDOT:PSS/P3HT:$PC_{61}BM$/LiF/Al (from [26]).

An organic solar cell device can also have a reversed structure by inserting a hole blocking layer between the transparent electrode and the active layer in order to collect electrons and an electron blocking layer on the metallic electrode in order to collect holes. Figure 34 (b) shows a typical inverted structure composed of ITO as the cathode, zinc oxide (ZnO) as the hole blocking layer, $PC_{61}BM$:P3HT as the active layer, the PEDOT:PSS as the electron blocking layer and gold (Au) as the anode [203].

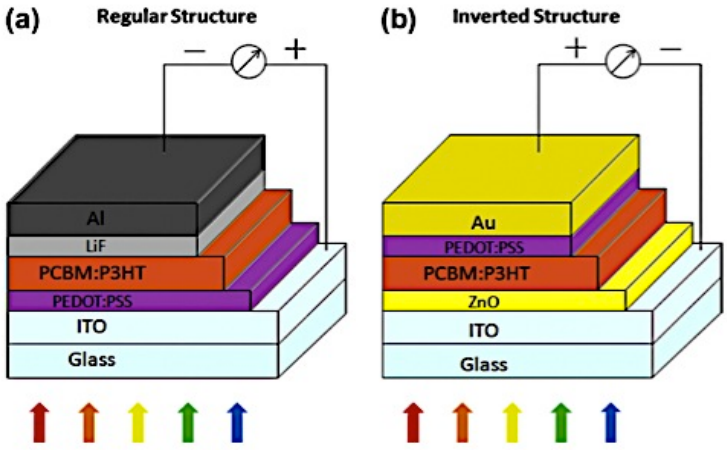

Figure 34: (a) Schematic of a regular organic solar cell structure; (b) Schematic of an inverted organic solar cell structure (from [204]).

In order to characterize the performance of an organic solar cell, the electrical current (I) and the voltage potential (V) across the device are measured and plotted on y and x axis, respectively, under a standard illumination (Figure 36). The current produced by a solar cell is the combination of the current (I_D) of the solar cell diode in the dark with the light-generated current (I_L) (Figure 35).

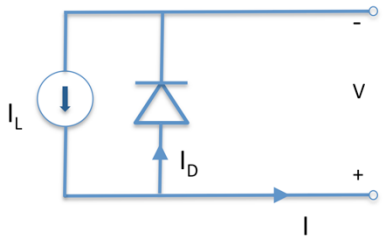

Figure 35: Simple equivalent circuit for a solar cell

The total current calculated from the circuit in Figure 35 is [205]:

$$I = I_0 \left[\exp\left(\frac{qV}{nKT}\right) - 1\right] - I_L \qquad (2)$$

The I-V curve of a solar cell is the superposition of the I-V curve of the solar cell diode in the dark described by the Shockley diode equation with the light-generated current. The light has the effect of shifting the I-V curve down into the fourth quadrant where power can be extracted (Figure 36).

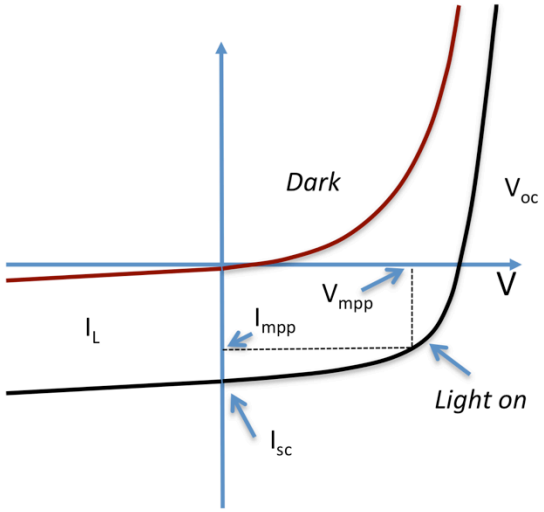

Figure 36: I-V curves of a solar cell. I_L indicates the current under illumination. V_{oc} and I_{sc} represent the open circuit voltage and the short circuit current respectively, while V_{mp} and I_{mp} indicate the maximum power point.

Typical resistive effects are unfortunately present and they contribute to reduce the performance of the device. The most common parasitic resistances are series resistance (R_S) and shunt resistance (R_{SH}). R_S and R_{SH} have to be included in a more complicated equivalent circuit model (Figure 37).

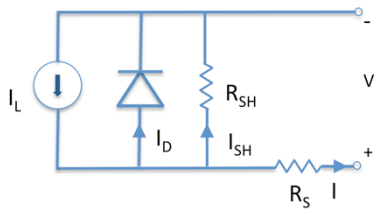

Figure 37: Detailed equivalent circuit for a solar cell

The efficiency η of a solar cell can be calculated from the I-V curves in Figure 36 [205]:

$$\eta = \frac{V_{oc} I_{sc} FF}{P_{in}} \qquad (3)$$

where V_{oc} is the open circuit voltage, I_{sc} the short circuit current and FF is the fill factor that indicates the "squareness" of the I-V curve. The FF can also be calculated from Figure 36 [205]:

$$FF = \frac{V_{mp} I_{mp}}{V_{oc} I_{sc}} \qquad (4)$$

where V_{mp} and I_{mp} correspond to the maximum power point on the I-V curves.

The remarkable properties of the carbon nanomaterials described previously make them very attractive for use in organic photovoltaics [16].

Fullerenes (C_{60}) were the first to be proposed because they have a response typical of n-type semiconductors and are able to accept electrons coming from the photo-excitation of the conducting polymer [206]. The first heterojunction based on C_{60} was realized in 1993 [207]. Unfortunately, the performance of the device was still limited by the fact that the C_{60} could not disperse well and penetrate into the conducting polymer. For this reason, C_{60} derivatives were proposed because of their ability to diffuse into the polymer film and to form an intermixed layer. In particular, the 1-(3-methoxycarbonyl)propyl-1-phenyl[6,6]methanofullerene or [6,6]-phenyl C_{61}-buyric acid methyl ester ($PC_{61}BM$) derivative is more soluble in organic solvents than pristine C_{60} [35]. Currently, many stable devices are prepared with a mixture of different conducting polymers and $PC_{61}BM$ achieving a stable PCE of about 4% [208].

Because the $PC_{61}BM$ has small absorption peaks, other fullerene derivatives such as phenyl-C_{71}-butyric acid methyl ester ($PC_{71}BM$), have recently been used to guarantee a better absorption in the visible spectra [209] boosting the PCEs to values higher than 7% (Figure 38) [210].

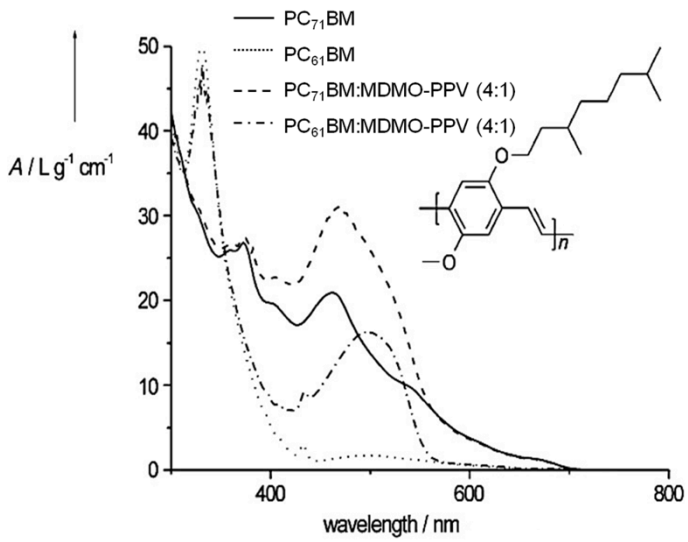

Figure 38: UV/Vis spectra of $PC_{71}BM$ and $PC_{61}BM$, both in toluene. To illustrate the contribution of MDMO-PPV to the absorption, the (normalized) spectra of $PC_{71}BM$:MDMO-PPV and $PC_{61}BM$:MDMO-PPV, also in toluene, are represented. The inset shows the structure of poly(2-methoxy-5-[3',7'-dimethyloctyloxy]-p-phenylene vinylene) (MDMO-PPV) (from [209]).

Other fullerene derivatives and C_{60} functionalized macromolecules have also been proposed for the preparation of all polymer type solar cells but the performances had always been very low due to the presence of large solubilizing groups that decrease the charge transport [211].

3.2 Carbon nanotubes in solar cells

CNTs have also been used in organic solar cells to replace fullerenes as acceptor material. Because of their high aspect ratio, electrical conductivity, tuneable optical and electronic properties, the quantity of CNTs introduced into the device could be significantly lower when compared to the amount of PCBM [212]. In fact, the ratio of PCBM and P3HT in the blend is usually 1:1. However, for CNTs, it could be much lower (~ 3% in weight of the P3HT) [213]. CNTs have been replacing either partially [214] or completely [213] the PCBM compounds in organic solar cells. For example, when they are mixed with P3HT, the polymer chains tend to wrap the CNTs with an electron transfer between the CNTs and the P3HT as demonstrated by Figure 39 [215-216] and experimentally observed by SEM and TEM images (Figure 40) [217-218]. This interaction is usually stronger if the SWNTs are semiconducting instead of metallic

[219-220]. Heterojunctions between SWCNTs and P3HT molecules that have been studied by means of scanning tunnelling microscopy and computer simulation open possibilities for making novel solar cells [221-222]. Devices were made by blending CNTs with the P3HT, with the maximum efficiency of 3.36% [223]. However, by blending the N-doped MWCNTs into a mixture of PTB7 and $PC_{71}BM$, the device reaches a high efficiency of 8.6%. It was concluded that the incorporation of N-MWCNTs leads to not only increased nanocrystallite sizes but also smaller phase-seperated domain sizes of both PTB7 copolymers and $PC_{71}BM$. N-MWCNTs serve as both exciton dissociation centers and charge transfer channels.

p-type SWCNTs can be easily obtained by chemical doping. A common method is the nitric acid treatment of CNTs, which introduces nitrogen dopants as well as increases the electrical conductivity [224-225]. The PEDOT:PSS can cause a degradation of the active layer and of the ITO electrode because of its hygroscopicity and acidity which results in a decrease in the lifetime of the solar cell device [226]. Hence, the network film of *p*-type SWCNTs has been used to replace the PEDOT:PSS buffer layer in organic solar cells, with a device structure of ITO/SWCNTs/P3HT:PCBM/Al [227-228]. Using SWCNT film as the hole transport layer, the energy conversion efficiency of the organic solar cell is equivalent to that of the component device with PEDOT:PSS.

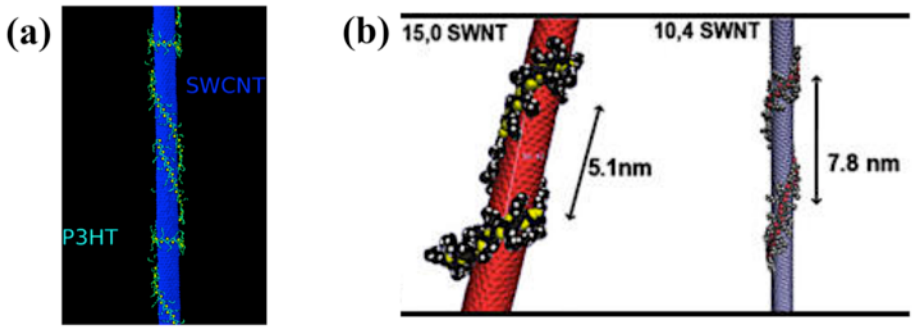

Figure 39: (a) Molecular dynamics simulations of the P3HT wrapped around a SWNT (15,0) (from [216]). (b) Helices form on (15,0) and (10,4) SWNTs during the folding of P3HT with orthogonal initialization. The chirality may affect the pitch distance to some extent (from [215]).

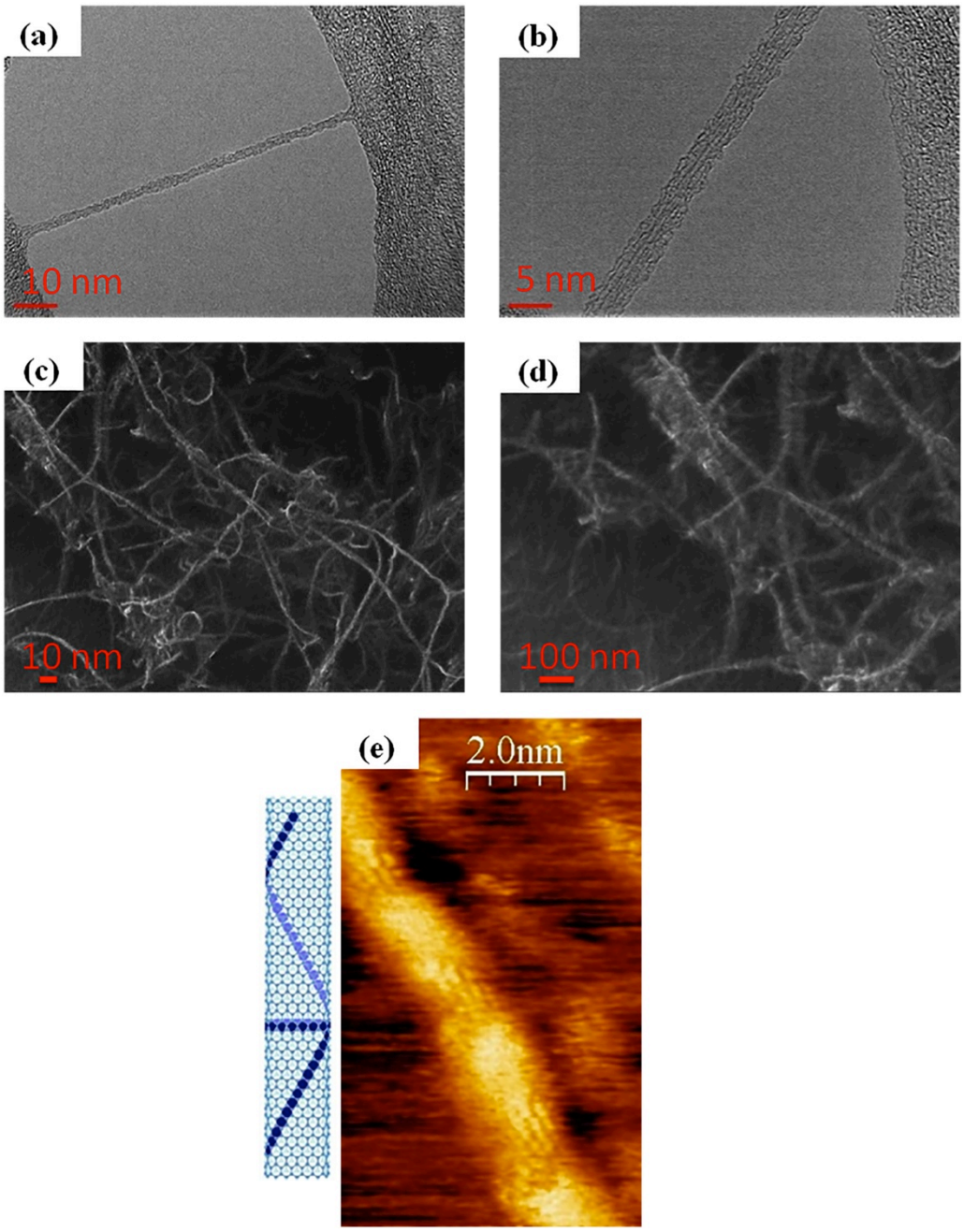

Figure 40: (a) and (b) TEM images of P3HT wrapping a SWNT (7,6) (images taken at QUT, not yet published). (c) and (d) SEM images of P3HT wrapping bundles of SWNTs (7,6) (images taken at QUT, not yet published). (e) STM image and schematic of P3HT wrapping a SWNT (15,0) (from [229]).

Efforts have also been paid to the development of hybrid solar cells with the structure of *p*-CNT/*n*-Si. By coating a transparent *p*-type SWCNT network film onto a Si substrate, the solar cell is formed and the energy conversion efficiency can be >11% [230]. By coating a layer of MoO_x onto the CNT film, the efficiency reaches 17 % [231].

In fact, CNTs can be grown directly on the ITO substrate [232-233]. In device fabrication, the mixture of P3HT and PCBM is coated onto the substrate, and CNTs are used as 3D electrodes to collect charges from the active media. The problem is that MWCNTs grown at relatively low temperatures onto the ITO glass are tens of nanometers thick and have low areal density. With such a substrate the energy conversion efficiency of organic solar cell is lower than 1%. The best result so far, 2.1% energy conversion efficiency, was obtained in 2013 by growing CNTs onto fluorine doped tin oxide (FTO) glass, which is more resistant to high temperature than ITO [234].

Other research groups are focusing their work on replacing the ITO, which is expensive and brittle, with a carpet of CNTs in bundles because of their optical transparency, high conductivity properties and the potential to be deposited onto a flexible substrate [235-236].

3.3 Graphene in solar cells

More recently, graphene and its derivatives have also been proposed for organic solar cells. In particular, pristine graphene can be used as a transparent electrode similar to the CNTs carpet (Figure 41) [237-239].

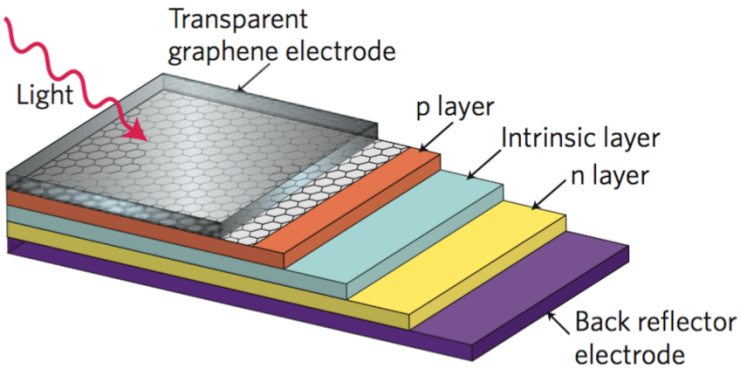

Figure 41: Schematic of an organic solar cell with a transparent graphene electrode (from [239]).

Graphene can hardly be found in the active or buffer layers, because of its zero band gap structure, but the introduction of functional groups could open up more possibilities of graphene integration into different layers of an organic solar cell device. On the other hand, GO can easily be integrated into organic solar cells because of its

semiconducting behaviour that can be finely tuned as a function of the degree of oxidation.

GO has been employed in the active layer for the effective exciton charge separation and charge transport when mixed with a conducting polymer, such as P3HT, because of the large surface interface area acceptor/donor and continuous pathway similar to CNTs [240-242]. In order to increase the solubility in typical organic solvents (e.g. dichlorobenzene), used to disperse the conducting polymers, the GO can be functionalized with other compounds such as phenyl isothiocyanate (PITC) (Figure 42) [241].

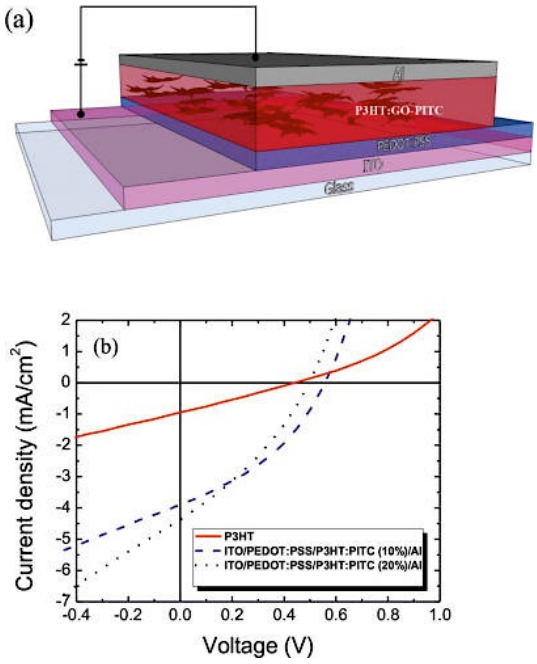

Figure 42: (a) Schematic of a photovoltaic device with P3HT:GO- PITC thin film as the active layer and the structure ITO/ PEDOT:PSS(30 nm)/P3HT:GO-PITC(110 nm)/Al(80 nm). (b) Experimental J-V curves of the photovoltaic devices based on P3HT (red curve) and P3HT:GO-PITC composites (blue curve, 10 wt %; black curve, 20 wt %) after post fabrication thermal annealing at 160 °C for 20 min (from [241]).

GO has been largely used in the organic solar cell field for the buffer layers. Specifically, it could be a valid candidate to replace the PEDOT:PSS as the electron blocking layer because it presents values of work function very similar to the PEDOT:PSS (4.6-4.8 eV) (Figure 43) [243-246].

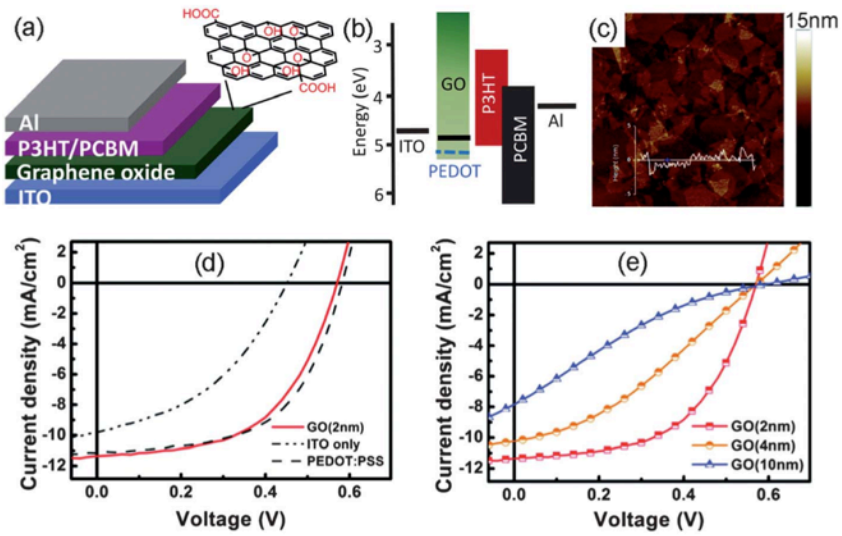

Figure 43: (a) Schematic illustration of a device structure with GO as the buffer layer. (b) Energy level diagrams of the bottom electrode ITO, interlayer materials (PEDOT:PSS, GO), P3HT (donor), and PCBM (acceptor), and the top electrode Al. (c) An AFM height image of a GO thin film with a thickness of approximately 2 nm. (d) Current density-voltage (J-V) characteristics of the devices with no HEL, with 30 nm PEDOT:PSS film, and with 2 nm GO film. (e) J-V characteristics of the ITO/GO/P3HT:PCBM/Al devices with the GO layer of different thicknesses (from [245]).

If chemically modified with specific dopants, such as caesium (Cs) atoms, it could also be used as an electron-blocking layer because its work function can be reduced to 3.9-4.1 eV (Figure 44) [243, 246].

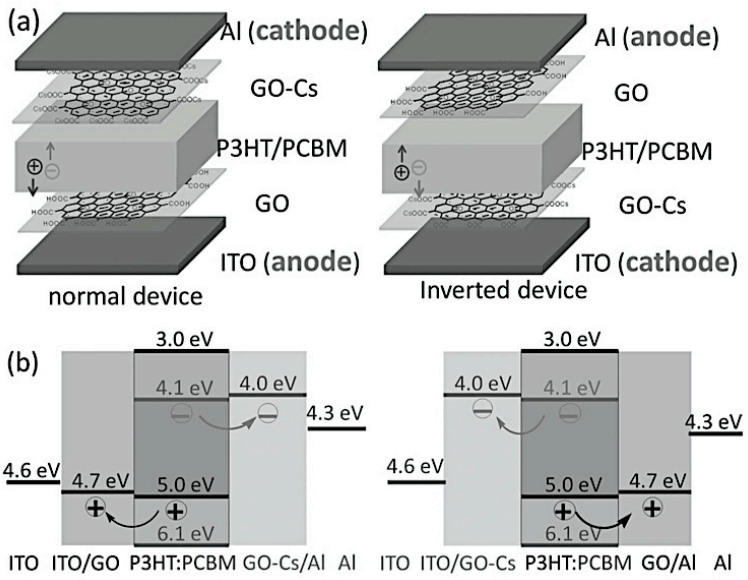

Figure 44: Device structures (a) and energy level diagrams (b) of the normal device and the inverted device with GO as the hole-extraction layer and GO-Cs as the electron-extraction layer (from [243]).

Because of the high sheet resistance of the GO, the addition of some SWNTs in the blend can decrease the through-thickness resistance of the GO film by an order of magnitude if used as a buffer layer (Figure 45) [247].

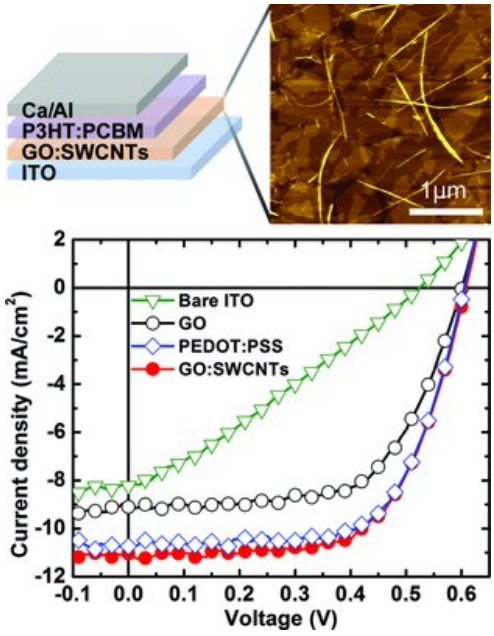

Figure 45: Addition of a small amount of SWCNTs into the GO buffer layer can increase the FF and JSC of devices with GO (from [247]).

Bernardi et al. [248] were the first to demonstrate the possibility to have a solar cell with the presence of only carbon nanomaterials in the active layer without the use of any conducting polymer. In their work the active layer was composed of only $PC_{71}BM$, semiconducting SWNTs, and reduced GO, achieving a PCE of 1.3%. They also used ab initio calculations to demonstrate efficiency limits of up to 13% for this device, which is comparable to those predicted for polymer solar cells (Figure 46).

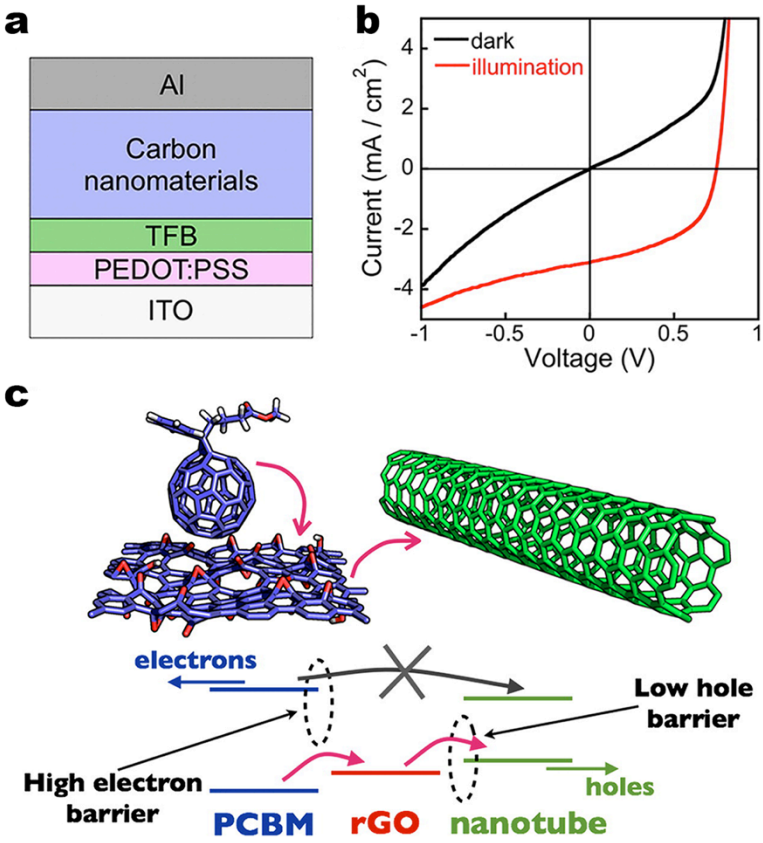

Figure 46: (a) Structure of carbon solar cells where TFB and PEDOT:PSS are the electron-blocking and hole-conducting layer , respectively, deposited on top of the ITO. For the best-efficiency device, a blend of rGO, $PC_{71}BM$, and s-SWCNT with a diameter of 1.2-1.7 nm is used as the active layer, which is denoted by "carbon nanomaterials". (b) Current-voltage curves in the dark and under simulated sunlight illumination of the device. (c) Interface of $PC_{71}BM$/rGO sheet/s-SWCNT. Hole carriers photogenerated within PCBM are transferred to rGO due to a large Schottky barrier for electrons, as shown by pink arrows, and then to s-SWCNT (from [248]).

In 2011, a research group at Stanford University proposed for the first time a solar cell based entirely on carbon nanomaterials in two architectures, one vertical and one horizontal (Figure 47) [249].

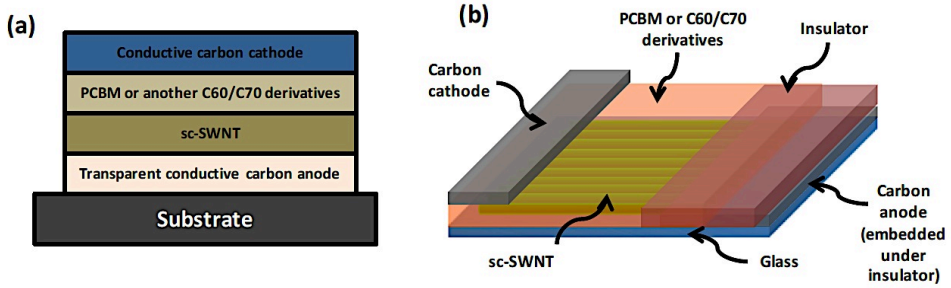

Figure 47: Schematic of the two basic solar cell device structures: (a) a typical vertical structure. An inverted vertical structure is also possible, where the conductive cathode will be in contact with the substrate; (b) A horizontal structure that will take advantage of aligned SWNTs or aligned C_{60} microribbons (from [249]).

In 2012, the same group was able to fabricate and test a complete carbon based solar cell device achieving a PCE of only 5.7 x 10^{-3} % but they were the first worldwide to demonstrate an efficiency from a device composed solely of carbon nanomaterials [250]. A transparent electrode based on rGO was used as the anode and n-type-doped SWNTs as the cathode. Sunlight was absorbed by the semiconducting SWNTs to generate excitons that were split in the active layer composed by SWNTs and $PC_{61}BM$ [250].

Despite the use of new compounds in the active layer or novel carbon nanomaterials, such as fullerene derivatives and SWCNTs, and the implementation of new architectures, the PCE is still limited by the low photon absorption of the active layer. Though carbon nanomaterials are strong light absorbers, their percentage in the active layer is optimized to achieve the maximum PCE; Also thickness of the active layer is usually below 1 μm because adding the thickness is unfavourable for exciton extraction. At present, tandem organic solar cells based on the combination of a high band gap and a low bandgap polymer represent a reliable way to achieve a maximum spectral range for the photoabsorption in the device but do not provide a valid mechanism to trap the most incoming photons in terms of light-electrons conversion [251].

Graphene has also been involved in solar cells other than the organic ones. By coating CVD graphene onto a n-type Si, Schottky junction solar cells with efficiencies up to 1.5 % were made by Li et al [252]. The efficiency of such type of solar cell was increased to 8.6 % under AM 1.5 illumination by chemically doping the graphene sheets with bis(trifluoromethanesulfonyl)amide[$((CF_3SO_2)_2NH)$] [253]. By doping the CVD graphene film coated onto *n*-Si with HNO_3 and subsequently spin coating a layer of colloidal TiO_2 antireflection film, Shi *et al* improved the solar cell efficiency to 14.5 % under standard illumination [254]. Graphene films in dye-sensitized solar cells are mainly used as counter electrodes, which outperform platinum electrodes in some cases [255-258].

4 Supercapacitors

Electrochemical capacitors (ECs) have been known by different names such as “ultracapacitors” or “power capacitors” but the most recognized name today is “supercapacitors”. The term supercapacitor was introduced by NEC because it was the first company to commercialize a device with the name SuperCapacitor^{TM} in 1971 [259].

Supercapacitors have been developed since 1957 when Becker [260] first used carbon flooded with a sulphuric acid electrolyte to develop a charge storage at the interface between these two materials. But, it took until 1969 for the company SOHIO [261] to launch this technology into the market. The real success of supercapacitors started in the nineties when government programs in the US began giving funds for this technology to be incorporated into hybrid vehicles for providing necessary power for acceleration [262]

Supercapacitors can provide a higher power density but a smaller energy density compared to traditional chemical batteries, which make them very attractive for applications where instantaneous power is required. The other key characteristics of supercapacitors are: ability to charge-discharge within seconds; a long lifetime of more than 10^6 cycles; environmentally friendly; stable operation at different temperatures. Figure 48 shows a typical energy density vs. power density plot, also called Ragone plot, that compares different energy storage devices. It can be noticed that supercapacitors fill the gap between capacitors and batteries [263].

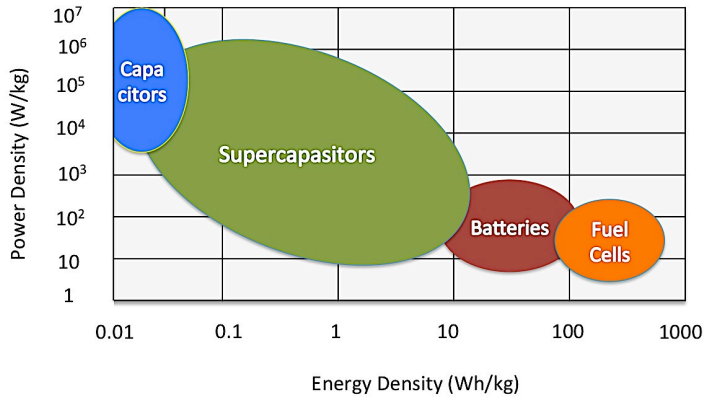

Figure 48: Energy density vs. Power density (Ragone plot) for various energy-storing devices (from [263]).

Today several companies such as Maxwell, FastCap Systems, NEC, Panasonic, Tokin and even car companies such as Volvo are investing further in developing this technology because of the possibility to have a large amount of energy in a small component that can be easily integrated into a device. Volvo for example is working at reducing the weight and increase the space in an hybrid vehicle by incorporating supercapacitors in the frame of the car (**Error! Reference source not found.**) [264].

Supercapacitors are typically divided in two categories: electric double-layer capacitors (EDLCs) and pseudo-capacitors. A subcategory called hybrid capacitors can be identified if the EDLCs and the pseudo-capacitors are combined together into a single device (Figure 49) [259].

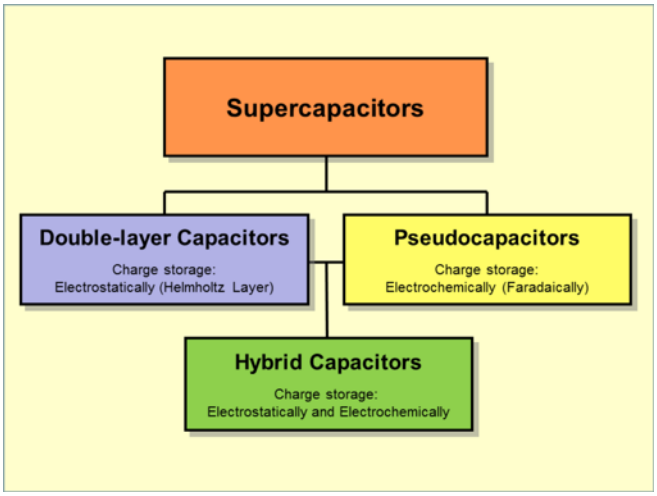

Figure 49: Hierarchical classification of supercapacitors and related types (from [265]).

EDLC stores the energy typically at the electrode/electrolyte interface as shown in Figure 50. During the charging phase, an external electric field applied to the device moves the ions at the electrode/electrolyte interface [259].

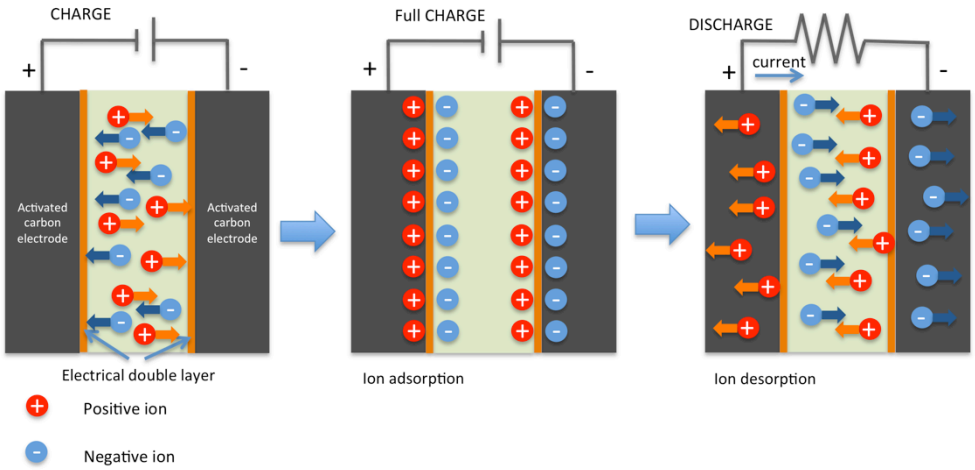

Figure 50: Charge and Discharge of an EDLC (from [259]).

Positive and negative ions are accumulated at this interface, typically in the order of 5-10 Å [266]. The conventional formula that defines the capacitance is:

$$C = \varepsilon_0 \varepsilon_r \frac{A}{d} \qquad (8)$$

where ε_0 is the permittivity of the vacuum, ε_r is the permittivity of the electrolyte and d is the thickness of the double layer with surface area A. The thickness (d) of the interface is very small (order of Å), as discussed previously, while the surface area (A) of the electrode is usually very high owing to the porous structures with a large internal surface area, which are usually chosen for supercapacitor applications. In this way, the capacitance can reach a high value (>10 $\mu F/cm^2$).

The model described to store the charges at the interface electrode/electrolyte was designed for the first time by Helmholtz [267] in the 19th century. But only in around 1910 Gouy [268] and Chapman [269] were able to expand the model considering the thermal motion of the electrolyte ions that leads to a diffuse layer. Stern [270], in 1924, combined the two theories in order to identify an inner plane, inner Helmholtz plane (IHP), and an outer plane, outer Helmholtz plane (OHP). The ions of the IHP are strongly bonded to the IHP resulting in a strong electric field in that area (Figure 51) [271]. The capacitance established at one electrode will be given by the sum of a compact double layer capacitance (C_H) and diffusion region capacitance (C_{diff}):

$$\frac{1}{C} = \frac{1}{C_H} + \frac{1}{C_{diff}} \qquad (9)$$

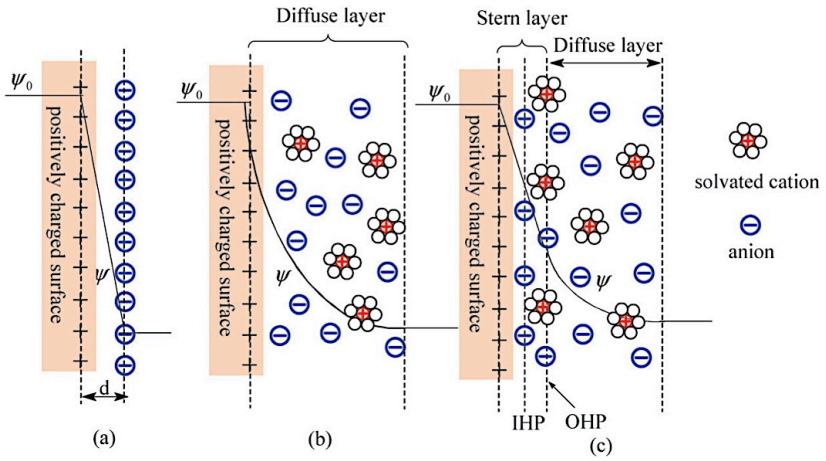

Figure 51: Models of the electrical double layer at a positively charged surface: (a) the Helmholtz model, (b) the Gouy-Chapman model, and (c) the Stern model, showing the inner Helmholtz plane (IHP) and outer Helmholtz plane (OHP). The IHP refers to the distance of closest approach of specifically adsorbed ions (generally anions) and OHP refers to that of the non-specifically adsorbed ions. The OHP is also the plane where the diffuse layer begins. d is the double layer distance described by the Helmholtz model. Ψ_0 and Ψ are the potentials at the electrode surface and the electrode/electrolyte interface, respectively (from [271]).

The ideal total capacitance in an EDLC is given by the sum of the capacitances established at the two electrode/electrolyte interfaces [272]:

$$\frac{1}{C} = \frac{1}{C_1} + \frac{1}{C_2} \qquad (10)$$

Unfortunately, other parameters have to be considered in a simple equivalent circuit of an EDLC such as the insulation resistances (R_1, R_2), the electrodes resistances (Re_1, Re_2) and the interelectrode resistance (R_S) [259] (Figure 52).

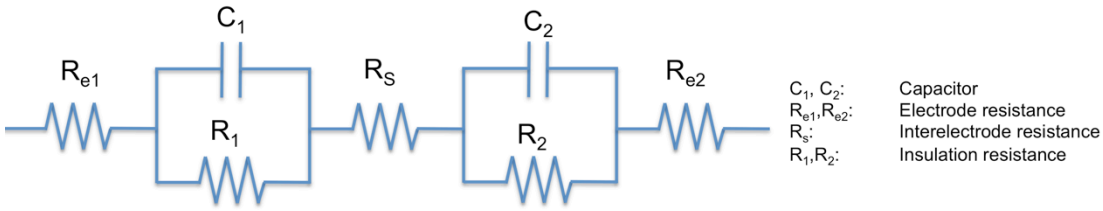

Figure 52: Simple equivalent circuit

In contrast, pseudo-capacitors are devices where the charge is not stored electrostatically but electrochemically similar to what happens in conventional lithium ion batteries. The materials that compose the electrode are subjected to a faradaic

oxidation/reduction reaction at specific potentials during charging and discharging processes involving absorption or intercalation with the electrolyte. Pseudocapacitive materials such as conducting polymer (e.g. polyanaline (PANI) [273]) or metal oxides (e.g. ruthenium oxide (RuO_2) [274]) can have 10-100 times larger capacitance than EDLCs but they suffer from poor stability, short lifetime and are expensive to synthesize. Because of these drawbacks, they are usually combined with carbon materials creating hybrid supercapacitors. The capacitance for a pseudocapacitor is calculated using the following formula [259]:

$$\frac{C}{Q} = \frac{\frac{F}{RT}\exp\left(\Delta E\frac{F}{RT}\right)}{\left[1+\exp\left(\Delta E\frac{F}{RT}\right)\right]^2} \qquad (11)$$

By using the Nernst equation that describes the general oxidation/reduction phenomenon. E represents the equilibrium potential for the reaction and $(E - E^0) = \Delta E$, F is the Faraday constant defined as the number of coulombs per mole of electrons and Q describes the charge related to the materials subjected to oxidation or reduction.

Pseudocapacitors are not explored in this work because of the drawbacks described previously and of the uncertainty on whether they should be categorized in the supercapacitor or in the battery family. In fact, their operating mechanism is more similar to a chemical battery than to a supercapacitor.

In order to characterize the electrical properties of a supercapacitor, three electrochemical measurement techniques are usually performed: cyclic voltammetry (CV), galvanostatic charging/discharging and electrochemical impedance.

The CV technique consists of applying a potential sweep rate dV/dt from a lower limit to an upper limit and vice-versa in order to measure the reversibility of the process and the stability of the device. The characteristic of the CV curve depends on the rate of the electron transfer reactions, the chemical reactivity of the electrode/electrolyte and the voltage scan rate [275]. The CV measurement is usually plot as Voltage (V) vs. Current (I) with an ideal supercapacitor presenting a rectangular CV curve when the capacitance (C) is constant across the different potential scan range (Figure 53). The capacitance (C) can be calculated by measuring the current (I) from the CV curves and knowing the potential sweep rate (dV/dt) applied from the formula:

$$I = C\left(\frac{dV}{dt}\right) \qquad (12)$$

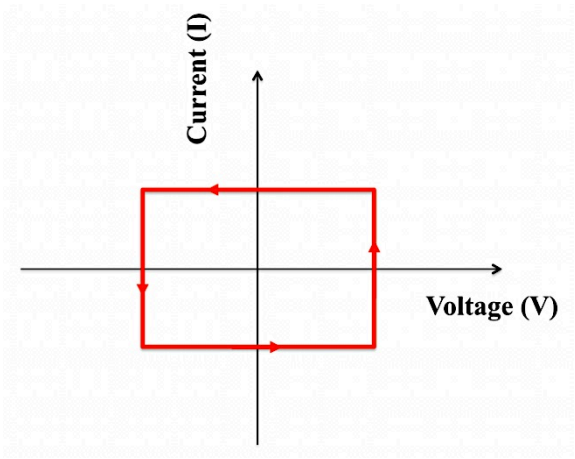

Figure 53: CV curve of an ideal supercapacitor

Most of the real CV curves for an EDLC show deviations from the ideal shape because of the electrolyte and electrode resistance and unwanted Faradaic reactions. For example, Figure 54 shows a simulation of CV curves with increasing internal resistance at a fixed scan rate [276].

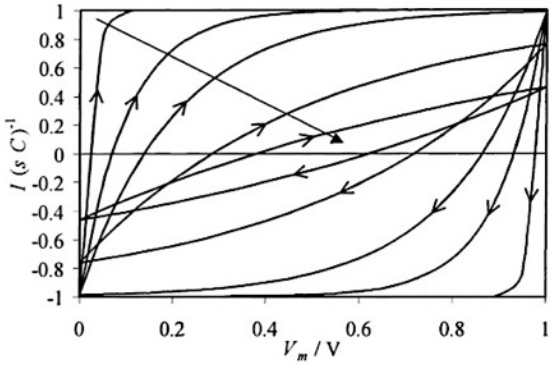

Figure 54: Simulation of CV curves with increasing internal resistance (1, 5, 10, 25 and 50 Ω) at 20mV/s scan rate with C= 1F and voltage range from 0 to 1V (from [276]).

The galvanostatic charge/discharge measurement is instead obtained by charging/discharging the supercapacitor at a certain defined current (I) within a certain voltage window. The galvanostatic charge/discharge measurement is plotted Time (s) vs. Voltage (V) (Figure 55). Capacitance and the internal resistance of the device can be extracted from this measurement technique. The capacitance is calculated from the slope of the charge or discharge curve with the formula [259]:

$$C = I/(-\Delta V/\Delta t) \qquad (13)$$

The effective series resistance (R_{ESR}) is calculated from the voltage drop (V_{drop}) that occurs at the initial portion of the discharge with the formula [259]:

$$R_{ESR} = V_{drop}/2I \qquad (14)$$

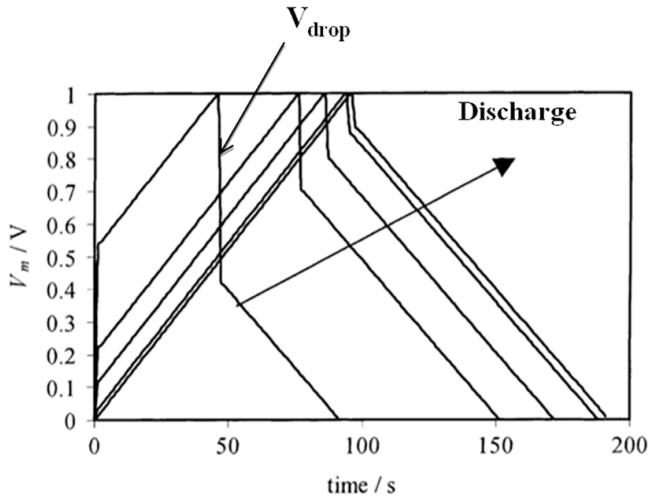

Figure 55: Simulation of the charge/discharge curves with increasing internal resistance (0, 1, 5, 10 and 25 Ω) at I = 10 mA. The smallest V_{drop} can be achieved with the smallest internal resistance. The largest total time of charging is also achieved with the smallest internal resistance (from [276]).

It can be noticed in Figure 55 that the total time of charging to a specific voltage limit decreases with increasing the internal resistance. This occurs because the electrode has a smaller effective charge capacity within a specific voltage window [276].

Another useful measurement technique to reveal the properties of a supercapacitor is the Electrochemical Impedance Spectroscopy (EIS) that measures the impedance (Z) of a device over a range of frequencies. The data obtained are usually graphed as the real part of the impedance (Z_{real}) vs. the imaginary part of the impedance (Z_{imag}), also called the Nyquist plot. Figure 56 shows the Nyquist plot of an ideal and a simplified supercapacitor. The ideal capacitor exhibits just a vertical line while a real one usually starts with a 45° line and then approaches a vertical line at higher frequencies. The 45° region, also called the Warburg region, is governed by the distributed resistance/capacitance in a porous electrode and by the electrolyte conductivity [259]. The effective series resistance (R_{ESR}) and the equivalent distributed resistance (R_{EDR}) can also be extracted from the Nyquist plot as shown in Figure 56 [272].

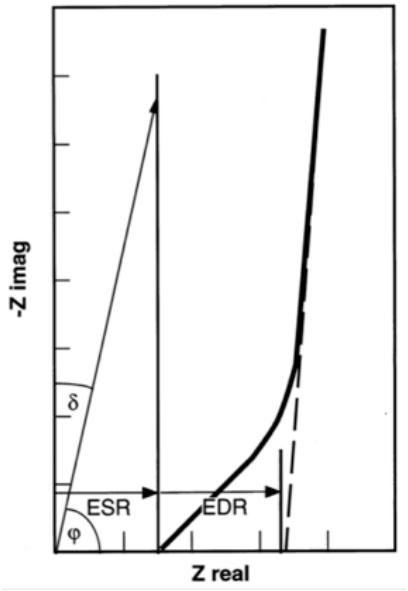

Figure 56: Schematic representation of the Nyquist impedance plot of an ideal capacitor (vertical thin line) and a supercapacitor with porous electrodes (thick line) (from [272]).

To determine the supercapacitor performance another two important factors, apart from the capacitance, need to be considered. One is the energy density that corresponds to the amount of energy stored per unit volume or mass and the other one is the power density that combines energy density with the speed that energy can be drawn out of a device.

The energy density per unit volume, expressed in Wh/cm^3, is defined by the formula [259]:

$$E = \frac{1}{2} C_{stack} \frac{(\Delta V)^2}{3600} \qquad (15)$$

where $C_{stack} = C/V$ is the volumetric stack capacitance expressed in F/cm^3 and ΔV is the operating voltage window of the device.

The power density per unit volume, expressed in W/cm^3 is defined by the formula [259]:

$$P = \frac{(\Delta V)^2}{4 R_{ESR} A d} \qquad (16)$$

Where A is the area of the electrodes, d is the distance between the electrodes, ΔV is the operating voltage window of the device and R_{ESR} is the total effective resistance of the device that can be extracted from the galvanostatic charge/discharge curves.

The maximum energy and power densities are achieved at the maximum voltage applied to the device which is usually determined by the maximum voltage that the electrolyte can tolerate before decomposition and breakdown of the electrode material.

Using formula (15), the easiest way to increase the energy density is to increase the capacitance (C) of the device but it is not the only way. The energy density can also be improved by increasing the voltage window of the electrolyte (ΔV), which follows a quadratic law. Organic electrolytes can achieve higher voltages compared to aqueous electrolytes allowing a dramatic increase in energy density. Unfortunately, they also show an effective series resistance (R_{ESR}) of at least 20 times larger than the aqueous ones which reduces the power density (formula (16)) [272].

In summary, several important characteristics of an EDLC have to be considered to maximize the performance of the device [259]:

- The specific surface area of the electrodes to increase the capacitance
- The conductivity of the electrodes to reduce the power density losses
- The resistance to any oxidation/reduction on the surface of the electrode to maintain good stability and performance
- Controlled distribution size of the pores that should match the size of the electrolyte ions
- Electrochemical stability of the electrolyte in the voltage operating window of the device
- Low interconnected resistance of the electrolyte
- Good wettability of the electrolyte on the electrode

4.1 The use of carbon nanotubes and graphene in supercapacitors

Activated carbons (ACs) are the most commonly used materials for commercial electrodes in supercapacitors because of their stable electrical properties, large surface area and low cost. ACs can be produced by thermal and/or chemical activation of various types of materials containing carbon such as wood, coal etc. For thermal activation, high temperatures are usually employed (from 700 °C to 1200 °C) in the presence of oxidising gases. For chemical activation the temperatures are lower (from 400 °C to 700 °C) and require activating agents such as phosphoric acid, sodium hydroxide and others [271]. These two processes allow the production of a material with a high surface area (3000 m^2/g) but with a wide pore size distribution consisting of macropores (> 50 nm), mesopores (2-50 nm) and micropores (< 2 nm) [277-278]. Even with such a high surface area, the experimental capacitance obtained with these materials is lower (<10 $\mu F/cm^2$) when compared to the theoretical calculations [266]. This difference indicates that not all of the pores are contributing to the charge storage mechanism and that the specific surface area is not the only parameter to be considered in a supercapacitor [279]. Pore shape and structure, pore size distribution, electrical conductivity and wettability of the electrode are other important parameters that contribute to the performance of the device as discussed previously. Pore size distribution in ACs is still a problem that has to be addressed [271].

Carbon nanomaterials like CNTs and graphene are excellent candidates to replace ACs as electrode materials in supercapacitors because of their large specific surface area, remarkable chemical stability, and high electric conductivity[280-281]. Commercial supercapacitors contain metal foils as current collectors such as Al, Cu, and stainless steel, whicht require special techniques to passivate the metal surface to avoid corrosion effects due to the use of alkali or acidic electrolyte [282]. Because of the high conductivity of CNTs and graphene, they can function as the capacitor electrode and the current collector leading to a more simple and lightweight device.

CNTs in forms of either arrays grown on a substrate [283-284] or network films processed from a suspension [285] have been employed in supercapacitors by using. CNTs show a specific capacitance of 15-200 F/g [286] with a high power capability but a low energy density due to a small specific surface area (<500 m^2g^{-1}) caused by the entangled arrangement of the CNTs with only the outermost tubes of the bundles exposed to the electrolyte (Figure 57) [287].

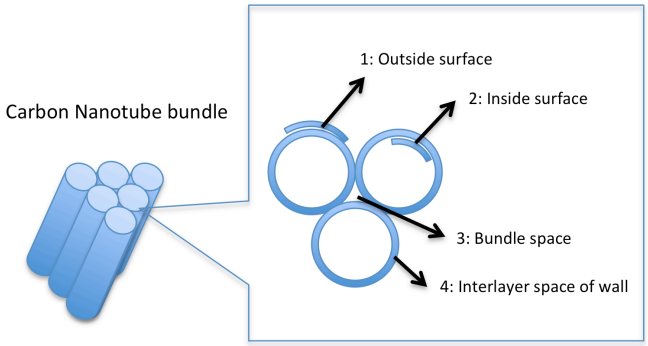

Figure 57: Schematic illustration of the spaces in a carbon nanotube bundle for the storage of electrolyte ions (from [287]).

CNTs grown on a substrate can be very useful for high power applications when compared to ACs. In fact, the schematic in Figure 58 shows that if the CNTs are all aligned on a current collector, the resistance can be low because the path for ions and electrons is much simpler than in the typical ACs electrode [287].

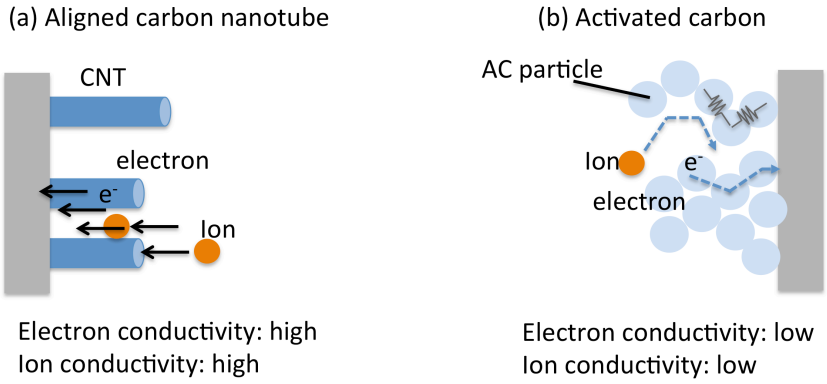

Figure 58: Comparison on conducting paths for electron and electrolyte ion in aligned carbon nanotubes and granular activated carbon (from [287]).

MWNTs were the first to be proposed as an electrode for an EDLC, showing a capacitance of ~100 F/g, a low surface area of ~400 m^2/g and a low power density value of 8 kW/kg [288]. However, apart from their high volumetric capacitance values [289] obtained by optimizing the growth process, SWNTs are preferred because they exhibit a higher surface area and consequently better overall performance [290].

Many strategies have been proposed to increase the surface area of SWNTs such as oxidizing methods, pyrolysis methods or by the use of liquids' zipping effects [285, 291-292]. The electrochemical oxidation in KOH can increase the capacitance by three times because it can facilitate the opening of some tubes which increases the surface area. A "super growth" method has also been beneficial to increase the surface area to 1000 m^2/g when compared to the 400-800 m^2/g for commercial CNTs, proving that this material can have better capacitive performance than ACs [292].

A combination of the "super growth" and oxidation methods has also been proposed in order to further increase the surface area to over 2000 m^2/g with an energy density and power density of 24.7 Wh/kg and 98.9 kW/kg, respectively [293].

Vertical SWNTs with high purity and high density have also been grown by CVD and then removed from the substrate as a single unit, uniformly densified and engineered into different shapes by the zipping effects of liquid. The surface tension of the liquids and the strong van der Waals interactions can zip the SWNTs together to near-ideal graphitic spacing. With this method, no insulating binders were needed with a conductivity 20 times larger than ACs and a higher capacitive performance than in the conventional SWNTs forest (Figure) [294].

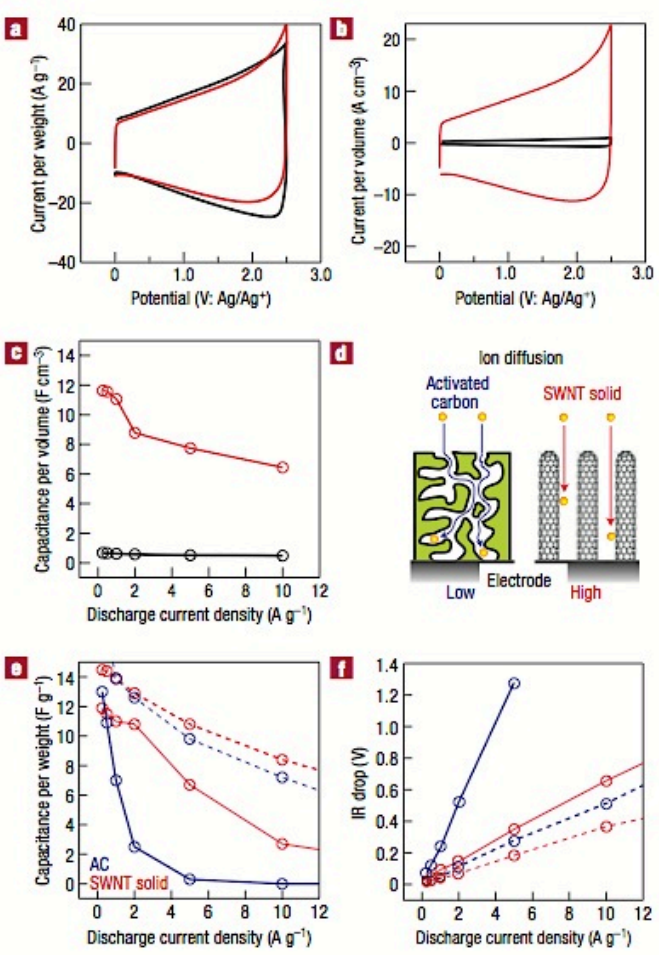

Figure 59: CV curves of the EDLC using the SWNT solid sheet (red) and as-grown forest (black) as electrodes comparing the capacitance per weight (a) and capacitance per volume (b). (c) Change in the capacitance per volume using the SWNT solid sheet (red) and as-grown forest (black). (d) Schematic model comparing the ion diffusion for activated carbon and the SWNT solid material. (e) Capacitance versus discharge current density comparing SWNT solid (red) and activated carbon (blue) for 0.1 and 0.5 mm electrode thicknesses (dashed and solid lines, respectively). (f) Potential drop associated with an increase in internal resistance (IR drop) for SWNT solid (red) and activated carbon (blue) for 0.1 and 0.5 mm electrode thicknesses (dashed and solid lines, respectively) (from [294]).

Another alternative, a mixture of CNTs and carbon aerogel, has been proposed to increase the surface area to 1059 m^2/g, obtaining a specific capacitance of 524 F/g (Figure) [295].

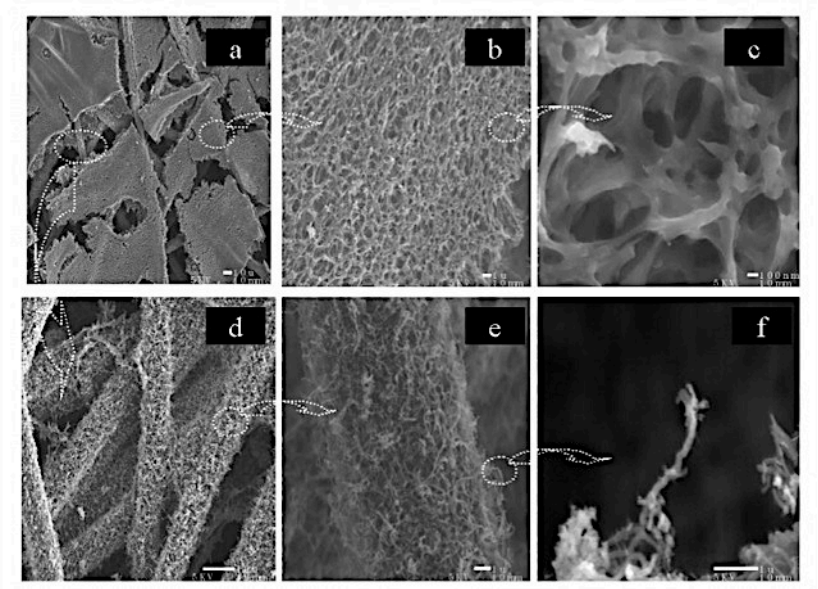

Figure 60: SEM images of CNTs- carbon aerogel nanocomposites (from [295]).

Recently, graphene and graphene derivatives have been considered for supercapacitor electrodes, not only for their exceptional electrical, thermal and mechanical properties described previously, but also for two other main reasons: the theoretical high surface area (2630 m^2/g) [69] and the inexpensive methods of production [82]. In fact, for supercapacitor applications, methods like the chemical exfoliation of graphite or the thermal reduction of GO are probably the most used because of the straight forward large quantity production of quality materials for electrodes. The addition of certain functional groups can also help to disperse the material in different solvents [296].

Stoller et al. [69] were the first group to explore the possibility of using chemically modified graphene, specifically reducing GO with hydrazine hydrate for EDLCs obtaining specific capacitance values of 135 F/g and 99 F/g for aqueous and organic electrolytes, respectively, even with a low surface area of 705 m^2/g (Figure).

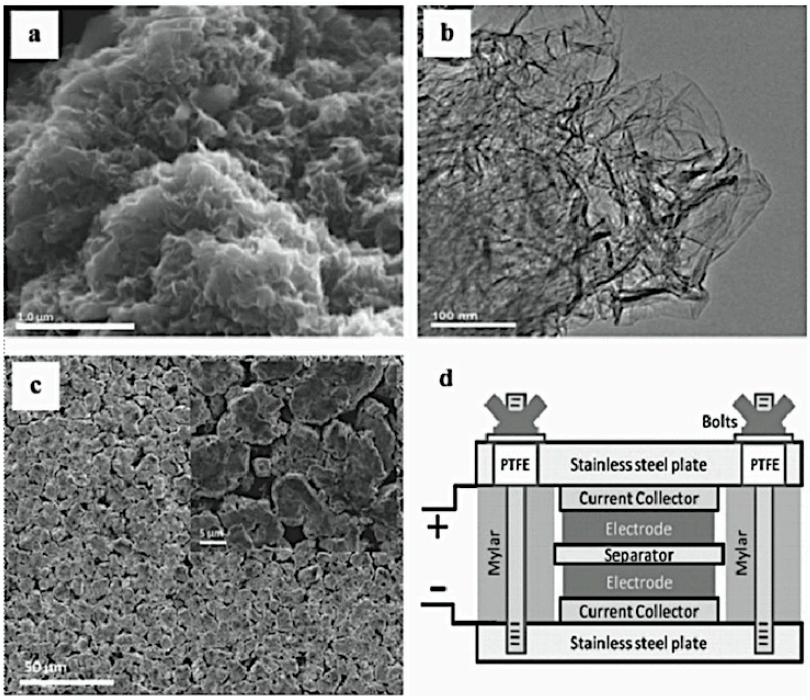

Figure 61: Graphene based EDLCs utilizing chemically modified graphene as electrode materials. (a) Scanning electron microscopy (SEM) image of the material. (b) Transmission electron microscopy (TEM) image showing individual graphene sheets. (c) Low- and high-(inset) magnification SEM images of the electrode. (d) Schematic of test cell assembly (from [69]).

In order to maximize the performance by increasing the surface area, Wang et al. [297] proposed to reduce the GO in a gas-solid reduction process (Figure). In this way, they were able to obtain a capacitance of 205 F/g with a power density and energy density of 10 kW/kg and 28.5 Wh/kg, respectively.

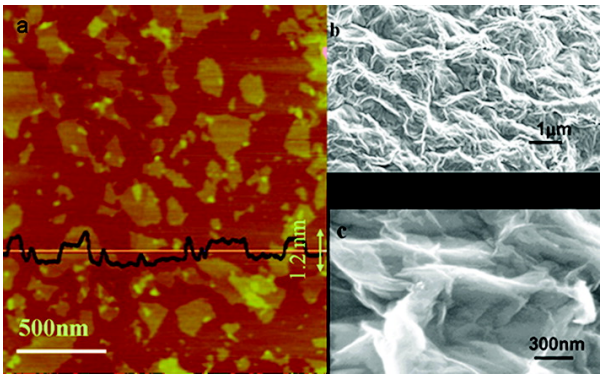

Figure 62: Morphology of graphene oxide and graphene-based materials. (a) Tapping-mode AFM image of graphene oxide and height profile plot. (b) and (c) SEM images at lower and

higher magnification respectively of the graphene oxide reduced by a gas-solid reduction process (from [297]).

Others, like Chen et al. [298], proposed to mildly reduce the GO with hydrobromic acid in order to maintain some oxygen-functional groups that could promote the wettability of the electrode and avoid restack of the graphene sheets allowing a better penetration of the electrolyte ions through the film. With this method, they were able to achieve a very high capacitance value of 348 F/g.

An exfoliation process of GO was also explored as a method to fabricate EDLCs electrodes. In particular, Lv et al. [299] showed that low temperature exfoliation of GO (200 °C) led to graphene based electrodes with 264 F/g and 122 F/g in aqueous and organic electrolytes, respectively.

Zhu et al. [124], instead, proposed a very inexpensive way to reduce the GO for EDLCs electrodes. They reduced the material in a conventional microwave oven obtaining a surface area of 463 m^2/g with a specific capacitance of 191 F/g [124]. Certainly, these are not the highest values reported but the ability to use a simple microwave creates a pathway for a scalable and inexpensive process to fabricate electrodes for supercapacitors.

A similar concept was proposed in 2012 by Kady et al. [300] using a standard LightScribe DVD optical drive to reduce GO and employing a gel electrolyte based on poly(vinyl alcohol) (PVA)-H_3PO_4 to fabricate flexible devices (Figure). The material showed a high surface area of 1520 m^2/g and a specific capacitance of 265 F/g.

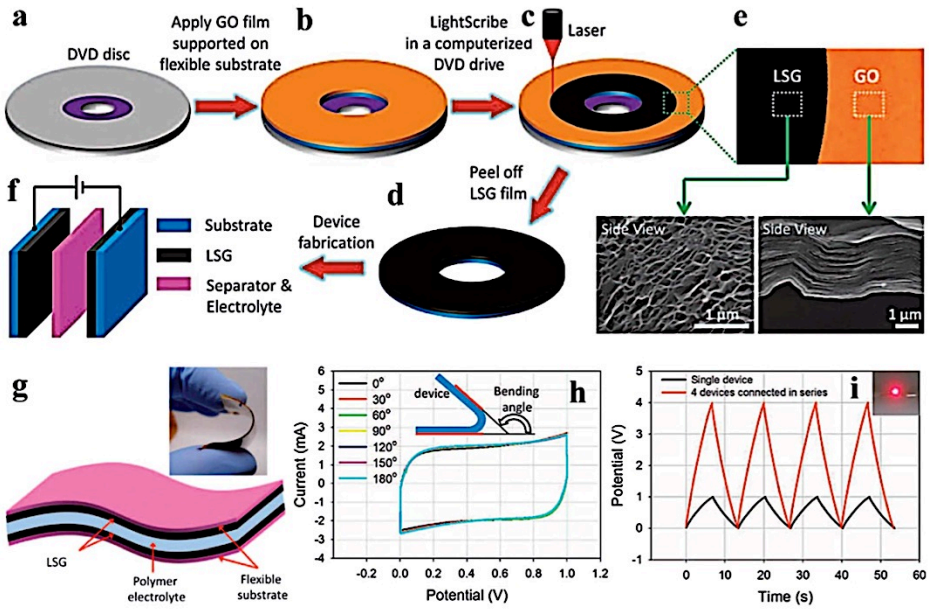

Figure 63: (a-d) Schematic illustration of the process to make laser-scribed graphene-based electrochemical capacitors. A GO film supported on a flexible substrate is placed on top of a LightScribe-enabled DVD media disc, and a computer image is then laser-irradiated on the GO film in a computerized LightScribe DVD drive. (e) As shown in the photograph, the GO film changes from golden brown color to black as it reduced to laser-scribed graphene. The low-power infrared laser changes the stacked GO sheets immediately into well-exfoliated few-layered laser scribed film, as shown in the cross-sectional SEM images. (f) A symmetric supercapacitor is constructed from two identical laser scribed electrodes, an ion-porous separator, and an electrolyte. (g) A schematic diagram of the all-solid-state device illustrates that the gelled electrolyte can serve as both the electrolyte and separator. The inset is a digital photograph showing the flexibility of the device. (h) CV curves collected at a scan rate of 1000 mV/s when the device was bent with different angles. (i) Galvanostatic charge-discharge curves for four devices connected in series. The inset image shows the glow of an LED light power by the four devices in series (from [300]).

In 2013, Kady et al. [301] were able to further develop this technique by fabricating more than 100 micro-supercapacitors on a single DVD disc in 30 minutes. The devices were built on flexible substrates to integrate them with MEMS or CMOS technologies into a single chip (Figure). These micro-supercapacitors demonstrated a very high power density of 200 W/cm^3.

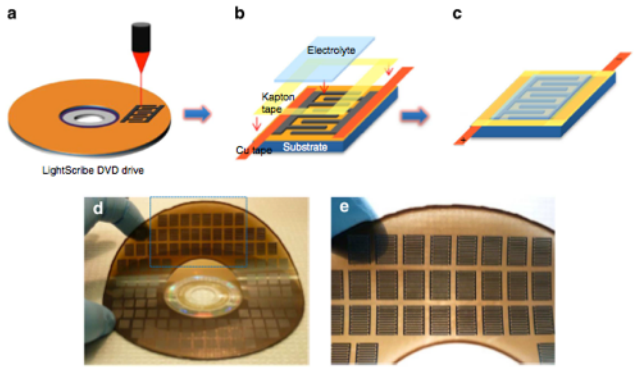

Figure 64: (a-c) Schematic diagram showing the fabrication process for a laser scribe graphene micro-supercapacitor. A GO film supported on a PET sheet is placed on a DVD media disc. The disc is inserted into a LightScribe DVD drive and a computer-designed circuit is etched onto the film. The laser inside the drive converts the golden-brown GO into black laser scribe graphene at precise locations to produce interdigitated graphene circuits (a). Copper tape is applied along the edges to improve the electrical contacts, and the interdigitated area is defined by polyimide (Kapton) tape (b). An electrolyte overcoat is then added to create a planar micro-supercapacitor (c). This technique has the potential for the direct writing of micro-devices with a high areal density (d,e). More than 100 micro-devices can be produced on a single run. The micro-devices are completely flexible and can be produced on virtually any substrate (from [301]).

Other graphene structures have been proposed to further boost the performance of EDLCs because planar structures have limited capacitance values due to the restacking of the graphene sheets which reduces the surface area. Porous 3D graphene networks have been synthetized by freezing and drying a chemically reduced GO dispersion [302-303] or by CVD on nickel foam [304-305] to overcome the limitations of planar structures.

Xu et al. [302] prepared a 3D porous reduced GO hydrogel with a capacitance of 186 F/g and a capacitance decay of only 8.4 % after 10,000 charge/discharge cycles in a PVA-H_3PO_4 gel polymer electrolyte (Figure). Even with such a high capacitance, the power density is limited to 0.5-5 kW/kg indicating that the porous structure has a large internal resistance and needs to be combined with an Au current collector. An electrode that also functions as a bendable high efficient current collector is usually preferred for supercapacitor applications in order to maintain a high power density value [306].

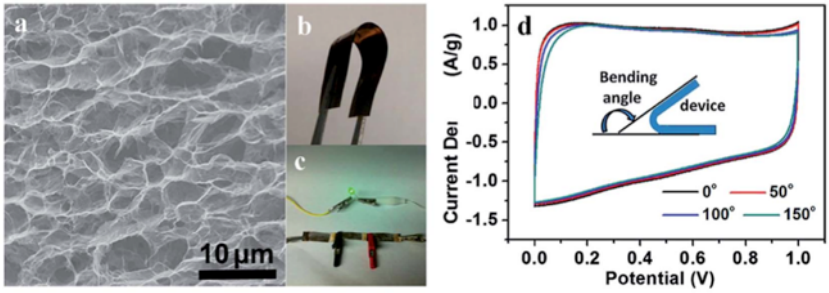

Figure 65: (a) SEM image of the interior microstructure of a graphene hydrogel. (b) Photograph of the flexible solid-state supercapacitor based on the graphene hydrogel film. (c) Photograph of a green LED powered by the three supercapacitors in series. (d) CV curves of the flexible solid-state device at 10 mV/s for different bending angles (from [302]).

Hybrid structures of CNTs and graphene electrodes have also been proposed for supercapacitors in order to combine the properties of both materials boosting the capacitance and the energy density of the devices [307-311]. In fact, the idea is to increase the surface area and have a defined architecture for the electric transport by using graphene to store the charges and CNTs as an efficient charge transport. Jha et al. [309] demonstrated that a device made of reduced GO mixed in a proportion of 1:1 with SWNTs achieved a specific capacitance of 222 F/g and with an energy density of 94 Wh/kg in an ionic liquid electrolyte (Figure).

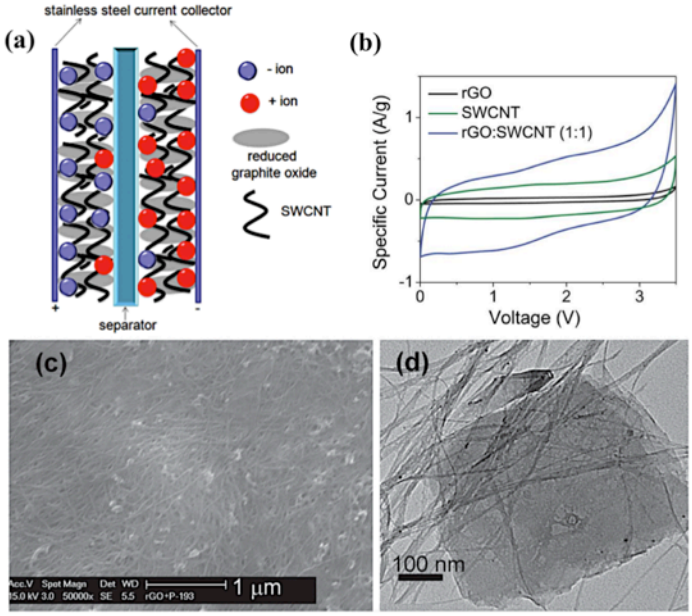

Figure 66: (a) Schematic illustration of a supercapacitor cell fabricated from reduced graphite oxide (rGO) and single-walled carbon nanotubes (SWCNTs). (b) CV curves of the

materials at 10 mV/s. (c) SEM images of the hybrid material consisting of rGO and SWNTs in a 1:1 weight ratio. (d) TEM image of the hybrid material showing few-layer graphene sheets covering a network of SWNTs (from [309]).

Flexible supercapacitors have been integrated into organic solar cells in order to eliminate the energy loss in the wiring between the energy conversion device and the storage device. Wee et al. [312] demonstrated that it is possible to integrate both devices in one printable all-solid device. The supercapacitor was charged by a polymer solar cell and the discharge was achieved by connecting it to a resistor (Figure). The capacitance obtained from the discharge was only 28 F/g but the possibility to combine both devices onto a flexible and printable surface opens up the avenue to a scalable and cheap process to have a generation and storage device simultaneously.

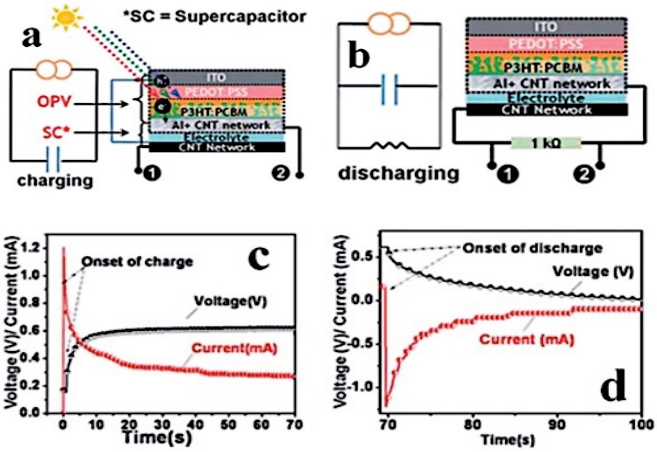

Figure 67: (a) and (b) Schematic and equivalent circuit illustration for a polymer solar cell and a supercapacitor during charging and discharging, respectively. The voltage and current profiles versus time for the charging (c) and discharging (d) process (from [312]).

5 Conclusions

The energy demand is increasing rapidly due to dramatic population growth and technological advances worldwide. Conventional energy sources are limited and are polluting the environment. Photovoltaics represent a viable solution to produce clean energy but their costs are still high due to materials and process techniques involved.
Moreover, an efficient energy storage system is required to make it independent from the grid, because the sun is an intermittent energy source. Carbon, one of the most abundant materials found on earth, can be a valid material for both energy generation and storage, as it can be employed in real world devices like organic solar cells and supercapacitors in one or more of its allotrope forms (Graphene, Carbon Nanotubes, Fullerene), with inexpensive synthesis and process methods based on printing and roll-to-roll techniques.
In this paper, different approaches to synthesize and use carbon nanomaterials for energy generation and storage applications have been explored.
Carbon nanomaterials have been reviewed for organic solar cells. Graphene produced by electrochemical exfoliation could be a viable solution to produce a large quantity of transparent electrodes for organic solar cell. Achieving high quality material at a large scale still remains an issue in order to compete with conventional conducting transparent electrodes such as ITO. However, its potential of being used on flexible substrates, makes it very appealing for the organic solar cell field where roll-to roll techniques have been recently employed to increase the production volume.
Also, fullerene derivatives, CNTs and graphene oxide could help to boost the performance of organic solar cell devices if employed in the active or buffer layers. In fact, their semiconducting properties can be tuned by doping them with other materials or by changing their physical structure in order to absorb a broader range of solar spectrum wavelengths.
Carbon nanomaterials, in particular graphene, have also been proven to be very efficient and reliable materials for energy storage. The high specific surface area and conductivity of graphene are two key features for employing this material in supercapacitors. The ability to use a solid-state electrolyte composed of graphene oxide or a gel polymer electrolyte can lead to printable flexible devices that do not require any encapsulation. Even if carbon nanotubes present a low specific surface area, they can still be employed in combination with graphene to increase the conductivity of the electrode or the surface

roughness of the film to increase the number of ions stored at the interface electrode/electrolyte.

Carbon is still surprising researchers for its properties. Completely new carbon structures have been synthesized over the last 20 years, from 0D fullerenes to 1D nanotubes and 2D graphene, amazing the scientific community. The low cost of this element, the sixth most abundant on earth, makes it as an attractive choice to replace conventional materials for energy generation and storage applications.

6 Acknowledgements

The authors acknowledge the financial support of the Australian Research Council through the Discovery Projects DP130102120 and of the AOARD through the grant FA2386-14-1-4014. We also acknowledge the Marie Curie International Research Staff Exchange Scheme Fellowship within the 7th European Community Framework Programme. We thank the technical support of Dr. P. Hines, Dr. A Chou, Dr. H. Diao and Dr L. Rintoul from the Central Analytical Research Facility of the Institute of Future environments at QUT.

This work was performed in part at the Queensland node of the Australian National Fabrication Facility (ANFF) – a company established under the National Collaborative Research Infrastructure Strategy to provide nano and microfabrication facilities for Australia's researchers.

7 References

1. Gilbert, G., *World population: a reference handbook*. ABC-CLIO: 2005.
2. agency, I. E. World Outlook Energy 2015. https://www.iea.org/Textbase/npsum/WEO2015SUM.pdf.
3. Service, R. F., Is It Time to Shoot for the Sun? *Science* **2005,** *309* (5734), 548-551.
4. Armaroli, N.; Balzani, V., *Energy for a sustainable world: from the oil age to a sun-powered future*. Wiley-VCH: Weinheim, 2011.
5. Smalley, R. E., Future Global Energy Prosperity: The Terawatt Challenge. *MRS Bulletin* **2005,** *30* (06), 412-417.
6. Smil, V., *Energy at the crossroads: global perspectives and uncertainties*. MIT Press: Cambridge, Mass, 2003.
7. Mearns, E. Global Energy Trends – BP Statistical Review 2014.
8. Holgate, S. T., *Air pollution and health*. Academic Press: San Diego, 1999.
9. Letcher, T., *Climate Change: Observed impacts on Planet Earth*. Elsevier: 2009.
10. Simmons, M. R., Twilight In the Desert - Doubting Saudi Potential. *Petroleum Intelligence Weekly* **2005**, 1.
11. Hoffert, M. I.; Calderia, K.; Jain, A. K.; Haites, E. F.; et al., Energy implications of future stabilization of atmospheric CO2 content. *Nature* **1998,** *395* (6705), 881-884.
12. Lewis, N. S., Powering the Planet. *MRS Bulletin* **2007,** *32* (10), 808-820.
13. Armaroli, N.; Balzani, V., The Future of Energy Supply: Challenges and Opportunities. *Angewandte Chemie International Edition* **2007,** *46* (1-2), 52-66.
14. Titman, S. What's the Value of Saudi Aramco?
15. Ginley, D.; Green, M. A.; Collins, R., Solar Energy Conversion Toward 1 Terawatt. *MRS Bulletin* **2008,** *33* (04), 355-364.
16. Zhu, H.; Wei, J.; Wang, K.; Wu, D., Applications of carbon materials in photovoltaic solar cells. *Solar Energy Materials and Solar Cells* **2009,** *93* (9), 1461-1470.
17. Frackowiak, E., Carbon materials for supercapacitor application. *Physical chemistry chemical physics : PCCP* **2007,** *9* (15), 1774.
18. W, J., The Elements, Their Origin, Abundance and Distribution. Elsevier B.V: 1990; Vol. 240, pp 339-339.
19. Mauter, M. S.; Elimelech, M., Environmental Applications of Carbon-Based Nanomaterials. *Environmental Science & Technology* **2008,** *42* (16), 5843-5859.
20. Osawa, E., *Kagaku (Kyoto)* **1970,** *25*, 854-863.
21. D. A. Bochvar, E. G. G. p., *Dok. Akad. Nauk SSSR 209*, 610-615.
22. Kroto, H. W.; Heath, J. R.; O'Brien, S. C.; Curl, R. F.; Smalley, R. E., C60: Buckminsterfullerene. *Nature* **1985,** *318* (6042), 162-163.
23. Fuller, R. Buckminster. Encyclopædia Britannica Inc: 2013.
24. Taylor, R.; Hare, J. P.; Abdul-Sada, A. a. K.; Kroto, H. W., Isolation, separation and characterisation of the fullerenes C60 and C70: the third form of carbon. *Journal of the Chemical Society, Chemical Communications* **1990**, 10.1039/C39900001423 (20), 1423-1425.
25. Dresselhaus, M. S.; Dresselhaus, G.; Eklund, P. C., Fullerenes. *Journal of Materials Research* **1993,** *8* (8), 2054-2097.
26. Hirsch, A.; Brettreich, M., *Fullerenes*. Wiley-VCH: 2006.
27. Kratschmer, W.; Lamb, L. D.; Fostiropoulos, K.; Huffman, D. R., Solid C60: a new form of carbon. *Nature* **1990,** *347* (6291), 354-358.
28. Hare, J. P.; Kroto, H. W.; Taylor, R., Preparation and UV / visible spectra of fullerenes C60 and C70. *Chemical Physics Letters* **1991,** *177* (4–5), 394-398.
29. N. Bezmelnitsin, V.; V. Eletskii, A.; G. Schepetov, N.; G. Avent, A.; Taylor, R., Isolation and characterisation of C70O. *Journal of the Chemical Society, Perkin Transactions 2* **1997**, 10.1039/A607847H (4), 683-686.

30. Howard, J. B.; McKinnon, J. T.; Makarovsky, Y.; Lafleur, A. L.; Johnson, M. E., Fullerenes C60 and C70 in flames. *Nature* **1991,** *352* (6331), 139-141.
31. Hebgen, P.; Goel, A.; Howard, J. B.; Rainey, L. C.; Vander Sande, J. B., Synthesis of fullerenes and fullerenic nanostructures in a low-pressure benzene/oxygen diffusion flame. *Proceedings of the Combustion Institute* **2000,** *28* (1), 1397-1404.
32. Scott, L. T.; Boorum, M. M.; McMahon, B. J.; Hagen, S.; Mack, J.; Blank, J.; Wegner, H.; de Meijere, A., A Rational Chemical Synthesis of C60. *Science* **2002,** *295* (5559), 1500-1503.
33. Lee, H. M.; Olmstead, M. M.; Suetsuna, T.; Shimotani, H.; Dragoe, N.; Cross, R. J.; Kitazawa, K.; Balch, A. L., Crystallographic characterization of Kr@C60 in (0.09Kr@C60/0.91C60)[middle dot]{NiII(OEP)}[middle dot]2C6H6. *Chemical Communications* **2002**, 10.1039/B202925C (13), 1352-1353.
34. Saunders, M.; Jimenez-Vazquez, H. A.; Cross, R. J.; Mroczkowski, S.; Gross, M. L.; Giblin, D. E.; Poreda, R. J., Incorporation of helium, neon, argon, krypton, and xenon into fullerenes using high pressure. *Journal of the American Chemical Society* **1994,** *116* (5), 2193-2194.
35. Hummelen, J. C.; Knight, B. W.; LePeq, F.; Wudl, F.; Yao, J.; Wilkins, C. L., Preparation and characterization of fulleroid and methanofullerene derivatives. *The Journal of Organic Chemistry* **1995,** *60* (3), 532-538.
36. Gonzalez, R.; Hummelen, J. C.; Wudl, F., The Specific Acid-Catalyzed and Photochemical Isomerization of a Robust Fulleroid to a Methanofullerene. *The Journal of Organic Chemistry* **1995,** *60* (8), 2618-2620.
37. Iijima, S., Helical microtubules of graphitic carbon. *Nature* **1991,** *354* (6348), 56-58.
38. Walters, D. A.; Ericson, L. M.; Casavant, M. J.; Liu, J.; Colbert, D. T.; Smith, K. A.; Smalley, R. E., Elastic strain of freely suspended single-wall carbon nanotube ropes. *Applied Physics Letters* **1999,** *74* (25), 3803-3805.
39. Yu, M. F.; Files, B. S.; Arepalli, S.; Ruoff, R. S., Tensile loading of ropes of single wall carbon nanotubes and their mechanical properties. *Physical Review Letters* **2000,** *84* (24), 5552-5555.
40. Gao, G.; Çağin, T.; Goddard Iii, W. A., Energetics, structure, mechanical and vibrational properties of single-walled carbon nanotubes. *Nanotechnology* **1998,** *9* (3), 184-191.
41. Tans, S. J.; Devoret, M. H.; Dai, H.; Thess, A.; Smalley, R. E.; Geerligs, L. J.; Dekker, C., Individual single-wall carbon nanotubes as quantum wires. *Nature* **1997,** *386* (6624), 474-477.
42. Hone, J.; Whitney, M.; Piskoti, C.; Zettl, A., Thermal conductivity of single-walled carbon nanotubes. *Physical Review B - Condensed Matter and Materials Physics* **1999,** *59* (4), R2514-R2516.
43. Ajayan, P. M., Nanotubes from Carbon. *Chemical Reviews* **1999,** *99* (7), 1787-1800.
44. Vidu, R.; Rahman, M.; Mahmoudi, M.; Enachescu, M.; Poteca, T. D.; Opris, I., Nanostructures: a platform for brain repair and augmentation. *Frontiers in systems neuroscience* **2014,** *8*, 91.
45. Dresselhaus, M. S.; Dresselhaus, G.; Saito, R., Physics of carbon nanotubes. *Carbon* **1995,** *33* (7), 883-891.
46. Wang, X.; Li, Q.; Xie, J.; Jin, Z.; Wang, J.; Li, Y.; Jiang, K.; Fan, S., Fabrication of Ultralong and Electrically Uniform Single-Walled Carbon Nanotubes on Clean Substrates. *Nano Letters* **2009,** *9* (9), 3137-3141.
47. Yellampalli, S., *Carbon Nanotubes - Synthesis, Characterization, Applications*. InTech: 2011.
48. Baddour, C. E.; Briens, C., Carbon nanotube synthesis: A review. *International Journal of Chemical Reactor Engineering* **2005,** *3*.
49. Bolshakov, A. P.; Uglov, S. A.; Saveliev, A. V.; Konov, V. I.; Gorbunov, A. A.; Pompe, W.; Graff, A., A novel CW laser-powder method of carbon single-wall nanotubes production. *Diamond and Related Materials* **2002,** *11* (3-6), 927-930.

50. Eklund, P. C.; Pradhan, B. K.; Kim, U. J.; Xiong, Q.; Fischer, J. E.; Friedman, A. D.; Holloway, B. C.; Jordan, K.; Smith, M. W., Large-Scale Production of Single-Walled Carbon Nanotubes Using Ultrafast Pulses from a Free Electron Laser. *Nano Letters* **2002,** *2* (6), 561-566.
51. Guo, T.; Nikolaev, P.; Thess, A.; Colbert, D. T.; Smalley, R. E., Catalytic growth of single-walled manotubes by laser vaporization. *Chemical Physics Letters* **1995,** *243* (1-2), 49-54.
52. Arepalli, S., Laser ablation process for single-walled carbon nanotube production. *Journal of Nanoscience and Nanotechnology* **2004,** *4* (4), 317-325.
53. Jorio, A.; Dresselhaus, G.; Dresselhaus, M. S., *Carbon Nanotubes: Advanced Topics in the Synthesis, Structure, Properties and Applications*. Springer-Verlag: 2008.
54. Sinnott, S. B.; Andrews, R.; Qian, D.; Rao, A. M.; Mao, Z.; Dickey, E. C.; Derbyshire, F., Model of carbon nanotube growth through chemical vapor deposition. *Chemical Physics Letters* **1999,** *315* (1-2), 25-30.
55. Kumar, M.; Ando, Y., Chemical Vapor Deposition of Carbon Nanotubes: A Review on Growth Mechanism and Mass Production. *Journal of Nanoscience and Nanotechnology* **2010,** *10* (6), 3739-3758.
56. Sato, H.; Hata, K., Growth of carbon nanotubes by plasma-enhanced chemical vapor deposition. *New Diamond and Frontier Carbon Technology* **2006,** *16* (3), 163-176.
57. Alexandrescu, R.; Crunteanu, A.; Morjan, R. E.; Morjan, I.; Rohmund, F.; Falk, L. K. L.; Ledoux, G.; Huisken, F., Synthesis of carbon nanotubes by CO2-laser-assisted chemical vapour deposition. *Infrared Physics and Technology* **2003,** *44* (1), 43-50.
58. Smalley, R. E.; Yakobson, B. I., The future of the fullerenes. *Solid State Communications* **1998,** *107* (11), 597-606.
59. Nikolaev, P.; Bronikowski, M. J.; Bradley, R. K.; Rohmund, F.; Colbert, D. T.; Smith, K. A.; Smalley, R. E., Gas-phase catalytic growth of single-walled carbon nanotubes from carbon monoxide. *Chemical Physics Letters* **1999,** *313* (1-2), 91-97.
60. Geim, A. K.; Novoselov, K. S., The rise of graphene. *Nat Mater* **2007,** *6* (3), 183-191.
61. Seyller, T.; Bostwick, A.; Emtsev, K. V.; Horn, K.; Ley, L.; McChesney, J. L.; Ohta, T.; Riley, J. D.; Rotenberg, E.; Speck, F., Epitaxial graphene: a new material. *physica status solidi (b)* **2008,** *245* (7), 1436-1446.
62. Geim, A. K.; Novoselov, K. S., The rise of graphene. *Nat. Mater.* **2007,** *6* (3), 183-191.
63. Mayorov, A. S.; Gorbachev, R. V.; Morozov, S. V.; Britnell, L.; Jalil, R.; Ponomarenko, L. A.; Blake, P.; Novoselov, K. S.; Watanabe, K.; Taniguchi, T.; Geim, A. K., Micrometer-Scale Ballistic Transport in Encapsulated Graphene at Room Temperature. *Nano Letters* **2011,** *11* (6), 2396-2399.
64. Morozov, S. V.; Novoselov, K. S.; Katsnelson, M. I.; Schedin, F.; Elias, D. C.; Jaszczak, J. A.; Geim, A. K., Giant Intrinsic Carrier Mobilities in Graphene and Its Bilayer. *Physical Review Letters* **2008,** *100* (1), 016602.
65. Lee, C.; Wei, X.; Kysar, J. W.; Hone, J., Measurement of the elastic properties and intrinsic strength of monolayer graphene. *Science (New York, N.Y.)* **2008,** *321* (5887), 385-388.
66. Liu, F.; Li, J., Ab initio calculation of ideal strength and phonon instability of graphene under tension. *Physical Review B* **2007,** *76* (6).
67. Balandin, A. A., Thermal Properties of Graphene, Carbon Nanotubes and Nanostructured Carbon Materials. **2011**.
68. Nair, R. R.; Blake, P.; Grigorenko, A. N.; Novoselov, K. S.; Booth, T. J.; Stauber, T.; Peres, N. M. R.; Geim, A. K., Fine Structure Constant Defines Visual Transparency of Graphene. *Science* **2008,** *320* (5881), 1308-1308.
69. Stoller, M. D.; Park, S.; Yanwu, Z.; An, J.; Ruoff, R. S., Graphene-Based ultracapacitors. *Nano Letters* **2008,** *8* (10), 3498-3502.
70. Bunch, J. S.; Verbridge, S. S.; Alden, J. S.; van der Zande, A. M.; Parpia, J. M.; Craighead, H. G.; McEuen, P. L., Impermeable atomic membranes from graphene sheets. *Nano letters* **2008,** *8* (8), 2458-2462.

71. Bachtold, A.; Barreiro, A.; Moser, J., Current-induced cleaning of graphene. *Applied Physics Letters* **2007,** *91* (16), 163513-163513-3.
72. Katsnelson, M. I.; Fal'ko, V. I.; Zeitler, U.; McCann, E.; Novoselov, K. S.; Geim, A. K.; Jiang, D.; Schedin, F.; Morozov, S. V., Unconventional quantum Hall effect and Berry's phase of 2 π in bilayer graphene. *Nature Physics* **2006,** *2* (3), 177-180.
73. Katsnelson, M. I.; Guinea, F.; Geim, A. K., Energy gaps and a zero-field quantum Hall effect in graphene by strain engineering. *Nature Physics* **2009,** *6* (1), 30-33.
74. Meric, I.; Han, M. Y.; Young, A. F.; Ozyilmaz, B.; Kim, P.; Shepard, K. L., Current saturation in zero-bandgap, top-gated graphene field-effect transistors. *Nature Nanotechnology* **2008,** *3* (11), 654-659.
75. Novoselov, K., Graphene: Mind the gap. *Nature Material* **2007,** *6* (10), 720-721.
76. Geim, A. K., Graphene: Status and Prospects. *Science* **2009,** *324* (5934), 1530-1534.
77. Wallace, P. R., The Band Theory of Graphite. *Physical Review* **1947,** *71* (9), 622.
78. Avouris, P.; Dimitrakopoulos, C., Graphene: synthesis and applications. *Materials Today* **2012,** *15* (3), 86.
79. Novoselov, K. S.; Jiang, D.; Schedin, F.; Booth, T. J.; Khotkevich, V. V.; Morozov, S. V.; Geim, A. K., Two-dimensional atomic crystals. *Proceedings of the National Academy of Sciences of the United States of America* **2005,** *102* (30), 10451-10453.
80. Geim, A. K., Random walk to graphene. *Uspekhi Fizicheskih Nauk* **2011,** *181* (12), 1284.
81. Novoselov, K. S., Nobel Lecture: Graphene: Materials in the Flatland. *Reviews of Modern Physics* **2011,** *83* (3), 837.
82. Novoselov, K. S.; Falko, V. I.; Colombo, L.; Gellert, P. R.; Schwab, M. G.; Kim, K., A roadmap for graphene. *Nature* **2012,** *490* (7419), 192-200.
83. Bae, S.; Kim, H.; Lee, Y.; Xu, X.; Park, J.-S.; Zheng, Y.; Balakrishnan, J.; Lei, T.; Ri Kim, H.; Song, Y. I.; Kim, Y.-J.; Kim, K. S.; Ozyilmaz, B.; Ahn, J.-H.; Hong, B. H.; Iijima, S., Roll-to-roll production of 30-inch graphene films for transparent electrodes. *Nat Nano* **2010,** *5* (8), 574-578.
84. Li, X.; Cai, W.; An, J.; Kim, S.; Nah, J.; Yang, D.; Piner, R.; Velamakanni, A.; Jung, I.; Tutuc, E.; Banerjee, S. K.; Colombo, L.; Ruoff, R. S., Large-Area Synthesis of High-Quality and Uniform Graphene Films on Copper Foils. *Science* **2009,** *324* (5932), 1312-1314.
85. Stankovich, S.; Dikin, D. A.; Piner, R. D.; Kohlhaas, K. A.; Kleinhammes, A.; Jia, Y.; Wu, Y.; Nguyen, S. T.; Ruoff, R. S., Synthesis of graphene-based nanosheets via chemical reduction of exfoliated graphite oxide. *Carbon* **2007,** *45* (7), 1558-1565.
86. Eda, G.; Fanchini, G.; Chhowalla, M., Large-area ultrathin films of reduced graphene oxide as a transparent and flexible electronic material. *Nature Nanotechnology* **2008,** *3* (5), 270-274.
87. Novoselov, K. S.; Geim, A. K.; Morozov, S. V.; Jiang, D.; Zhang, Y.; Dubonos, S. V.; Grigorieva, I. V.; Firsov, A. A., Electric field in atomically thin carbon films. *Science* **2004,** *306* (5696), 666-669.
88. Allen, M. J.; Tung, V. C.; Kaner, R. B., Honeycomb carbon: A review of graphene. *Chemical Reviews* **2010,** *110* (1), 132-145.
89. Hernandez, Y.; Nicolosi, V.; Lotya, M.; Blighe, F. M.; Sun, Z.; De, S.; McGovern, I. T.; Holland, B.; Byrne, M.; Gun'Ko, Y. K.; Boland, J. J.; Niraj, P.; Duesberg, G.; Krishnamurthy, S.; Goodhue, R.; Hutchison, J.; Scardaci, V.; Ferrari, A. C.; Coleman, J. N., High-yield production of graphene by liquid-phase exfoliation of graphite. *Nature Nanotechnology* **2008,** *3* (9), 563-568.
90. Coleman, J. N., Liquid Exfoliation of Defect-Free Graphene. *Accounts of Chemical Research* **2012,** *46* (1), 14-22.
91. De, S.; King, P. J.; Lotya, M.; O'Neill, A.; Doherty, E. M.; Hernandez, Y.; Duesberg, G. S.; Coleman, J. N., Flexible, Transparent, Conducting Films of Randomly Stacked Graphene from Surfactant-Stabilized, Oxide-Free Graphene Dispersions. *Small* **2010,** *6* (3), 458-464.

92. Zhang, X.; Coleman, A. C.; Katsonis, N.; Browne, W. R.; van Wees, B. J.; Feringa, B. L., Dispersion of graphene in ethanol using a simple solvent exchange method. *Chemical Communications* **2010,** *46* (40), 7539-7541.
93. Du, W.; Jiang, X.; Zhu, L., From graphite to graphene: direct liquid-phase exfoliation of graphite to produce single- and few-layered pristine graphene. *Journal of Materials Chemistry A* **2013,** *1*, 10592-10606.
94. Nuvoli, D.; Valentini, L.; Alzari, V.; Scognamillo, S.; Bon, S. B.; Piccinini, M.; Illescas, J.; Mariani, A., High concentration few-layer graphene sheets obtained by liquid phase exfoliation of graphite in ionic liquid. *Journal of Materials Chemistry* **2011,** *21* (10), 3428-3431.
95. Behabtu, N.; Lomeda, J. R.; Green, M. J.; Higginbotham, A. L.; Sinitskii, A.; Kosynkin, D. V.; Tsentalovich, D.; Parra-Vasquez, A. N. G.; Schmidt, J.; Kesselman, E.; Cohen, Y.; Talmon, Y.; Tour, J. M.; Pasquali, M., Spontaneous high-concentration dispersions and liquid crystals of graphene. *Nature Nanotechnology* **2010,** *5* (6), 406-411.
96. Pupysheva, O. V.; Farajian, A. A.; Knick, C. R.; Zhamu, A.; Jang, B. Z., Modeling Direct Exfoliation of Nanoscale Graphene Platelets. *The Journal of Physical Chemistry C* **2010,** *114* (49), 21083-21087.
97. Su, C.-Y.; Lu, A.-Y.; Xu, Y.; Chen, F.-R.; Khlobystov, A. N.; Li, L.-J., High-Quality Thin Graphene Films from Fast Electrochemical Exfoliation. *ACS Nano* **2011,** *5* (3), 2332-2339.
98. Liu, J.; Notarianni, M.; Will, G.; Tiong, V. T.; Wang, H.; Motta, N., Electrochemically Exfoliated Graphene for Electrode Films: Effect of Graphene Flake Thickness on the Sheet Resistance and Capacitive Properties. *Langmuir* **2013,** *29* (43), 13307-13314.
99. Wassei, J. K.; Kaner, R. B., Graphene, a promising transparent conductor. *Materials Today* **2010,** *13* (3), 52-59.
100. Gao, W.; Alemany, L. B.; Ci, L.; Ajayan, P. M., New insights into the structure and reduction of graphite oxide. *Nature Chemistry* **2009,** *1* (5), 403-408.
101. Szabó, T.; Berkesi, O.; Forgó, P.; Josepovits, K.; Sanakis, Y.; Petridis, D.; Dékány, I., Evolution of surface functional groups in a series of progressively oxidized graphite oxides. *Chemistry of Materials* **2006,** *18* (11), 2740-2749.
102. Chen, D.; Feng, H.; Li, J., Graphene Oxide: Preparation, Functionalization, and Electrochemical Applications. *Chemical Reviews* **2012,** *112* (11), 6027-6053.
103. He, H.; Klinowski, J.; Forster, M.; Lerf, A., A new structural model for graphite oxide. *Chemical Physics Letters* **1998,** *287* (1), 53-56.
104. Becerril, H. A.; Mao, J.; Liu, Z.; Stoltenberg, R. M.; Bao, Z.; Chen, Y., Evaluation of Solution-Processed Reduced Graphene Oxide Films as Transparent Conductors. *ACS Nano* **2008,** *2* (3), 463-470.
105. Wang, S.; Chia, P. J.; Chua, L. L.; Zhao, L. H.; Png, R. Q.; Sivaramakrishnan, S.; Zhou, M.; Goh, R. G. S.; Friend, R. H.; Wee, A. T. S.; Ho, P. K. H., Band-like transport in surface-functionalized highly solution-processable graphene nanosheets. *Advanced Materials* **2008,** *20* (18), 3440-3446.
106. Brodie, B. C., On the Atomic Weight of Graphite. *Philosophical Transactions of the Royal Society of London* **1859,** *149* (ArticleType: research-article / Full publication date: 1859 /), 249-259.
107. Hummers, W. S.; Offeman, R. E., Preparation of Graphitic Oxide. *Journal of the American Chemical Society* **1958,** *80* (6), 1339-1339.
108. Marcano, D. C.; Kosynkin, D. V.; Berlin, J. M.; Sinitskii, A.; Sun, Z.; Slesarev, A.; Alemany, L. B.; Lu, W.; Tour, J. M., Improved Synthesis of Graphene Oxide. *ACS Nano* **2010,** *4* (8), 4806-4814.
109. Eda, G.; Chhowalla, M., Chemically derived graphene oxide: towards large-area thin-film electronics and optoelectronics. *Advanced materials* **2010,** *22* (22), 2392-2415.
110. Pei, S.; Cheng, H. M., The reduction of graphene oxide. *Carbon* **2012,** *50* (9), 3210-3228.

111. Lopez, V.; Sundaram, R. S.; Gomez-Navarro, C.; Olea, D.; Burghard, M.; Gomez-Herrero, J.; Zamora, F. l.; Kern, K., Chemical Vapor Deposition Repair of Graphene Oxide: A Route to Highly-Conductive Graphene Monolayers. *Advanced Materials* **2009,** *21*, 4683-4686.
112. Gómez-Navarro, C.; Meyer, J. C.; Sundaram, R. S.; Chuvilin, A.; Kurasch, S.; Burghard, M.; Kern, K.; Kaiser, U., Atomic Structure of Reduced Graphene Oxide. *Nano Letters* **2010,** *10* (4), 1144-1148.
113. Piloto, C.; Notarianni, M.; Shafiei, M.; Taran, E.; Galpaya, D.; Yan, C.; Motta, N., Highly NO2 sensitive caesium doped graphene oxide conductometric sensors. *Beilstein Journal of Nanotechnology* **2014,** *5*, 1073-1081.
114. Hontoria-Lucas, C.; López-Peinado, A. J.; López-González, J. d. D.; Rojas-Cervantes, M. L.; Martín-Aranda, R. M., Study of oxygen-containing groups in a series of graphite oxides: Physical and chemical characterization. *Carbon* **1995,** *33* (11), 1585-1592.
115. Jeong, H.-K.; Lee, Y. P.; Lahaye, R. J. W. E.; Park, M.-H.; An, K. H.; Kim, I. J.; Yang, C.-W.; Park, C. Y.; Ruoff, R. S.; Lee, Y. H., Evidence of Graphitic AB Stacking Order of Graphite Oxides. *Journal of the American Chemical Society* **2008,** *130* (4), 1362-1366.
116. Mattevi, C.; Eda, G.; Agnoli, S.; Miller, S.; Mkhoyan, K. A.; Celik, O.; Mastrogiovanni, D.; Granozzi, G.; Garfunkel, E.; Chhowalla, M., Evolution of Electrical, Chemical, and Structural Properties of Transparent and Conducting Chemically Derived Graphene Thin Films. *Advanced Functional Materials* **2009,** *19* (16), 2577-2583.
117. Ganguly, A.; Sharma, S.; Papakonstantinou, P.; Hamilton, J., Probing the Thermal Deoxygenation of Graphene Oxide Using High-Resolution In Situ X-ray-Based Spectroscopies. *The Journal of Physical Chemistry C* **2011,** *115* (34), 17009-17019.
118. Yang, D.; Velamakanni, A.; Bozoklu, G.; Park, S.; Stoller, M.; Piner, R. D.; Stankovich, S.; Jung, I.; Field, D. A.; Ventrice Jr, C. A.; Ruoff, R. S., Chemical analysis of graphene oxide films after heat and chemical treatments by X-ray photoelectron and Micro-Raman spectroscopy. *Carbon* **2009,** *47* (1), 145-152.
119. Schniepp, H. C.; Li, J.-L.; McAllister, M. J.; Sai, H.; Herrera-Alonso, M.; Adamson, D. H.; Prud'homme, R. K.; Car, R.; Saville, D. A.; Aksay, I. A., Functionalized Single Graphene Sheets Derived from Splitting Graphite Oxide. *The Journal of Physical Chemistry B* **2006,** *110* (17), 8535-8539.
120. Chambers, B. A.; Notarianni, M.; Liu, J.; Motta, N.; Andersson, G. G., Examining the electrical and chemical properties of reduced graphene oxide with varying annealing temperatures in argon atmosphere. *Applied Surface Science* **2015,** *356*, 719-725.
121. Wu, Z.-S.; Ren, W.; Gao, L.; Zhao, J.; Chen, Z.; Liu, B.; Tang, D.; Yu, B.; Jiang, C.; Cheng, H.-M., Synthesis of Graphene Sheets with High Electrical Conductivity and Good Thermal Stability by Hydrogen Arc Discharge Exfoliation. *ACS Nano* **2009,** *3* (2), 411-417.
122. Wu, Z.-S.; Ren, W.; Gao, L.; Liu, B.; Jiang, C.; Cheng, H.-M., Synthesis of high-quality graphene with a pre-determined number of layers. *Carbon* **2009,** *47* (2), 493-499.
123. Li, X.; Wang, H.; Robinson, J. T.; Sanchez, H.; Diankov, G.; Dai, H., Simultaneous nitrogen doping and reduction of graphene oxide. *Journal of the American Chemical Society* **2009,** *131* (43), 15939.
124. Zhu, Y.; Murali, S.; Stoller, M. D.; Velamakanni, A.; Piner, R. D.; Ruoff, R. S., Microwave assisted exfoliation and reduction of graphite oxide for ultracapacitors. *Carbon* **2010,** *48* (7), 2118-2122.
125. Zhang, Y.; Guo, L.; Wei, S.; He, Y.; Xia, H.; Chen, Q.; Sun, H.-B.; Xiao, F.-S., Direct imprinting of microcircuits on graphene oxides film by femtosecond laser reduction. *Nano Today* **2010,** *5* (1), 15-20.

126. Kotov, N. A.; Dékány, I.; Fendler, J. H., Ultrathin graphite oxide-polyelectrolyte composites prepared by self-assembly: Transition between conductive and non-conductive states. *Advanced Materials* **1996,** *8* (8), 637-641.
127. Stankovich, S.; Piner, R. D.; Chen, X.; Wu, N.; Nguyen, S. T.; Ruoff, R. S., Stable aqueous dispersions of graphitic nanoplatelets via the reduction of exfoliated graphite oxide in the presence of poly(sodium 4-styrenesulfonate). *Journal of Materials Chemistry* **2006,** *16* (2), 155-158.
128. He, Q.; Sudibya, H. G.; Yin, Z.; Wu, S.; Li, H.; Boey, F.; Huang, W.; Chen, P.; Zhang, H., Centimeter-Long and Large-Scale Micropatterns of Reduced Graphene Oxide Films: Fabrication and Sensing Applications. *ACS Nano* **2010,** *4* (6), 3201-3208.
129. Zhu, Y.; Cai, W.; Piner, R. D.; Velamakanni, A.; Ruoff, R. S., Transparent self-assembled films of reduced graphene oxide platelets. *Applied Physics Letters* **2009,** *95* (10).
130. Fernández-Merino, M. J.; Guardia, L.; Paredes, J. I.; Villar-Rodil, S.; Solís-Fernández, P.; Martínez-Alonso, A.; Tascón, J. M. D., Vitamin C is an ideal substitute for hydrazine in the reduction of graphene oxide suspensions. *Journal of Physical Chemistry C* **2010,** *114* (14), 6426-6432.
131. Periasamy, M.; Thirumalaikumar, M., Methods of enhancement of reactivity and selectivity of sodium borohydride for applications in organic synthesis. *Journal of Organometallic Chemistry* **2000,** *609* (1–2), 137-151.
132. Moon, I. K.; Lee, J.; Ruoff, R. S.; Lee, H., Reduced graphene oxide by chemical graphitization. *Nature Communications* **2010,** *1* (6), 1-6.
133. Williams, G.; Seger, B.; Kamat, P. V., TiO2-Graphene Nanocomposites. UV-Assisted Photocatalytic Reduction of Graphene Oxide. *ACS Nano* **2008,** *2* (7), 1487-1491.
134. Wang, Z.; Zhou, X.; Zhang, J.; Boey, F.; Zhang, H., Direct Electrochemical Reduction of Single-Layer Graphene Oxide and Subsequent Functionalization with Glucose Oxidase. *The Journal of Physical Chemistry C* **2009,** *113* (32), 14071-14075.
135. Dubin, S.; Gilje, S.; Wang, K.; Tung, V. C.; Cha, K.; Hall, A. S.; Farrar, J.; Varshneya, R.; Yang, Y.; Kaner, R. B., A One-Step, Solvothermal Reduction Method for Producing Reduced Graphene Oxide Dispersions in Organic Solvents. *ACS Nano* **2010,** *4* (7), 3845-3852.
136. Xu, Y.; Sheng, K.; Li, C.; Shi, G., Highly conductive chemically converted graphene prepared from mildly oxidized graphene oxide. *Journal of Materials Chemistry* **2011,** *21* (20), 7376-7380.
137. Yan, Z.; Peng, Z.; Tour, J. M., Chemical Vapor Deposition of Graphene Single Crystals. *Accounts of Chemical Research* **2014,** *47* (4), 1327-1337.
138. Grabke, H. J.; Paulitschke, W.; Tauber, G.; Viefhaus, H., Equilibrium surface segregation of dissolved nonmetal atoms on iron(100) faces. *Surface Science* **1977,** *63* (0), 377-389.
139. Shelton, J. C.; Patil, H. R.; Blakely, J. M., Equilibrium segregation of carbon to a nickel (111) surface: A surface phase transition. *Surface Science* **1974,** *43* (2), 493-520.
140. Hamilton, J. C.; Blakely, J. M., Carbon segregation to single crystal surfaces of Pt, Pd and Co. *Surface Science* **1980,** *91* (1), 199-217.
141. Hagstrom, S.; Lyon, H. B.; Somorjai, G. A., Surface Structures on the Clean Platinum (100) Surface. *Physical Review Letters* **1965,** *15* (11), 491-493.
142. May, J. W., Platinum surface LEED rings. *Surface Science* **1969,** *17* (1), 267-270.
143. Zhang, Y.; Gomez, L.; Ishikawa, F. N.; Madaria, A.; Ryu, K.; Wang, C.; Badmaev, A.; Zhou, C., Comparison of Graphene Growth on Single-Crystalline and Polycrystalline Ni by Chemical Vapor Deposition. *The Journal of Physical Chemistry Letters* **2010,** *1* (20), 3101-3107.
144. Chen, S.; Cai, W.; Piner, R. D.; Suk, J. W.; Wu, Y.; Ren, Y.; Kang, J.; Ruoff, R. S., Synthesis and Characterization of Large-Area Graphene and Graphite Films on Commercial Cu–Ni Alloy Foils. *Nano Letters* **2011,** *11* (9), 3519-3525.

145. Huang, P. Y.; Ruiz-Vargas, C. S.; van der Zande, A. M.; Whitney, W. S.; Levendorf, M. P.; Kevek, J. W.; Garg, S.; Alden, J. S.; Hustedt, C. J.; Zhu, Y.; Park, J.; McEuen, P. L.; Muller, D. A., Grains and grain boundaries in single-layer graphene atomic patchwork quilts. *Nature* **2011,** *469* (7330), 389-392.
146. Tsen, A. W.; Brown, L.; Levendorf, M. P.; Ghahari, F.; Huang, P. Y.; Havener, R. W.; Ruiz-Vargas, C. S.; Muller, D. A.; Kim, P.; Park, J., Tailoring Electrical Transport Across Grain Boundaries in Polycrystalline Graphene. *Science* **2012,** *336* (6085), 1143-1146.
147. Ruiz-Vargas, C. S.; Zhuang, H. L.; Huang, P. Y.; van der Zande, A. M.; Garg, S.; McEuen, P. L.; Muller, D. A.; Hennig, R. G.; Park, J., Softened Elastic Response and Unzipping in Chemical Vapor Deposition Graphene Membranes. *Nano Letters* **2011,** *11* (6), 2259-2263.
148. Yan, Z.; Lin, J.; Peng, Z.; Sun, Z.; Zhu, Y.; Li, L.; Xiang, C.; Samuel, E. L.; Kittrell, C.; Tour, J. M., Toward the Synthesis of Wafer-Scale Single-Crystal Graphene on Copper Foils. *ACS Nano* **2012,** *6* (10), 9110-9117.
149. Li, X.; Magnuson, C. W.; Venugopal, A.; Tromp, R. M.; Hannon, J. B.; Vogel, E. M.; Colombo, L.; Ruoff, R. S., Large-Area Graphene Single Crystals Grown by Low-Pressure Chemical Vapor Deposition of Methane on Copper. *Journal of the American Chemical Society* **2011,** *133* (9), 2816-2819.
150. Chen, S.; Ji, H.; Chou, H.; Li, Q.; Li, H.; Suk, J. W.; Piner, R.; Liao, L.; Cai, W.; Ruoff, R. S., Millimeter-Size Single-Crystal Graphene by Suppressing Evaporative Loss of Cu During Low Pressure Chemical Vapor Deposition. *Advanced Materials* **2013,** *25* (14), 2062-2065.
151. Mohsin, A.; Liu, L.; Liu, P.; Deng, W.; Ivanov, I. N.; Li, G.; Dyck, O. E.; Duscher, G.; Dunlap, J. R.; Xiao, K.; Gu, G., Synthesis of Millimeter-Size Hexagon-Shaped Graphene Single Crystals on Resolidified Copper. *ACS Nano* **2013,** *7* (10), 8924-8931.
152. Zhou, H.; Yu, W. J.; Liu, L.; Cheng, R.; Chen, Y.; Huang, X.; Liu, Y.; Wang, Y.; Huang, Y.; Duan, X., Chemical vapour deposition growth of large single crystals of monolayer and bilayer graphene. *Nature Communications* **2013,** *4*, 2096-2104.
153. Gan, L.; Luo, Z., Turning off Hydrogen To Realize Seeded Growth of Subcentimeter Single-Crystal Graphene Grains on Copper. *ACS Nano* **2013,** *7* (10), 9480-9488.
154. Hao, Y.; Bharathi, M. S.; Wang, L.; Liu, Y.; Chen, H.; Nie, S.; Wang, X.; Chou, H.; Tan, C.; Fallahazad, B.; Ramanarayan, H.; Magnuson, C. W.; Tutuc, E.; Yakobson, B. I.; McCarty, K. F.; Zhang, Y.-W.; Kim, P.; Hone, J.; Colombo, L.; Ruoff, R. S., The Role of Surface Oxygen in the Growth of Large Single-Crystal Graphene on Copper. *Science* **2013,** *342* (6159), 720-723.
155. Friedrichs, P.; Kimoto, T.; Ley, L.; Pensl, G., *Silicon Carbide*. Wiley-VCH: 2011.
156. Saddow, S.; Agarwal, A., *Advances in Silicon Carbide Processing and Applications*. Artech House Inc: Norwood, 2004.
157. Schardt, J.; Bernhardt, J.; Starke, U.; Heinz, K., Atomic structure of hexagonal 6H-And 3C-SiC surfaces. *Surface Review and Letters* **1998,** *5* (1), 181-186.
158. Luo, X.; Goel, S.; Reuben, R. L., A quantitative assessment of nanometric machinability of major polytypes of single crystal silicon carbide. *Journal of the European Ceramic Society* **2012,** *32* (12), 3423-3434.
159. Forbeaux, I.; Themlin, J. M.; Charrier, A.; Thibaudau, F.; Debever, J. M., Solid-state graphitization mechanisms of silicon carbide 6H–SiC polar faces. *Applied Surface Science* **2000,** *162–163* (0), 406-412.
160. Van Bommel, A. J.; Crombeen, J. E.; Van Tooren, A., LEED and Auger electron observations of the SiC(0001) surface. *Surface Science* **1975,** *48* (2), 463-472.
161. Berger, C.; Song, Z.; Li, T.; Li, X.; Ogbazghi, A. Y.; Feng, R.; Dai, Z.; Marchenkov, A. N.; Conrad, E. H.; First, P. N.; de Heer, W. A., Ultrathin Epitaxial Graphite: 2D Electron Gas Properties and a Route toward Graphene-based Nanoelectronics. *The Journal of Physical Chemistry B* **2004,** *108* (52), 19912-19916.
162. Norimatsu, W.; Kusunoki, M., Epitaxial graphene on SiC{0001}: advances and perspectives. *Physical Chemistry Chemical Physics* **2014,** *16* (8), 3501-3511.

163. Ouerghi, A.; Marangolo, M.; Belkhou, R.; El Moussaoui, S.; Silly, M. G.; Eddrief, M.; Largeau, L.; Portail, M.; Fain, B.; Sirotti, F., Epitaxial graphene on 3C-SiC(111) pseudosubstrate: Structural and electronic properties. *Physical Review B - Condensed Matter and Materials Physics* **2010,** *82* (12).
164. Abe, S.; Handa, H.; Takahashi, R.; Imaizumi, K.; Fukidome, H.; Suemitsu, M., Surface Chemistry Involved in Epitaxy of Graphene on 3C-SiC(111)/Si(111). *Nanoscale Research Letters* **2010,** *5* (12), 1888-1891.
165. Starke, U.; Schardt, J.; Bernhardt, J.; Franke, M.; Heinz, K., Stacking Transformation from Hexagonal to Cubic SiC Induced by Surface Reconstruction: A Seed for Heterostructure Growth. *Physical Review Letters* **1999,** *82* (10), 2107-2110.
166. Gupta, B.; Notarianni, M.; Mishra, N.; Shafiei, M.; Iacopi, F.; Motta, N., Evolution of epitaxial graphene layers on 3C SiC/Si (1 1 1) as a function of annealing temperature in UHV. *Carbon* **2014,** *68*, 563-572.
167. Emtsev, K. V.; Speck, F.; Seyller, T.; Ley, L., Interaction, growth, and ordering of epitaxial graphene on SiC{0001} surfaces: A comparative photoelectron spectroscopy study. *Physical Review B* **2008,** *77* (15), 155303-155400.
168. Starke, U.; Bram, C.; Steiner, P. R.; Hartner, W.; Hammer, L.; Heinz, K.; Müller, K., The (0001)-surface of 6HSiC: morphology, composition and structure. *Applied Surface Science* **1995,** *89* (2), 175-185.
169. Emtsev, K. V.; Bostwick, A.; Horn, K.; Jobst, J.; Kellogg, G. L.; Ley, L.; McChesney, J. L.; Ohta, T.; Reshanov, S. A.; Röhrl, J.; Rotenberg, E.; Schmid, A. K.; Waldmann, D.; Weber, H. B.; Seyller, T., Towards wafer-size graphene layers by atmospheric pressure graphitization of silicon carbide. *Nature materials* **2009,** *8* (3), 203-207.
170. Virojanadara, C.; Syväjarvi, M.; Yakimova, R.; Johansson, L. I.; Special, a.; Max, l.; Lunds, u.; Max, l.; Lund, U.; Särskilda, v., Homogeneous large-area graphene layer growth on 6H -SiC(0001). *Physical Review B* **2008,** *78* (24), 245403-245410.
171. Tromp, R. M.; Hannon, J. B., Thermodynamics and Kinetics of Graphene Growth on SiC(0001). *Physical Review Letters* **2009,** *102* (10), 106104.
172. Norimatsu, W.; Kusunoki, M., Transitional structures of the interface between graphene and 6H–SiC (0001). *Chemical Physics Letters* **2009,** *468* (1–3), 52-56.
173. Kuroki, J.; Norimatsu, W.; Kusunoki, M., Plan-View of Few Layer Graphene on 6H-SiC by Transmission Electron Microscopy. *e-Journal of Surface Science and Nanotechnology* **2012,** *10*, 396-399.
174. Berger, C.; Song, Z.; Li, X.; Wu, X.; Brown, N.; Naud, C.; Mayou, D.; Li, T.; Hass, J.; Marchenkov, A. N.; Conrad, E. H.; First, P. N.; de Heer, W. A., Electronic Confinement and Coherence in Patterned Epitaxial Graphene. *Science* **2006,** *312* (5777), 1191-1196.
175. Avouris, P.; Xia, F., Graphene applications in electronics and photonics. *MRS Bulletin* **2012,** *37* (12), 1225-1234.
176. Lin, Y.-M.; Valdes-Garcia, A.; Han, S.-J.; Farmer, D. B.; Meric, I.; Sun, Y.; Wu, Y.; Dimitrakopoulos, C.; Grill, A.; Avouris, P.; Jenkins, K. A., Wafer-Scale Graphene Integrated Circuit. *Science* **2011,** *332* (6035), 1294-1297.
177. Powell, C.; Bender, T.; Lawryshyn, Y., A model to determine financial indicators for organic solar cells. *Solar Energy* **2009,** *83* (11), 1977-1984.
178. Kalowekamo, J.; Baker, E., Estimating the manufacturing cost of purely organic solar cells. *Solar Energy* **2009,** *83* (8), 1224-1231.
179. Krebs, F. C., Fabrication and processing of polymer solar cells: A review of printing and coating techniques. *Solar Energy Materials and Solar Cells* **2009,** *93* (4), 394-412.
180. Kippelen, B.; Brédas, J. L., Organic photovoltaics. *Energy and Environmental Science* **2009,** *2* (3), 251-261.
181. Heliatek (Firm) Heliatek consolidates technology leadership by establishing a new world record for organic solar technology with a cell efficiency of 12% (press release). http://www.heliatek.com/newscenter/latest_news/neuer-weltrekord-fur-

organische-solarzellen-heliatek-behauptet-sich-mit-12-zelleffizienz-als-technologiefuhrer/?lang=en (accessed 21 June).
182. (NREL), N. R. E. L. Best Reserach-Cell Efficiencies. http://www.nrel.gov/ncpv/images/efficiency_chart.jpg.
183. Dennler, G.; Scharber, M. C.; Brabec, C. J., Polymer-Fullerene Bulk-Heterojunction Solar Cells. *Advanced Materials* **2009,** *21* (13), 1323-1338.
184. Jørgensen, M.; Norrman, K.; Krebs, F. C., Stability/degradation of polymer solar cells. *Solar Energy Materials and Solar Cells* **2008,** *92* (7), 686-714.
185. Brabec, C. J.; Durrant, J. R., Solution-processed organic solar cells. *MRS Bulletin* **2008,** *33* (7), 670-675.
186. Mihailetchi, V. D.; Koster, L. J. A.; Blom, P. W. M.; Melzer, C.; De Boer, B.; Van Duren, J. K. J.; Janssen, R. A. J., Compositional dependence of the performance of poly(p-phenylene vinylene):Methanofullerene bulk-heterojunction solar cells. *Advanced Functional Materials* **2005,** *15* (5), 795-801.
187. Erb, T.; Zhokhavets, U.; Gobsch, G.; Raleva, S.; Stühn, B.; Schilinsky, P.; Waldauf, C.; Brabec, C. J., Correlation between structural and optical properties of composite polymer/fullerene films for organic solar cells. *Advanced Functional Materials* **2005,** *15* (7), 1193-1196.
188. Guo, H.; Sreekumar, T. V.; Liu, T.; Minus, M.; Kumar, S., "Structutre and properties of polyacrylonitrile/single wall carbon nanotube composite films". *Polymer* **2005,** *46*, 3001-3005.
189. Sariciftci, N. S.; Smilowitz, L.; Heeger, A. J.; Wudl, F., Photoinduced Electron Transfer from a Conducting Polymer to Buckminsterfullerene. *Science* **1992,** *258* (5087), 1474-1476.
190. Umnov, A. G.; Korovyanko, O. J., Photovoltaic effect in poly-dioctyl-phenylene-ethynylene-C[sub 60] cells upon donor and acceptor excitation. *Applied Physics Letters* **2005,** *87* (11), 113506-3.
191. Krebs, F. C., *Polymeric Solar Cells: Materials, Design, Manufacture*. 2010.
192. Nunzi, J. M., Organic photovoltaic materials and devices. *Comptes Rendus Physique* **2002,** *3* (4), 523-542.
193. Halls, J. J. M.; Pichler, K.; Friend, R. H.; Moratti, S. C.; Holmes, A. B., Exciton diffusion and dissociation in a poly(p-phenylenevinylene)/C[sub 60] heterojunction photovoltaic cell. *Applied Physics Letters* **1996,** *68* (22), 3120-3122.
194. Theander, M.; Yartsev, A.; Zigmantas, D.; Sundström, V.; Mammo, W.; Andersson, M. R.; Inganäs, O., Photoluminescence quenching at a polythiophene/C_{60} heterojunction. *Physical Review B* **2000,** *61* (19), 12957-12963.
195. Pivrikas, A.; Neugebauer, H.; Sariciftci, N. S., Influence of processing additives to nano-morphology and efficiency of bulk-heterojunction solar cells: A comparative review. *Solar Energy* **2011,** *85* (6), 1226-1237.
196. Watkins, P. K.; Walker, A. B.; Verschoor, G. L. B., Dynamical monte carlo modelling of organic solar cells: The dependence of internal quantum efficiency on morphology. *Nano Letters* **2005,** *5* (9), 1814-1818.
197. Yusuf, K. Q.; Motta, N.; Pawlak, Z.; Oloyede, A., A Microanalytical Study of the Surfaces of Normal, Delipidized, and Artificially "Resurfaced" Articular Cartilage. *Connective Tissue Research* **2012,** *53* (3), 236-245.
198. Tao, C.; Aljada, M.; Shaw, P. E.; Lee, K. H.; Cavaye, H.; Balfour, M. N.; Borthwick, R. J.; James, M.; Burn, P. L.; Gentle, I. R.; Meredith, P., Controlling hierarchy in solution-processed polymer solar cells based on crosslinked P3HT. *Advanced Energy Materials* **2013,** *3* (1), 105-112.
199. Lee, K. H.; Schwenn, P. E.; Smith, A. R. G.; Cavaye, H.; Shaw, P. E.; James, M.; Krueger, K. B.; Gentle, I. R.; Meredith, P.; Burn, P. L., Morphology of All-Solution-Processed "Bilayer" Organic Solar Cells. *Advanced Materials (Weinheim, Germany)* **2011,** *23* (6), 766-770.

200. Seemann, A.; Sauermann, T.; Lungenschmied, C.; Armbruster, O.; Bauer, S.; Egelhaaf, H. J.; Hauch, J., Reversible and irreversible degradation of organic solar cell performance by oxygen. *Solar Energy* **2011,** *85* (6), 1238-1249.
201. Nelson, J., Polymer: Fullerene bulk heterojunction solar cells. *Materials Today* **2011,** *14* (10), 462-470.
202. Bindl, D. J.; Wu, M. Y.; Prehn, F. C.; Arnold, M. S., Efficiently harvesting excitons from electronic type-controlled semiconducting carbon nanotube films. *Nano Letters* **2011,** *11* (2), 455-460.
203. Hau, S. K.; Yip, H. L.; Jen, A. K. Y., A review on the development of the inverted polymer solar cell architecture. *Polymer Reviews* **2010,** *50* (4), 474-510.
204. Notarianni, M.; Vernon, K.; Chou, A.; Aljada, M.; Liu, J.; Motta, N., Plasmonic effect of gold nanoparticles in organic solar cells. *Solar Energy* **2013**.
205. McEvoy, A.; Castaner, L.; Markvart, T., *Solar Cells: Materials, Manufacture and Operation*. Academic Press: GB, 2013.
206. Miller, B.; Rosamilia, J. M.; Dabbagh, G.; Tycko, R.; Haddon, R. C.; Muller, A. J.; Wilson, W.; Murphy, D. W.; Hebard, A. F., Photoelectrochemical behavior of C60 films. *Journal of the American Chemical Society* **1991,** *113* (16), 6291-6293.
207. Sariciftci, N. S.; Braun, D.; Zhang, C.; Srdanov, V. I.; Heeger, A. J.; Stucky, G.; Wudl, F., Semiconducting polymer-buckminsterfullerene heterojunctions: Diodes, photodiodes, and photovoltaic cells. *Applied Physics Letters* **1993,** *75* (6), 585-587.
208. Dang, M. T.; Hirsch, L.; Wantz, G., P3HT:PCBM, Best Seller in Polymer Photovoltaic Research. *Advanced Materials (Weinheim, Germany)* **2011,** *23* (31), 3597-3602.
209. Wienk, M. M.; Kroon, J. M.; Verhees, W. J. H.; Knol, J.; Hummelen, J. C.; van Hal, P. A.; Janssen, R. A. J., Efficient methano[70]fullerene/MDMO-PPV bulk heterojunction photovoltaic cells. *Angewandte Chemie (International ed.in English)* **2003,** *42* (29), 3371-3375.
210. Liang, Y.; Xu, Z.; Xia, J.; Tsai, S.-T.; Wu, Y.; Li, G.; Ray, C.; Yu, L., For the Bright Future—Bulk Heterojunction Polymer Solar Cells with Power Conversion Efficiency of 7.4%. *Advanced Materials* **2010,** *22* (20), E135-E138.
211. Nierengarten, J.-F., Chemical modification of C60 for materials science applications. *New Journal of Chemistry* **2004,** *28* (10), 1177-1191.
212. Sgobba, V.; Guldi, D. M., Carbon nanotubes as integrative materials for organic photovoltaic devices. *Journal of Materials Chemistry* **2008,** *18* (2), 153-157.
213. Ren, S.; Bernardi, M.; Lunt, R. R.; Bulovic, V.; Grossman, J. C.; Gradečak, S., Toward efficient carbon nanotube/P3HT solar cells: Active layer morphology, electrical, and optical properties. *Nano Letters* **2011,** *11* (12), 5316-5321.
214. Lu, L.; Xu, T.; Chen, W.; Lee, J. M.; Luo, Z.; Jung, I. H.; Park, H. I.; Kim, S. O.; Yu, L., The Role of N-Doped Multiwall Carbon Nanotubes in Achieving Highly Efficient Polymer Bulk Heterojunction Solar Cells. *Nano Letters* **2013,** *13* (6), 2365-2369.
215. Bernardi, M.; Giulianini, M.; Grossman, J. C., Self-assembly and its impact on interfacial charge transfer in carbon nanotube/P3HT solar cells. *ACS Nano* **2010,** *4* (11), 6599-6606.
216. Caddeo, C.; Melis, C.; Colombo, L.; Mattoni, A., Understanding the helical wrapping of poly(3-hexylthiophene) on carbon nanotubes. *Journal of Physical Chemistry C* **2010,** *114* (49), 21109-21113.
217. Giulianini, M.; Waclawik, E. R.; Bell, J. M.; Scarselli, M.; Castrucci, P.; De Crescenzi, M.; Motta, N., Microscopic and spectroscopic investigation of Poly (3-hexylthiophene) interaction with carbon nanotubes. *Polymers* **2011,** *3* (3), 1433-1446.
218. Giulianini, M.; Waclawik, E. R.; Bell, J. M.; Crescenzi, M. D.; Castrucci, P.; Scarselli, M.; Diociauti, M.; Casciardi, S.; Motta, N., Evidence of multiwall carbon nanotube deformation caused by poly(3-hexylthiophene) adhesion. *Journal of Physical Chemistry C* **2011,** *115* (14), 6324-6330.

219. Kanai, Y.; Grossman, J. C., Role of semiconducting and metallic tubes in P3HT/carbon-nanotube photovoltaic heterojunctions: Density functional theory calculations. *Nano Letters* **2008,** *8* (3), 908-912.
220. Liu, L.; Stanchina, W. E.; Li, G., Effects of semiconducting and metallic single-walled carbon nanotubes on performance of bulk heterojunction organic solar cells. *Applied Physics Letters* **2009,** *94* (23), 233309-233309-03.
221. Giulianini, M.; Waclawik, E. R.; Bell, J. M.; Scarselli, M.; Castrucci, P.; De Crescenzi, M.; Motta, N., Poly(3-hexyl-thiophene) coil-wrapped single wall carbon nanotube investigated by scanning tunneling spectroscopy. *Applied Physics Letters* **2009,** *95* (14), 143116-3.
222. Schuettfort, T.; Nish, A.; Nicholas, R. J., Observation of a type II heterojunction in a highly ordered polymer− carbon nanotube nanohybrid structure. *Nano letters* **2009,** *9* (11), 3871-3876.
223. Dabera, G. D. M. R.; Jayawardena, K. D. G. I.; Prabhath, M. R. R.; Yahya, I.; Tan, Y. Y.; Nismy, N. A.; Shiozawa, H.; Sauer, M.; Ruiz-Soria, G.; Ayala, P.; Stolojan, V.; Adikaari, A. A. D. T.; Jarowski, P. D.; Pichler, T.; Silva, S. R. P., Hybrid Carbon Nanotube Networks as Efficient Hole Extraction Layers for Organic Photovoltaics. *ACS Nano* **2012,** *7* (1), 556-565.
224. Vavro, J.; Llaguno, M. C.; Fischer, J. E.; Ramesh, S.; Saini, R. K.; Ericson, L. M.; Davis, V. A.; Hauge, R. H.; Pasquali, M.; Smalley, R. E., Thermoelectric Power ofp-Doped Single-Wall Carbon Nanotubes and the Role of Phonon Drag. *Physical Review Letters* **2003,** *90* (6).
225. Jeong, H.; Park, J.-Y., Local Electrical Investigations of Nitric Acid Treatment Effects on Carbon Nanotube Networks. *The Journal of Physical Chemistry C* **2015,** *119* (17), 9665-9668.
226. Sun, Y.; Gong, X.; Hsu, B. B. Y.; Yip, H.-L.; Jen, A. K. Y.; Heeger, A. J., Solution-processed cross-linkable hole selective layer for polymer solar cells in the inverted structure. *Applied Physics Letters* **2010,** *97* (19), 193310-3.
227. Kim, S.; Yim, J.; Wang, X.; Bradley, D. D. C.; Lee, S.; deMello, J. C., Spin- and Spray-Deposited Single-Walled Carbon-Nanotube Electrodes for Organic Solar Cells. *Advanced Functional Materials* **2010,** *20* (14), 2310-2316.
228. Kymakis, E.; Stylianakis, M. M.; Spyropoulos, G. D.; Stratakis, E.; Koudoumas, E.; Fotakis, C., Spin coated carbon nanotubes as the hole transport layer in organic photovoltaics. *Solar Energy Materials and Solar Cells* **2012,** *96*, 298-301.
229. Giulianini, M.; Waclawik, E. R.; Bell, J. M.; Scarselli, M.; Castrucci, P.; De Crescenzi, M.; Motta, N., Poly(3-hexyl-thiophene) coil-wrapped single wall carbon nanotube investigated by scanning tunneling spectroscopy. *Applied Physics Letters* **2009,** *95* (14).
230. Jung, Y.; Li, X.; Rajan, N. K.; Taylor, A. D.; Reed, M. A., Record high efficiency single-walled carbon nanotube/silicon p-n junction solar cells. *Nano Lett* **2013,** *13* (1), 95-9.
231. Wang, F.; Kozawa, D.; Miyauchi, Y.; Hiraoka, K.; Mouri, S.; Ohno, Y.; Matsuda, K., Considerably improved photovoltaic performance of carbon nanotube-based solar cells using metal oxide layers. *Nat Commun* **2015,** *6*, 6305.
232. Capasso, A.; Salamandra, L.; Di Carlo, A.; Bell, J. M.; Motta, N., Low-temperature synthesis of carbon nanotubes on indium tin oxide electrodes for organic solar cells. *Beilstein Journal of Nanotechnology* **2012,** *3* (1), 524-532.
233. Miller, A. J.; Hatton, R. A.; Chen, G. Y.; Silva, S. R. P., Carbon nanotubes grown on In[sub 2]O[sub 3]:Sn glass as large area electrodes for organic photovoltaics. *Applied Physics Letters* **2007,** *90* (2), 023105-3.
234. Capasso, A.; Salamandra, L.; Chou, A.; Di Carlo, A.; Motta, N., Multi-wall carbon nanotube coating of fluorine-doped tin oxide as an electrode surface modifier for polymer solar cells. *Solar Energy Materials and Solar Cells* **2014,** *122*, 297-302.

235. Sears, K.; Fanchini, G.; Watkins, S. E.; Huynh, C. P.; Hawkins, S. C., Aligned carbon nanotube webs as a replacement for indium tin oxide in organic solar cells. *Thin Solid Films* **2013,** *531*, 525-529.
236. Mirri, F.; Ma, A. W. K.; Hsu, T. T.; Behabtu, N.; Eichmann, S. L.; Young, C. C.; Tsentalovich, D. E.; Pasquali, M., High-Performance Carbon Nanotube Transparent Conductive Films by Scalable Dip Coating. *ACS Nano* **2012,** *6* (11), 9737-9744.
237. Kim, K.; Bae, S.-H.; Toh, C. T.; Kim, H.; Cho, J. H.; Whang, D.; Lee, T.-W.; Özyilmaz, B.; Ahn, J.-H., Ultrathin Organic Solar Cells with Graphene Doped by Ferroelectric Polarization. *ACS Applied Materials & Interfaces* **2014,** *6* (5), 3299-3304.
238. Sangchul, L.; Jun-Seok, Y.; Yongsung, J.; Chunhum, C.; Dong-Yu, K.; Seok-In, N.; Byoung Hun, L.; Takhee, L., Flexible organic solar cells composed of P3HT:PCBM using chemically doped graphene electrodes. *Nanotechnology* **2012,** *23* (34), 344013.
239. Bonaccorso, F.; Sun, Z.; Hasan, T.; Ferrari, A. C., Graphene photonics and optoelectronics. *Nature Photonics* **2010,** *4* (9), 611-622.
240. Liscio, A.; Veronese, G. P.; Treossi, E.; Suriano, F.; Rossella, F.; Bellani, V.; Rizzoli, R.; Samori, P.; Palermo, V., Charge transport in graphene-polythiophene blends as studied by Kelvin Probe Force Microscopy and transistor characterization. *Journal of Materials Chemistry* **2011,** *21* (9), 2924-2931.
241. Stylianakis, M. M.; Stratakis, E.; Koudoumas, E.; Kymakis, E.; Anastasiadis, S. H., Organic Bulk Heterojunction Photovoltaic Devices Based on Polythiophene–Graphene Composites. *ACS Applied Materials & Interfaces* **2012,** *4* (9), 4864-4870.
242. Wang, J.; Wang, Y.; He, D.; Liu, Z.; Wu, H.; Wang, H.; Zhao, Y.; Zhang, H.; Yang, B., Composition and annealing effects in solution-processable functionalized graphene oxide/P3HT based solar cells. *Synthetic Metals* **2010,** *160* (23-24), 2494-2500.
243. Liu, J.; Xue, Y.; Gao, Y.; Yu, D.; Durstock, M.; Dai, L., Hole and electron extraction layers based on graphene oxide derivatives for high-performance bulk heterojunction solar cells. *Advanced Materials* **2012,** *24* (17), 2228-2233.
244. Ryu, M. S.; Jang, J., Effect of solution processed graphene oxide/nickel oxide bi-layer on cell performance of bulk-heterojunction organic photovoltaic. *Solar Energy Materials and Solar Cells* **2011,** *95* (10), 2893-2896.
245. Li, S.-S.; Tu, K.-H.; Lin, C.-C.; Chen, C.-W.; Chhowalla, M., Solution-Processable Graphene Oxide as an Efficient Hole Transport Layer in Polymer Solar Cells. *ACS Nano* **2010,** *4* (6), 3169-3174.
246. Liu, J.; Durstock, M.; Dai, L., Graphene oxide derivatives as hole- and electron-extraction layers for high-performance polymer solar cells. *Energy & Environmental Science* **2014,** *7* (4), 1297-1306.
247. Kim, J.; Tung, V. C.; Huang, J., Water Processable Graphene Oxide:Single Walled Carbon Nanotube Composite as Anode Modifier for Polymer Solar Cells. *Advanced Energy Materials* **2011,** *1* (6), 1052-1057.
248. Bernardi, M.; Lohrman, J.; Kumar, P. V.; Kirkeminde, A.; Ferralis, N.; Grossman, J. C.; Ren, S., Nanocarbon-based photovoltaics. *ACS Nano* **2012,** *6* (10), 8896-8903.
249. Bao, Z. Design and Fabrication of the First All-Carbon-Based Solar Cell. http://web.stanford.edu/group/gcep/cgi-bin/gcep-research/all/design-and-fabrication-of-the-first-all-carbon-based-solar-cell/.
250. Ramuz, M. P.; Vosgueritchian, M.; Wei, P.; Wang, C.; Gao, Y.; Wu, Y.; Chen, Y.; Bao, Z., Evaluation of Solution-Processable Carbon-Based Electrodes for All-Carbon Solar Cells. *ACS Nano* **2012,** *6* (11), 10384-10395.
251. Ameri, T.; Dennler, G.; Lungenschmied, C.; Brabec, C. J., Organic tandem solar cells: A review. *Energy and Environmental Science* **2009,** *2* (4), 347-363.
252. Li, X.; Zhu, H.; Wang, K.; Cao, A.; Wei, J.; Li, C.; Jia, Y.; Li, Z.; Li, X.; Wu, D., Graphene‐on‐silicon Schottky junction solar cells. *Advanced Materials* **2010,** *22* (25), 2743-2748.

253. Miao, X.; Tongay, S.; Petterson, M. K.; Berke, K.; Rinzler, A. G.; Appleton, B. R.; Hebard, A. F., High efficiency graphene solar cells by chemical doping. *Nano letters* **2012,** *12* (6), 2745-2750.
254. Shi, E.; Li, H.; Yang, L.; Zhang, L.; Li, Z.; Li, P.; Shang, Y.; Wu, S.; Li, X.; Wei, J., Colloidal antireflection coating improves graphene–silicon solar cells. *Nano letters* **2013,** *13* (4), 1776-1781.
255. Roy-Mayhew, J. D.; Aksay, I. A., Graphene materials and their use in dye-sensitized solar cells. *Chemical reviews* **2014,** *114* (12), 6323-6348.
256. Wang, H.; Hu, Y. H., Graphene as a counter electrode material for dye-sensitized solar cells. *Energy & Environmental Science* **2012,** *5* (8), 8182-8188.
257. Wang, X.; Zhi, L.; Müllen, K., Transparent, conductive graphene electrodes for dye-sensitized solar cells. *Nano letters* **2008,** *8* (1), 323-327.
258. Wang, X.; Zhi, L.; Müllen, K., Transparent, Conductive Graphene Electrodes for Dye-Sensitized Solar Cells. *Nano Letters* **2007,** *8* (1), 323-327.
259. Lu, M.; Beguin, F.; Frackowiak, E., *Supercapacitors*. Wiley-VCH: 2013.
260. Becker, H. E. 1957.
261. Boos, D. I. 1970.
262. T.C. Murphy, R. B. W., R.A. Sutula, in: F.M. Del- nick, D. Ingersoll, X. Andrieu, K. Naoi In *Electrochemical Capacitors II*, The Electrochemical Society, Pennington, NJ, Pennington, NJ, 1997; p 258.
263. Aslani, M. Electrochemical Double Layer Capacitors (Supercapacitors). http://large.stanford.edu/courses/2012/ph240/aslani1/. (accessed 09/09/2015).
264. Gobert, Y. Volvo develops batteries (supercapacitors) integrated with body panels. http://www.technologicvehicles.com/en/green-transportation-news/2597/video-volvo-develops-batteries-supercapacitors-integrated-with-body-panels - .U-o98VHanX0.
265. Elcap Supercapacitor. http://en.wikipedia.org/wiki/Supercapacitor.
266. Conway, B. E., *Electrohcemical Supercapacitors*. Plenum Publishing: New York, 1999, p 560.
267. Helmholtz, H. V., *Ann. Phys. (Leipzig)* **1853,** *89*, 21.
268. Gouy, G., *J. Phys.* **1910,** *4*, 457.
269. Chapman, D. L., *Philos. Mag.* **1913,** *6*, 475.
270. Stern, O., *Z. Electrochem.* **1924,** *30*, 508.
271. Zhang, L. L.; Zhao, X. S., Carbon-based materials as supercapacitor electrodes. *Chem. Soc. Rev.* **2009,** *38* (9), 2520-2531.
272. Kötz, R.; Carlen, M., Principles and applications of electrochemical capacitors. *Electrochimica Acta* **2000,** *45* (15–16), 2483-2498.
273. Zhang, K.; Zhang, L. L.; Zhao, X. S.; Wu, J., Graphene/Polyaniline Nanofiber Composites as Supercapacitor Electrodes. *Chemistry of Materials* **2010,** *22* (4), 1392-1401.
274. Sugimoto, W.; Yokoshima, K.; Murakami, Y.; Takasu, Y., Charge storage mechanism of nanostructured anhydrous and hydrous ruthenium-based oxides. *Electrochimica Acta* **2006,** *52* (4), 1742-1748.
275. Wang, J., *Analytical Electrochemistry*. Wiley-VCH: 2006.
276. Pell, W. G.; Conway, B. E., Analysis of power limitations at porous supercapacitor electrodes under cyclic voltammetry modulation and dc charge. *Journal of Power Sources* **2001,** *96* (1), 57-67.
277. Qu, D.; Shi, H., Studies of activated carbons used in double-layer capacitors. *Journal of Power Sources* **1998,** *74* (1), 99-107.
278. Raymundo-Piñero, E.; Kierzek, K.; Machnikowski, J.; Béguin, F., Relationship between the nanoporous texture of activated carbons and their capacitance properties in different electrolytes. *Carbon* **2006,** *44* (12), 2498-2507.

279. Kierzek, K.; Frackowiak, E.; Lota, G.; Gryglewicz, G.; Machnikowski, J., Electrochemical capacitors based on highly porous carbons prepared by KOH activation. *Electrochimica Acta* **2004,** *49* (4), 515-523.
280. Bose, S.; Kuila, T.; Mishra, A. K.; Rajasekar, R.; Kim, N. H.; Lee, J. H., Carbon-based nanostructured materials and their composites as supercapacitor electrodes. *Journal of Materials Chemistry* **2012,** *22* (3), 767-784.
281. Candelaria, S. L.; Shao, Y.; Zhou, W.; Li, X.; Xiao, J.; Zhang, J. G.; Wang, Y.; Liu, J.; Li, J.; Cao, G., Nanostructured carbon for energy storage and conversion. *Nano Energy* **2012,** *1* (2), 195-220.
282. Yu, A., *Electrochemical Energy Storage and Conversion: Electrochemical Supercapacitors for Energy Storage and Delivery : Fundamentals and Applications*. CRC Press: 2013.
283. Azam, M. A.; Fujiwara, A.; Shimoda, T., Significant capacitance performance of vertically aligned single-walled carbon nanotube supercapacitor by varying potassium hydroxide concentration. *International Journal of Electrochemical Science* **2013,** *8* (3), 3902-3911.
284. Chunsheng, D.; Jeff, Y.; Ning, P., High power density supercapacitors using locally aligned carbon nanotube electrodes. *Nanotechnology* **2005,** *16* (4), 350.
285. Zhang, H.; Cao, G.; Yang, Y.; Gu, Z., Comparison between electrochemical properties of aligned carbon nanotube array and entangled carbon nanotube electrodes. *Journal of the Electrochemical Society* **2008,** *155* (2), K19-K22.
286. Liu, C.; Li, F.; Lai-Peng, M.; Cheng, H. M., Advanced materials for energy storage. *Advanced Materials* **2010,** *22* (8), E28-E62.
287. Inagaki, M.; Konno, H.; Tanaike, O., Carbon materials for electrochemical capacitors. *Journal of Power Sources* **2010,** *195* (24), 7880-7903.
288. Niu, C.; Sichel, E. K.; Hoch, R.; Moy, D.; Tennent, H., High power electrochemical capacitors based on carbon nanotube electrodes. *Applied Physics Letters* **1997,** *75* (11), 1480-1482.
289. Emmenegger, C.; Mauron, P.; Sudan, P.; Wenger, P.; Hermann, V.; Gallay, R.; Züttel, A., Investigation of electrochemical double-layer (ECDL) capacitors electrodes based on carbon nanotubes and activated carbon materials. *Journal of Power Sources* **2003,** *124* (1), 321-329.
290. Yamada, Y.; Kimizuka, O.; Tanaike, O.; Machida, K.; Suematsu, S.; Tamamitsu, K.; Saeki, S.; Yamada, Y.; Hatori, H., Capacitor Properties and Pore Structure of Single- and Double-Walled Carbon Nanotubes. *Electrochemical and Solid-State Letters* **2009,** *12* (3), K14.
291. Liu, C. G.; Fang, H. T.; Li, F.; Liu, M.; Cheng, H. M., Single-walled carbon nanotubes modified by electrochemical treatment for application in electrochemical capacitors. *Journal of Power Sources* **2006,** *160* (1), 758-761.
292. O.Tanaike, D. N. F., K. Hata, H. Hatori, Supercapacitors using pure single-walled carbon nanotubes. *Carbon Letter* **2009,** *10*, 90-93.
293. Hiraoka, T.; Izadi-Najafabadi, A.; Yamada, T.; Futaba, D. N.; Yasuda, S.; Tanaike, O.; Hatori, H.; Yumura, M.; Iijima, S.; Hata, K., Compact and Light Supercapacitor Electrodes from a Surface-Only Solid by Opened Carbon Nanotubes with 2 200 m2 g−1 Surface Area. *Advanced Functional Materials* **2010,** *20* (3), 422-428.
294. Futaba, D. N.; Hata, K.; Yamada, T.; Hiraoka, T.; Hayamizu, Y.; Kakudate, Y.; Tanaike, O.; Hatori, H.; Yumura, M.; Iijima, S., Shape-engineerable and highly densely packed single-walled carbon nanotubes and their application as super-capacitor electrodes. *Nature materials* **2006,** *5* (12), 987-994.
295. Bordjiba, T.; Mohamedi, M.; Dao, L. H., New Class of Carbon-Nanotube Aerogel Electrodes for Electrochemical Power Sources. *Advanced Materials* **2008,** *20* (4), 815-819.
296. Huang, Y.; Liang, J.; Chen, Y., An overview of the applications of graphene-based materials in supercapacitors. *Small* **2012,** *8* (12), 1805-1834.

297. Wang, Y.; Shi, Z.; Huang, Y.; Ma, Y.; Wang, C.; Chen, M.; Chen, Y., Supercapacitor Devices Based on Graphene Materials. *The Journal of Physical Chemistry C* **2009,** *113* (30), 13103-13107.
298. Chen, Y.; Zhang, X.; Zhang, D.; Yu, P.; Ma, Y., High performance supercapacitors based on reduced graphene oxide in aqueous and ionic liquid electrolytes. *Carbon* **2011,** *49* (2), 573-580.
299. Lv, W.; Tang, D.-M.; He, Y.-B.; You, C.-H.; Shi, Z.-Q.; Chen, X.-C.; Chen, C.-M.; Hou, P.-X.; Liu, C.; Yang, Q.-H., Low-Temperature Exfoliated Graphenes: Vacuum-Promoted Exfoliation and Electrochemical Energy Storage. *ACS Nano* **2009,** *3* (11), 3730-3736.
300. El-Kady, M. F.; Strong, V.; Dubin, S.; Kaner, R. B., Laser Scribing of High-Performance and Flexible Graphene-Based Electrochemical Capacitors. *Science* **2012,** *335* (6074), 1326-1330.
301. El-Kady, M. F.; Kaner, R. B., Scalable fabrication of high-power graphene micro-supercapacitors for flexible and on-chip energy storage. *Nature Communications* **2013,** *4*.
302. Xu, Y.; Lin, Z.; Huang, X.; Liu, Y.; Huang, Y.; Duan, X., Flexible Solid-State Supercapacitors Based on Three-Dimensional Graphene Hydrogel Films. *ACS Nano* **2013,** *7* (5), 4042-4049.
303. Wu, Z.-S.; Winter, A.; Chen, L.; Sun, Y.; Turchanin, A.; Feng, X.; Müllen, K., Three-dimensional nitrogen and boron co-doped graphene for high-performance all-solid-state supercapacitors. *Advanced Materials* **2012,** *24* (37), 5130-5135.
304. Zhang, L.; Shi, G., Preparation of Highly Conductive Graphene Hydrogels for Fabricating Supercapacitors with High Rate Capability. *The Journal of Physical Chemistry C* **2011,** *115* (34), 17206-17212.
305. Chen, J.; Sheng, K.; Luo, P.; Li, C.; Shi, G., Graphene hydrogels deposited in nickel foams for high-rate electrochemical capacitors. *Advanced Materials* **2012,** *24* (33), 4569-4573.
306. Notarianni, M.; Liu, J.; Mirri, F.; Pasquali, M.; Motta, N., Graphene-based supercapacitor with carbon nanotube film as highly efficient current collector. *Nanotechnology* **2014,** *25* (43), 435405.
307. Zhu, Y.; Li, L.; Zhang, C.; Casillas, G.; Sun, Z.; Yan, Z.; Ruan, G.; Peng, Z.; Raji, A. R. O.; Kittrell, C.; Hauge, R. H.; Tour, J. M., A seamless three-dimensional carbon nanotube graphene hybrid material. *Nature Communications* **2012,** *3*.
308. Aboutalebi, S. H.; Chidembo, A. T.; Salari, M.; Konstantinov, K.; Wexler, D.; Liu, H. K.; Dou, S. X., Comparison of GO, GO/MWCNTs composite and MWCNTs as potential electrode materials for supercapacitors. *Energy & Environmental Science* **2011,** *4* (5), 1855-1865.
309. Jha, N.; Ramesh, P.; Bekyarova, E.; Itkis, M. E.; Haddon, R. C., High Energy Density Supercapacitor Based on a Hybrid Carbon Nanotube–Reduced Graphite Oxide Architecture. *Advanced Energy Materials* **2012,** *2* (4), 438-444.
310. Fan, Z.; Yan, J.; Zhi, L.; Zhang, Q.; Wei, T.; Feng, J.; Zhang, M.; Qian, W.; Wei, F., A three-dimensional carbon nanotube/graphene sandwich and its application as electrode in supercapacitors. *Advanced Materials* **2010,** *22* (33), 3723-3728.
311. Yu, D.; Dai, L., Self-Assembled Graphene/Carbon Nanotube Hybrid Films for Supercapacitors. *The Journal of Physical Chemistry Letters* **2009,** *1* (2), 467-470.
312. Wee, G.; Salim, T.; Lam, Y. M.; Mhaisalkar, S. G.; Srinivasan, M., Printable photo-supercapacitor using single-walled carbon nanotubes. *Energy & Environmental Science* **2011,** *4* (2), 413-416.